Formation and Diagenesis
of Sedimentary Rocks in
Gale Crater, Mars

Thesis by

Kirsten L. Siebach

In Partial Fulfillment of the Requirements for
the degree of
Doctor of Philosophy

CALIFORNIA INSTITUTE OF TECHNOLOGY
Pasadena, California

2016
(Defended May 19, 2016)

Kirsten L. Siebach
ORCID: 0000-0002-6628-6297

ACKNOWLEDGEMENTS

First, I would like to thank my advisor, John Grotzinger, for research and advising support over the last five years. I have greatly appreciated the chance to learn from his impressive example as a scientist, a leader, and as a field geologist, and for the opportunities he has given me to work on missions, to present and connect with other scientists, and to travel and get to see and learn about amazing rocks around the world. I would also like to thank Bethany Ehlmann for her mentorship, friendship, example, and helpful advice through several classes and years of group meetings. I am grateful to Paul Asimow and Mike Lamb for guidance on my first year project, advice on classes and graduate school, and for both of their examples as inspiring teachers, and to Ken Farley for his help and perspective on my thesis committee.

I have benefitted greatly from scientific and personal interactions with collaborators and mentors from the MSL science team—thanks particularly to Linda Kah, Scott McLennan, and Mike Baker, for very helpful discussions. A special thanks to Ray Arvidson, without whose advice and mentorship I would not be where I am today.

It has been a privilege to work with and learn from the faculty, staff, and students at Caltech. I want to thank the Grotzinger and Ehlmann groups, especially Jennifer Shechet, Katie Stack-Morgan, Melissa Rice, and Jennifer Buz, for discussions, friendship, and advice throughout graduate school, and helpful group meetings. I am also grateful to the wonderful staff members in the GPS division, especially Janice Grancich, Marcia Hudson, and Liz Boyd—I always leave your offices with a smile, thank you.

I cannot imagine how I would have finished the last five years without the incredible support I have had from my friends. Thanks to Mathieu Lapôtre, Pablo Guerrero, Morgane Grivel, and Abigail Fraeman, for meal breaks and countless miles of walking and discussions. Thanks to Sarah Slotznick for four years of excellent officemate chats and chocolate. Thanks to Caltech LDSSA for carpools, conversations, and ice cream adventures.

Finally, I would especially like to thank my family—my parents, Paul and Gretchen Siebach, my sister Chloe, and brother Jeffrey for their constant, endless love and support. Thanks for always answering the phone. I couldn't have done it without you.

ABSTRACT

The history of surface processes on Mars is recorded in the sedimentary rock record. Sedimentary rock layers exposed in Gale Crater on the modern crater floor (Aeolus Palus) and on Mount Sharp (Aeolus Mons), which hosts one of the more complete records of transitions between major mineralogical eras on Mars, have been investigated by the Mars Science Laboratory *Curiosity* rover since landing in August 2012. This dissertation focuses on the formation and diagenesis of the sedimentary rocks in Gale crater in order to assess the compositional diversity of the volcanic sources around Gale crater, the effects of transport processes on the sediment grains, and the volumes and geochemistry of water that transported and cemented the sediments. The first study uses orbital mapping of a distinctive cemented boxwork layer on Mount Sharp to constrain a minimum volume of groundwater available to form this layer, 1 km above the modern floor of Gale, with implications for the formation of Mount Sharp. The other three studies use *Curiosity* rover imagery and geochemical data to investigate sedimentary rocks in Aeolus Palus and at the base of Mount Sharp. The second study identifies and describes diagenetic synaeresis cracks in the Sheepbed mudstone, at the lowest elevation in Aeolus Palus, with implications for the duration of water saturation of these lake sediments. The third and fourth studies identify and explain geochemical trends in the fluvio-deltaic Bradbury group, the Murray mudstone formation, and the eolian Stimson sandstone, focusing on geochemical diversity in the source regions for each of these units and how different depositional processes are reflected in the geochemical data. The sedimentary system in Gale crater has changed our understanding of Mars by expanding the known variety of igneous rocks, increasing estimates of the longevity of surface water lakes, and showing that there were once habitable environments on our neighboring planet.

PUBLISHED CONTENT

Chapter 2 is published in:

Siebach, K. L., and J. P. Grotzinger. (2014) Volumetric Estimates of Ancient Water on Mount Sharp Based on Boxwork Deposits, Gale Crater, Mars. *J. Geophys. Res.*, online 28 Jan 2014, doi: 10.1002/2013JE004508.

Chapter 3 is published in:

Siebach, K. L., J. P. Grotzinger, L. C. Kah, K. M. Stack, M. Malin, R. Leveille, and D. Y. Sumner. (2014) Subaqueous Shrinkage Cracks in the Sheepbed Mudstone: Implications for Early Fluid Diagenesis, Gale Crater, Mars. *J. Geophys. Res.*, online 17 Jul 2014, doi: 10.1002/2014JE004623.

TABLE OF CONTENTS

LIST OF TABLES AND FIGURES

ACRONYMS

APXS. Alpha Particle X-Ray Spectrometer

BF. Bright Fractured unit

ChemCam. Chemistry and Camera

CheMin. Chemistry and Mineralogy

CIA. Chemical Index of Alteration

CTX. Context Camera

DTM. Digital Terrain Model

EP. Expected vertical Precision

GEL. Global Equivalent Layer

GIS. Geographic Information System

HiRISE. High Resolution Imaging Science Experiment

LIBS. Laser-Induced Breakdown Spectroscopy

MAHLI. MArs Hand Lens Imager

MARDI. MARs Descent Imager

MastCam. Mast Camera

MOLA. Mars Orbital Laser Altimeter

MSL. Mars Science Laboratory

NASA. National Aeronautics and Space Administration

Navcam. Navigation Camera

PDS. Planetary Data System

RDR. Reduced Data Record

THEMIS. Thermal Emission Imaging System

TIN. Triangulated Integrated Network

USGS. United States Geological Survey

XRD. X-Ray Diffraction

Chapter 1

Introduction

1.1 Sedimentary Records on Earth and Mars

The sedimentary rock record contains the history of the changing surface of the planets. Sediments can be transported whenever the wind blows or water moves, and, when these sediments accumulate and are preserved as rock, they record the story of their formation: the accumulated grains reveal the type of rocks that were upstream or upwind, the size and shape of the grains indicates the manner in which they were deposited, fossils preserve remains of life, chemical weathering of grains relates to the climate, cementation that turns grains into rock reveals the groundwater chemistry, and cracks or fractures tell the story of stresses applied to the rock and the environment when they healed. Studying the sedimentary rocks therefore enables us to tell the story of a location, and in some cases, the story of the planet. Planet-scale changes can be recorded globally in the rock record from that time; on Earth, the geochemistry of marine shales records — to name a few examples — the evolution of continental crust [*Taylor and McLennan*, 1995], the oxidation of the atmosphere due to photosynthesis [*Canfield*, 2005; *Falkowski and Isozaki*, 2008], major extraterrestrial impacts [*Alvarez et al.*, 1980], and the uplift of the Himalayas [*Palmer and Edmond*, 1989]. On Mars, we seek understanding of both local and global phenomena through our study of the sedimentary rock record.

Until recently, it was unclear whether Mars even had a sedimentary record—the planet today is dry and the lack of plate tectonics implies a lack of the burial and uplift processes typical of sedimentary rock formation on Earth [e.g. *Worden and Burley*, 2003]. Sediment production on Mars was suggested based on observations of channels [*Sharp and Malin*, 1975], windblown sediment [*McCauley*, 1973], and layered deposits [*Murray et al.*, 1972; *Soderblom et al.*, 1973] in early Mariner 9 imagery, but the presence of a sedimentary record was not established until a seminal paper by Malin and Edgett in 2000, which used Mars Orbital Camera images to identify and describe sedimentary deposits distributed across the surface of Mars [*Malin and Edgett*, 2000]. A few years later, the volume and resolution of data available increased exponentially with a series of successful orbiter and rover missions, providing confirmation of the presence of significant sedimentary deposits from both rover [*Squyres et al.*, 2004; *Grotzinger et al.*, 2005; *McLennan et al.*, 2005] and orbital [*Jerolmack et al.*, 2004; *Fassett and Head*, 2005] perspectives, and evidence for their association with water-lain minerals [*Bibring et al.*, 2005; *Poulet et al.*, 2005; *Bibring et al.*, 2006; *Ehlmann et al.*, 2008a; *Ehlmann et al.*, 2008b; *Mustard et al.*, 2008].

Now that the presence of a sedimentary record in Mars has been established [*Malin and Edgett*, 2000; *McLennan and Grotzinger*, 2008b; *Grotzinger and Milliken*, 2012], we seek to understand the episodes of global change through time that are recorded therein. While specific changes are best observed at the rover-scale, site selection must be accomplished based on global trends, established by orbital observations. Martian surfaces are dated based on the density of craters, calibrated (with considerable uncertainty) by comparison with cratered surfaces on the moon, from which we have samples that have been radiometrically dated [*Hartmann and Neukum*, 2001]. Mars offers a unique record compared to Earth because most of the Martian sedimentary rock record is more than 3 billion years old [*Tanaka et al.*, 2014], whereas it is difficult to find unmetamorphosed ancient sedimentary rocks on Earth. Bibring et al. [2006] pointed out that, to first order, the orbitally-mapped mineralogies of Martian rocks are related to their age, where phyllosilicate clays are most often associated with the oldest Noachian-era surfaces (4.5-~3.8 Ga), sulfates and other salts are associated with Hesperian-era surfaces (~3.8-3.3 Ga), and dry dusty iron-oxides are associated with Amazonian surfaces (~3.3 Ga-present) [*Bibring et al.*, 2006; *Ehlmann and Edwards*, 2014]. While this scheme is simplified, it highlights major mineralogical changes worth investigating in the sedimentary record; perhaps the transitions between these clay-rich, salty, and dry eras will reveal the global changes that shaped Mars. Furthermore, phyllosilicate clays are of special interest because of their potential for preserving organic molecules. At the time when landing sites for Mars Science Laboratory (MSL) were being chosen, only one site was found where rover-accessible layered sedimentary deposits recorded the transitions between phyllosilicates, sulfate-rich deposits, and iron oxides [*Grotzinger and Milliken*, 2012], so the Gale crater site was selected for further investigation of the sedimentary record of environmental transitions on Mars.

1.2 Gale Crater

Gale crater is a 154 km-diameter crater sitting on fluvially-dissected Noachian terrain along the dichotomy boundary that divides the southern highlands from the northern lowlands of Mars. It is an example of a class of craters identified and mapped by Malin and Edgett as a partially-filled crater with layered interior deposits, which in this case form a mound that extends higher than the northern crater rim [*Malin and Edgett*, 2000]. This mound likely surrounds the crater's central peak and, based on other similar craters, is likely an erosional remnant from a more complete crater fill [*Malin and Edgett*, 2000; *Grotzinger et al.*, 2015]. The layers exposed on the mound, called Mount Sharp (formally Aeolus Mons), were mapped in higher resolution by Anderson and Bell [2010] and the mineralogy associated with each layer was described in Milliken et al. [2010] in anticipation of Gale crater being a potential landing site for MSL.

Mount Sharp is just over 5 km tall, and has a significant unconformity about 1.3 km above the modern crater floor that separates the lower formation from the upper formation. The lower formation includes a thin phyllosilicate clay-bearing layer about 100 m above the base of the mound and a thick sequence of sulfate-bearing layers above the phyllosilicates [*Milliken et al.*, 2010]. In addition to these mineralogical indicators of water-rich sedimentation, there are channels indicating water flow from the base of the unconformity to the bottom of the mound, and a variety of fluvial channels leading into the crater [*Anderson and Bell*, 2010; *Palucis et al.*, 2014]. Within the sulfate-bearing layer, about 1 km above the floor of the mound, there are boxwork deposits that were identified by Anderson and Bell [2010] and are discussed in detail in Siebach and Grotzinger [2014a] (Chapter 2), which require significant volumes of groundwater to have fluxed through at this elevation of Mount Sharp. The MSL rover *Curiosity* landed on the floor of the crater, called Aeolus Palus, and has traversed to the base of Mount Sharp and up through about 40 meters of the stratigraphy, but has not yet (as of May, 2016) reached the phyllosilicate-bearing unit identified from orbit.

1.3 Mars Science Laboratory

The Mars Science Laboratory *Curiosity* rover is the most complex rover ever sent to the surface of Mars. It is 900 kg, 2.2 m tall, has a 1.9 m long robotic arm, and has eleven science instruments for in-situ data collection and analysis. Of relevance to the work presented here, these include stereo black and white navigation cameras (NavCam); stereo true-color mast cameras (MastCam); a Laser-Induced Breakdown Spectrometer (LIBS; ChemCam instrument) for remote compositional analyses at fine resolution; a robotic arm equipped with a drill for sampling, a high-resolution camera (MAHLI), and an Alpha-Particle X-ray Spectrometer (APXS) for quantitative compositions of 1.7-cm diameter spots; and an X-Ray Diffractometer (XRD) for crystalline mineralogy in the Chemistry & Mineralogy experiment onboard (CheMin) [*Grotzinger et al.*, 2012].

Since *Curiosity* successfully landed at Bradbury Rise in Aeolus Palus on 6 August 2012, *Curiosity*'s operations on Mars have been directed by the ~500 member MSL Science and Operations team on Earth. Work for this thesis incorporates *Curiosity*'s observations through sol 1300 (i.e., April 3, 2016).

1.4 Thesis Summary

Gale crater has been identified as one of the key sedimentary sections on Mars since sedimentary rocks were identified on that planet [*Malin and Edgett*, 2000]. With detailed orbital imagery and significant volumes of rover data now available for Gale crater, we are able to investigate the sedimentary record of Mars in unprecedented detail. The chapters in this thesis are designed to understand the formation and diagenesis of the sedimentary rocks in Gale crater encountered during each stage of the MSL mission.

Prior to *Curiosity*'s landing, orbitally-based imagery was used to map an extensive layer of boxwork deposits in Mount Sharp, which are discussed in chapter 2 with implications for the formation of the mound itself and the importance of groundwater. After landing, *Curiosity* drove to and investigated the lowest elevation unit in the floor of Aeolus Palus, which was a mudstone called the Sheepbed formation. Chapter 3 is a detailed investigation of diagenetic synaeresis cracks in the mudstone, which contributed to the interpretation of the Sheepbed formation as a once-habitable lake environment [*Grotzinger et al.*, 2014]. After investigating the Sheepbed mudstone, *Curiosity* drove another 9 km across Bradbury group fluvio-deltaic sediments exposed in Aeolus Palus. Chapter 4 presents a grain-size based classification scheme for the Bradbury group rocks analyzed by *Curiosity* and shows that the geochemistry of these rocks is mostly related to mineral sorting based on grain size during fluvial transport. On sol 750 (i.e., September 14, 2014), *Curiosity* reached the base of Mount Sharp and began investigating the Murray formation, another mudstone formed in an ancient lake that is interfingered with the Bradbury group sediments. Since then, *Curiosity* has also been analyzing samples from the Stimson formation, an eolian sandstone that unconformably drapes over the Murray mudstone at the base of Mount Sharp. Chapter 5 compares geochemical trends in the Bradbury fluvio-deltaic sediments, the Murray mudstone, and the Stimson eolian sandstone, focusing on our understanding of the source rocks around Gale crater based on clastic input to each of these formations, which sample different areas due to their distinct transport and depositional environments.

Chapter 2

Volumetric Estimates of Ancient Water on Mount Sharp Based on Boxwork Deposits, Gale Crater, Mars

Kirsten L. Siebach and John P. Grotzinger

This chapter is published as:
Siebach, K. L., and J. P. Grotzinger. (2014) Volumetric Estimates of Ancient Water on Mount Sharp Based on Boxwork Deposits, Gale Crater, Mars. *J. Geophys. Res.,* online 28 Jan 2014, doi: 10.1002/2013JE004508.

Key Points

- Boxwork structures on Aeolus Mons (Mount Sharp) are identified and mapped
- Minimum water volume required for boxwork calculated from water-to-cement ratio
- Implications for Mount Sharp formation are discussed

Abstract

While the presence of water on the surface of early Mars is now well-known, the volume, distribution, duration, and timing of the liquid water have proven difficult to determine. This study makes use of a distinctive boxwork-rich sedimentary layer on Mount Sharp to map fluid-based cementation from orbital imagery and estimate the minimum volume of water present when this sedimentary interval was formed. The boxwork structures on Mount Sharp are decameter-scale light-toned polygonal ridges that are unique compared to previous observations of Martian fractured terrain because they are parallel-sided ridges with dark central linear depressions. This texture and the sedimentary setting strongly imply that the ridges are early diagenetic features formed in the subsurface phreatic groundwater zone. High resolution orbital imagery was used to map the volume of light-toned ridges, indicating that a minimum of $5.25*10^5$ m^3 of cement was deposited within the fractures. Using a brine composition based on observations of other Martian cements and modeling the degree of evaporation, each volume of cement requires 800 – 6700 pore volumes of water, so the mapped boxwork ridge cements require a minimum of 0.43 km^3 of water. This is a significant

amount of groundwater that must have been present at the -3620 m level, 1050 m above the current floor of Gale Crater, providing both a new constraint on the possible origins of Mount Sharp and a possible future science target for the *Curiosity* rover where large volumes of water were present and early mineralization could have preserved a once-habitable environment.

2.1 Introduction

The past decade of rover and orbiter missions make the influence of liquid water on the surface environment of ancient Mars very clear [*Malin and Edgett*, 2003; *Squyres et al.*, 2004; *Bibring et al.*, 2006; *McEwen et al.*, 2007b; *Murchie et al.*, 2009]. However, the volume of water that was once available on the surface of Mars, and which likely was subsequently lost to space [e.g. *Jakosky*, 1991], sequestered as ice caps and frozen grounds [e.g. *Plaut et al.*, 2007], or incorporated in rocks and minerals [e.g. *Mustard et al.*, 2012], etc., is much debated. An early estimate that attempted to approximate the surface water inventory based on the cumulative volume of sediment excavated by the numerous outflow channels and valley networks on Mars indicated that a minimum 500 m global equivalent layer (GEL) of water must have been present on early Mars [*Carr*, 1987]. Other estimates have considered the volume of water needed to fill the northern ocean (100 m GEL) [e.g. *Head et al.*, 1999], the amount of water integrated into hydrated minerals (150-1800 m GEL) [*Mustard et al.*, 2012], or the total amount of hydrogen lost to space (95-99% of initial inventory) [*Jakosky*, 1991]. These large-scale estimates serve as a starting point for more specific discussion of local phenomena that may have contributed to regional water budgets.

Recent approaches to quantifying past water abundances exploit the increased resolution of recent orbiter missions to focus, for example, on well-defined geomorphic features that permit better constraints and allow modeling of the minimum water volumes required to form those features, including channels [e.g. *Baker and Milton*, 1974; *Burr et al.*, 2009], basins [e.g. *Goldspiel and Squyres*, 1991; *Jerolmack and Mohrig*, 2007], and alluvial fans or deltas [e.g. *Di Achille and Hynek*, 2010]. These smaller-scale, better constrained, conservative calculations are particularly useful when coupled with mineralogic evidence for water or when they provide context for larger sedimentary or geologic structures [e.g. *Jerolmack et al.*, 2004; *DiBiase et al.*, 2013] et al. Here, we evaluate a site where groundwater flowed through fractured rock and precipitated cements that formed large-scale boxwork structures. These structures enable estimation of water volumes required to form a specific interval of the sedimentary layers that comprise Aeolus Mons (informally known as Mount Sharp) in Gale Crater. The calculation of water volume at this height, many hundreds of meters above the current crater floor, places important constraints on processes occurring during diagenetic modification of Aeolus Mons. Furthermore, this site is characterized by a once water-rich environment that underwent early mineralization, which is known on Earth to help facilitate preservation of once-habitable environments [*Grotzinger et al.*, 2012]. This is therefore recommended as a priority target for the *Curiosity* rover that successfully landed at the base of Mount Sharp in August 2012.

2.2 Boxwork Structures: Mapping observations and formation discussion

2.2.1 Methodology

Mapping of the boxwork texture was accomplished using orbital imagery available through the NASA Planetary Data System. The gridded topographic dataset (463 m/pixel) from the Mars Orbiter Laser Altimeter (MOLA) instrument onboard the Mars Global Surveyor [*Smith et al.*, 2003] was used as a reference for correlating orbital data over the fractures. Thermal Emission Imaging System (THEMIS) global IR daytime imagery (232 m/pixel) was correlated to the MOLA reference, Context Camera (CTX) images (6 m/pixel) were correlated to the THEMIS reference, and finally High Resolution Imaging Science Experiment (HiRISE) imagery (25 cm/pixel) was correlated to the CTX images. The fracture networks were identified in the HiRISE images and exposures of the fractures were mapped over approximately 1 km^2.

HiRISE Digital Terrain Models (DTMs, 1 m/pixel) provided by the U. S. Geological Survey (USGS) [*Mattson et al.*, 2011] were co-registered where available to determine fracture elevations and stratigraphic relationships. The USGS creates DTMs based on the method described in [*Kirk et al.*, 2008]. The absolute elevations of these

DTMs is determined by comparison to MOLA elevations, and is accurate to within a few tens of meters, but the expected vertical precision (EP) within the DTM can be calculated based on the viewing geometry and resolution of the HiRISE image [*Kirk et al.*, 2008]. For the two DTMs used in this study, the EP, assuming 0.2-pixel matching error, is 7 cm for DTEEC_001488_1750_001752_1750_U02 and 15 cm for DTEEC_019698_1750_019988_1750_U01. Relative elevations within the fractured bed were determined using the HiRISE DTMs, and absolute elevations to compare with the landing site were determined by comparing averaged HiRISE DTM and MOLA gridded values over the mapped fracture networks to the MOLA-based landing site elevation. Fractures were mapped to the limit of resolution of HiRISE 25-cm-pixels, so ridges were detectable if they were about 50 cm across, and their heights could be measured to within about 10 cm based on DTM resolution.

2.2.2 Observations

Resistant fracture networks (boxwork textures) on Mount Sharp were first identified during Mars Science Laboratory (MSL) landing site assessment [*Thomson and Bridges*, 2008; *Thomson et al.*, 2011]. Anderson and Bell placed the fractures in the context of geomorphologic units based on HiRISE mapping, noting that the best-developed cemented fractures are in a dark-toned layered unit [*Anderson and Bell*, 2010]. Stratigraphically, these cemented fracture exposures are found in the upper member of the lower formation of the mound strata (Figure 2.1), which exhibits a spectral signature dominated by sulfates [*Milliken et al.*, 2010] and has a thermal inertia of 260 to 420 $Jm^{-2}K^{-1}s^{-1/2}$ [*Fergason et al.*, 2012].

Mapping of the boxwork texture in this study revealed that it is exposed in a stratigraphic interval at an average elevation of -3620 +/- 50 m with reference to the geoid. This interval is approximately 880 m above the Bradbury Rise landing site for MSL *Curiosity* [*Parker et al.*, 2013], and 1050 m above the current base-level in Gale Crater [*Anderson and Bell*, 2010]. The upper limit of boxwork-containing strata is sharply bounded and coincides with a bedding plane. The interval is abruptly overlain by light-toned strata that lack the boxwork texture. In contrast, the lower boundary of boxwork-

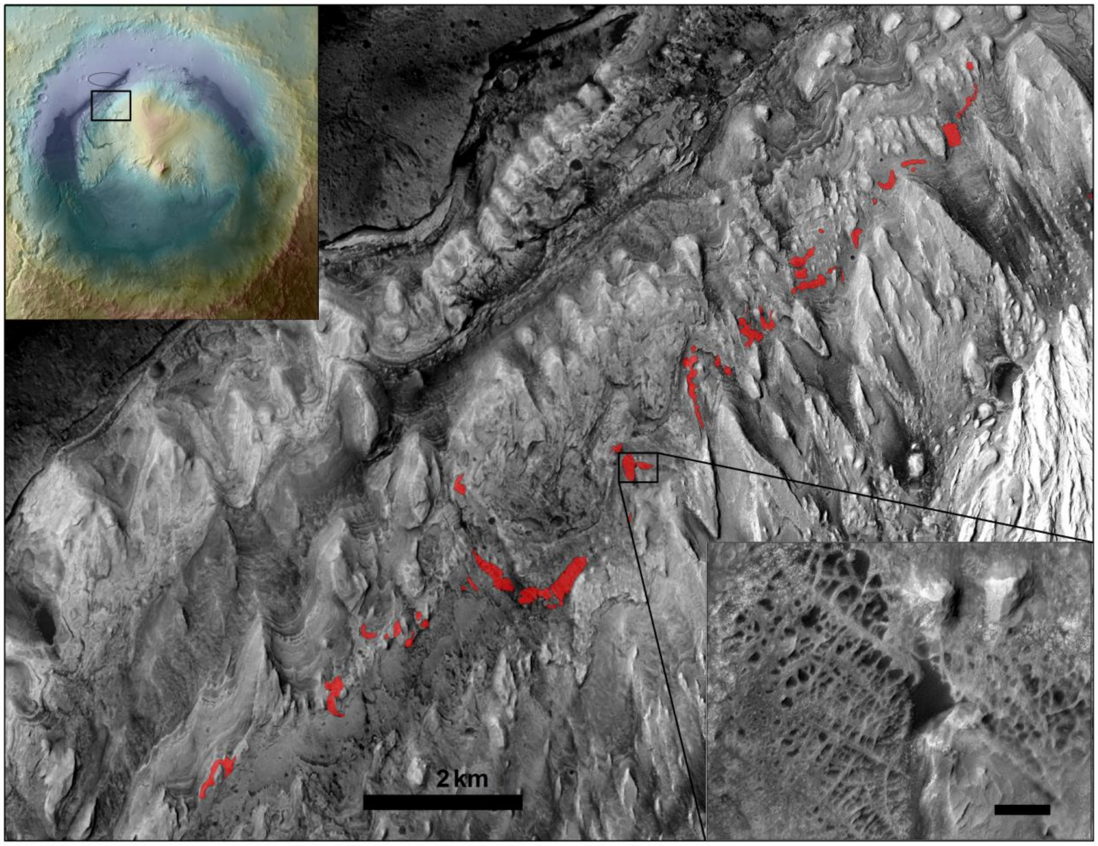

Figure 2.1 Overhead Map of Boxwork Structures
Map of the mapped boxwork structures (red) within the Gale Crater stratigraphy on CTX mosaic with 2 km scale bar. Upper left map of Gale crater shows High Resolution Stereo Camera imagery draped on MOLA topography. Gale crater is 155 km in diameter for scale. Lower right inset shows detail of boxwork structures with a 50 m scale bar. HiRISE images used for mapping include: ESP_012551_1750, ESP_019698_1750, and (inset) PSP_001752_1750. Images centered at 137.302088° E, 4.875233° S.

containing strata is diffuse; boxwork textures gradually dissipate downward through ~40 m of strata as measured in two visible sections in HiRISE DTMs (e.g. Figure 2.2e). Although exposure is intermittent, the boxwork texture can be traced through more resistant intervals. The boxwork-bearing unit is primarily exposed along cliff faces and in open-ended topographic lows between resistant outcrops of the capping unit (Figure 2.3). The light-toned ridges that help define well-developed boxwork textures are fairly densely spaced; these ridges make up an average of 35% of the surface area in these sections (ranging from ~20-50%, Figure 2.2a-d).

The geometry of the fracture network that defines the boxwork texture is delineated by the trends of light-toned ridges, expressed in raised relief. Fractures are mostly straight, however the longest fractures often show slight curvature (e.g. Figure 2.2a-d). The fractures tend to intersect at 90-degree angles and show a preferred orientation; secondary fractures often end when they intersect primary fractures, although secondary fractures may cross-cut primary fractures. The fracture networks are less well-organized at deeper stratigraphic levels, showing increasing fracture curvature and greater intersection angles (Figure 2.2e-f). Ridge widths vary between exposures, but they average about 5 m in width. Some light-toned ridges show a dark line running down the center of the ridge, which varies in width up to 1.5 m (Figure 2.4).

The hollows between elevated boxwork-defining fractures are filled with dark sediment that forms dunes in larger accumulations. These hollows tend to be quasi-circular in plan-view and range in diameter from tens of meters to below one meter, with an average of ~10 m. HiRISE DTMs were used to measure the elevation difference between ridge tops and the middle of the hollows. In many cases the hollows were quite shallow or filled with sand and there was not a measureable difference in elevation. For 25 profiles where there was a measureable difference in elevation, the average elevation difference was 0.4 m, and the elevation differences typically ranged from 0.1 m to 1.0 m (see Figure 2.4). The maximum elevation difference found was 3.5 m between the ridge and hollow.

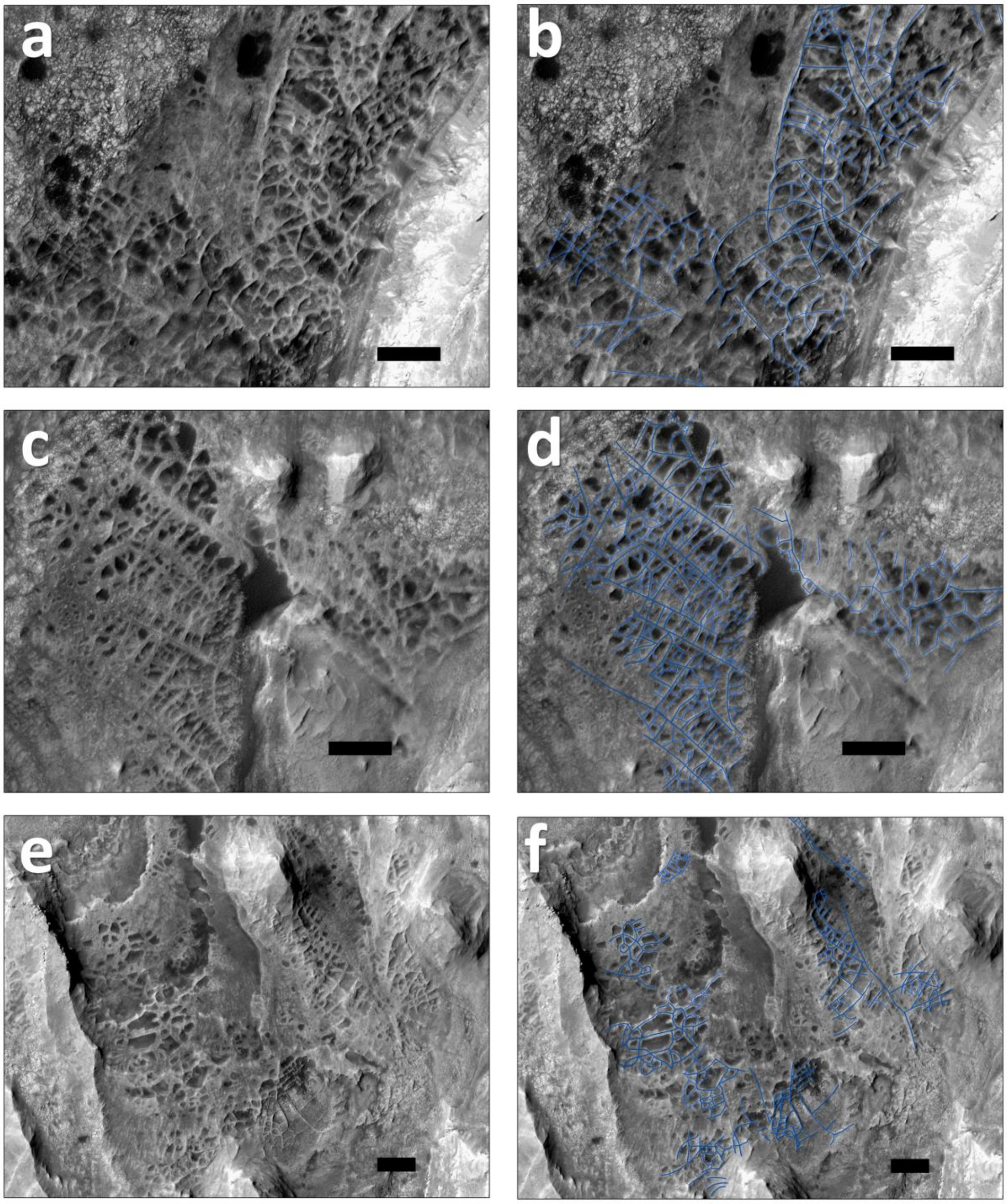

Figure 2.2 Boxwork Structure Morphologies
Images on right (b, d, and f) show outlines tracing the center of the light-toned raised ridges (original fracture network). Scale bar in all images is 50 m, north is up. All images from HiRISE frame PSP_001752_1750. Note clear primary and secondary fracture directions near top of stratigraphic layer (frames c and d) and increasing fracture curvature with depth in the stratigraphy (as shown in a, b, e, and f). Center latitude and longitude of each image pair listed here: (a, b) 137.288197E, -4.900521S, (c, d) 137.302600E, -4.876048S, and (e, f) 137.328993E, -4.845897S.

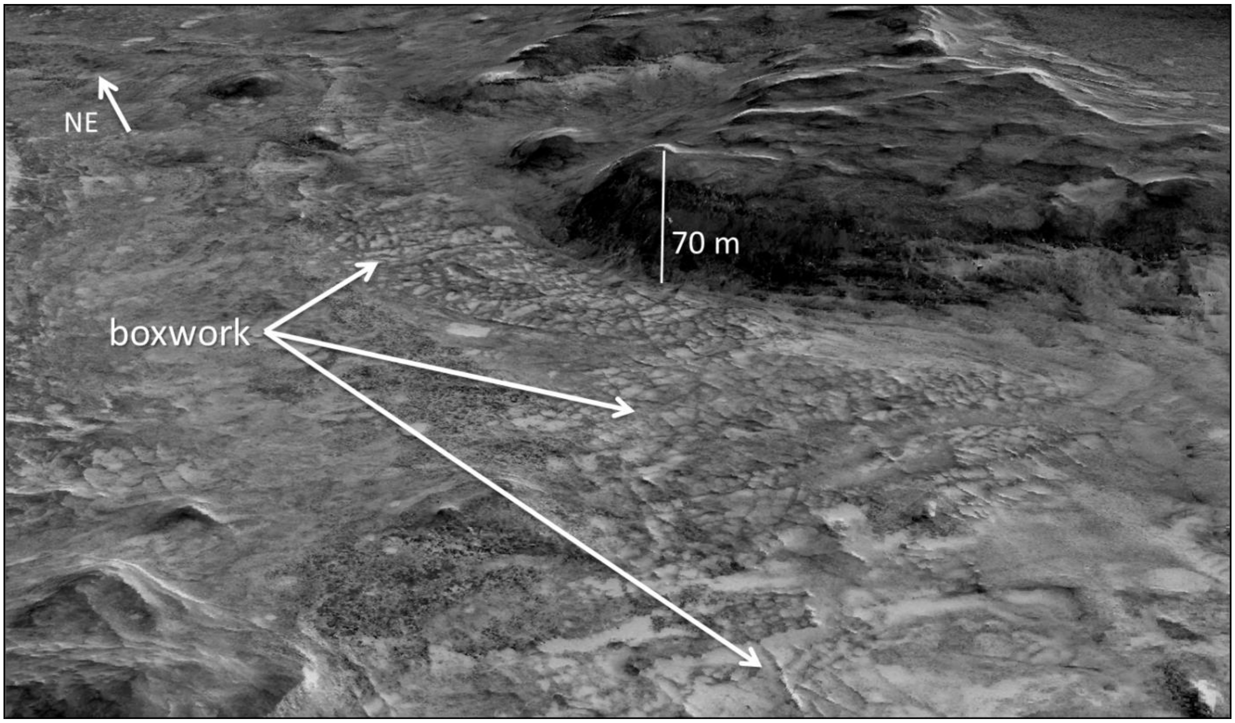

Figure 2.3 Perspective View of Boxwork from HiRISE DTM [DTEEC_001488_1750_001752_1750_U02] of boxwork structures in stratigraphy. Note that the fractures do not continue into the capping unit.

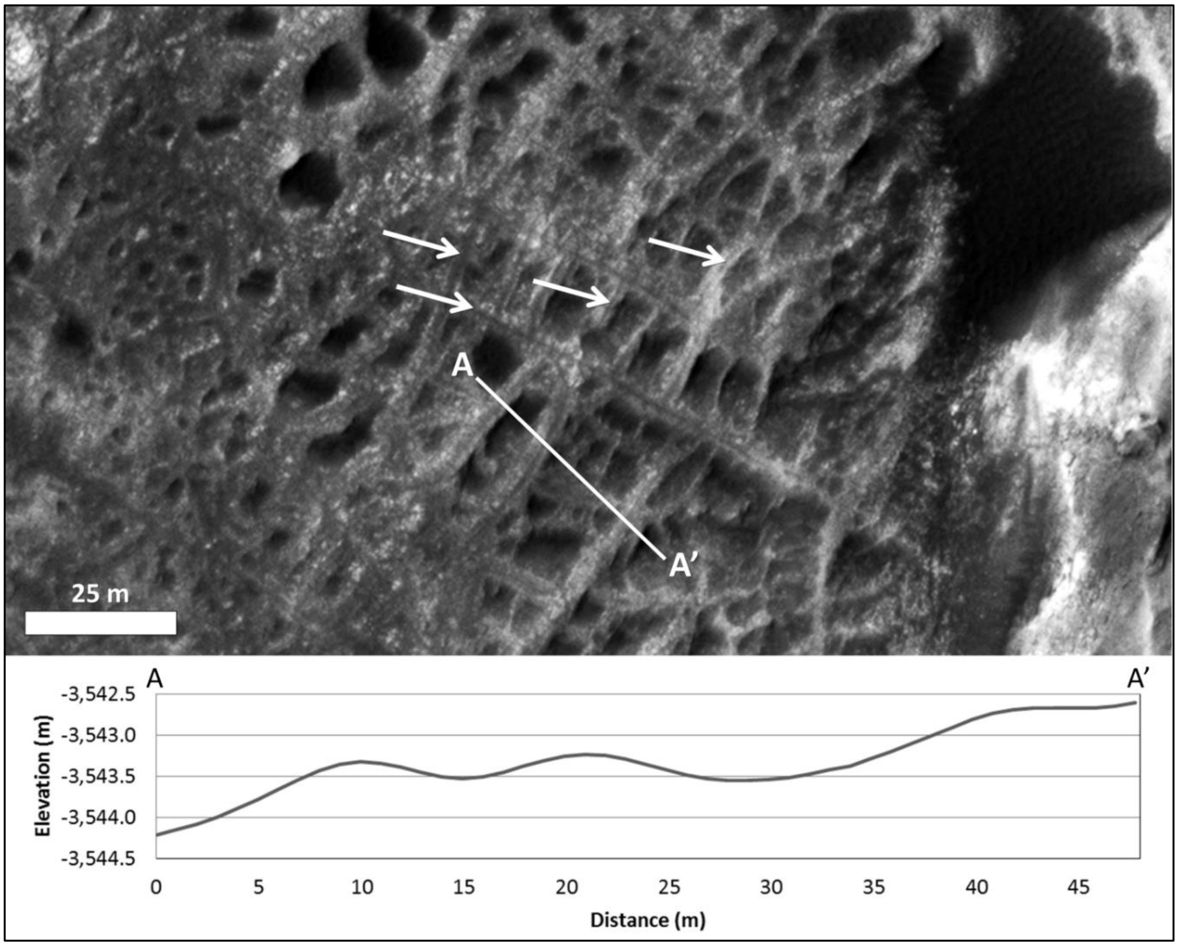

Figure 2.4 Detail of Boxwork Structures

Detail of boxwork structure, showing dark lines in ridge centers. Profile shows that relief between ridges and hollows is on the order of a few tens of centimeters.

2.2.3 Boxwork Formation Discussion

The boxwork texture is defined by light-toned, decameter-scale, polygonal ridge networks. The distinctive attribute of these light-toned ridges as compared to other fracture networks observed from orbit on Mars is that they are parallel-sided with dark center lines that demarcate either linear central depressions or later cements. This texture strongly implies that the ridges are post-depositional diagenetic features formed in the subsurface when mineral-saturated groundwater flowed through fractured, lithified rock, and cement precipitated within fractures and pores. The parallel walls of the filled fractures are comparable to "isopachous" void-filling cements described commonly in rocks on Earth, where minerals create linings, or coatings, along the margins of voids – be they fractures or intergranular pore spaces. Such isopachous cements form when the void is within the phreatic (water-saturated) zone [*Tucker*, 2009]. This differential cementation makes the fractures more resistant to erosion than the less cemented host rock, and thus the fracture fills stand as topographically higher rims around the eroded host rock (Figure 2.1).

Boxwork formation implies a series of post-depositional processes: sediment was lithified and fractured, then saturated fluids percolated through the fracture network and cemented fractures and residual pore spaces in the subsurface, finally the boxwork interval was exhumed and erosion of the less-indurated rock formed the now exposed polygonal ridges. These observations help to clarify the series of events at this stratigraphic interval on Mount Sharp.

The presence of fractures in a distinct stractigraphic successsion, with increasing organization towards the top of that succession, and the absence of similar fractures in overlying strata imply that this stratum was already lithified and then exposed at the surface when the fracturing occurred. Lithification on Mars is not well understood, but in general, compaction by burial decreases porosity of sediments and fluids cement and lithify sediments [*Grotzinger and Milliken*, 2012]. Conceivably, this boxwork-bearing interval could have been buried, infiltrated by cementing fluids, and converted from sediment to rock, prior to exhumation and fracturing.

The fracture geometry helps narrow down the cause of fracturing. In general, large non-tectonic surface fractures originate from contraction, impact processes, loading and unloading of lithospheric stresses, jointing, or fluid pressure [*Long et al.*, 1996]. Jointing and fluid pressure are ruled out by stratigraphic relationships—the fracturing occurred at the surface—and impact processes are ruled out by the systematic organization of fractures (Figure 2.2). Contraction processes are the most likely to have formed the fractures. The observed orthogonal fracture patterns indicate that the fractures did not form in extended freeze/thaw cycles, which create 120-degree joints over 10^6-year time scales [*Sletten et al.*, 2003]. Rather, the fracture geometry is most similar to those formed in non-cyclic isotropic or slightly non-isotropic contraction stress fields [*Olson et al.*, 2009], which could be related to sediment desiccation or more intense short-term freezing of lithified sediment [*Long et al.*, 1996].

After lithification and fracturing, the voids in the host rock and fractures are inferred to have been filled with a second generation of cement. The dark line in the center of the ridges helps delineate the parallel-sided or "isopachous" nature of precipitated fracture-filling minerals along the walls of the fractures (e.g. Figure 2.4). The isopachous morphology of the light-toned elevated ridges is consistent with cementation in the phreatic groundwater zone, where cement formation occurs evenly on all available surfaces.

Approximations of the water volume required to form the ridges depend on the relative proportion of primary host rock, and secondary cements forming the raised ridges. Two scenarios are proposed for the relative proportions of primary rock and secondary cement in the light-toned ridges: (1) the ridges are primarily composed of extensive secondary cements filling pores and fractures, or (2) the ridges are mostly composed of the host rock, hardened by an early cement within the pore spaces. For either case, there are then two options for the dark central lineations in the ridges; the dark lines could represent residual porosity in the fracture network that was back-filled with wind-blown dark sand or dark-toned cement that completely fills the fracture void. Since the dark central lines are a relatively minor component of the ridges, the primary distinction between these scenarios is whether the light-toned ridges are mostly cement or if they are host rock with pore-occluding cement, perhaps ~30% cement fill. Orbital data cannot discriminate between these two scenarios. However, in either case, the observed boxwork represents a significant volume of cement precipitated from groundwater.

Polygonal ridges, albeit at a much smaller scale, were originally analyzed and described in Wind Caves, South Dakota, where the term "boxwork" structures was coined [*Bakalowicz et al.*, 1987]. Large-scale intersecting filled fracture networks are also present in sulfate-bearing units in Candor Chasma [*Okubo and McEwen*, 2007] and northeast Syrtis Major [*Ehlmann and Mustard*, 2012], but the structures within Mount Sharp are distinguished as a dense, parallel-sided network of filled-fracture boxwork structures.

Alternative formation hypotheses for the boxwork were considered, but they do not explain the observed fracture characteristics and the dark line in the center of the ridges. Volcanic dikes, for example, could also leave raised ridges post-erosion, but these often form in clusters or irregular parallel geometries [*Hoek*, 1991], and this formation mechanism does not explain the centered dark lines. Some freeze-thaw thermal contraction polygons have dark central lines that demarcate accumulations of loose sediments between ice polygons, and the edges of the ice polygons may accumulate raised shoulders, but the central linear depressions (sand wedges) are generally wider than the raised polygon shoulders [*Sletten et al.*, 2003]; this does not match the measured elevated ridges described here. Finally, boxwork patterns could be similar to large-scale honeycomb or tafoni salt-weathering patterns [*Rodriguez-Navarro*, 1998], but this is unlikely because of the high ridge width relative to hollows and the albedo variation in the ridges. Based on the fracture geometry, presence of sulfates, ridge characteristics, and local geomorphic features consistent with water-induced bedrock erosion [*Anderson and Bell*, 2010], the cementation-based hypothesis for boxwork formation is accepted as the most likely interpretation.

2.3 Fluid Volume Calculation

Quantitative estimates of water flow on Mars are essential to understanding water-rock interactions that inform an understanding of diagenesis and alteration, as well as habitability. At Gale Crater, these estimates would help provide context for *Curiosity's* mission of exploration. The boxwork structures described here constitute an unusual opportunity where quantitative measurements of a volume of diagenetic cements can be acquired from orbital imagery. Cement volumes can be related to the volume of water required to deposit the cement if a few simple assumptions are made about the ion saturation of the groundwater and the degree of evaporation of the brine. An approach to fluid pore-volume calculations based on terrestrial studies of carbonate cementation is employed here to determine the water volume required to deposit the mapped cements [*Bethke,* 1985; *Banner and Hanson,* 1990]. Although the cement composition of the ridges was not uniquely determined from orbit, previous observations of evaporite deposits on Mars by the *Opportunity* rover [*Grotzinger et al.*, 2005; *McLennan et al.*, 2005] have constrained models of Martian brines. Here we use an evaporation model derived from acid-sulfate weathering of synthetic Martian basalts and constrained by the *Opportunity* rover findings in Meridiani Planum [*Tosca*, 2004; *Tosca et al.*, 2008].

Calculation of the minimum volume of water required to form the boxwork layer is based on the following equation:

$$\frac{V_{water}}{V_{cement}} = \left[\sum_{minerals} \left(\frac{m_{mineral}}{V_{brine} * \rho_{mineral}} \right) \right]^{-1} , \qquad (1)$$

where the volume of cement (V_{cement}) is derived from mapping of orbital imagery and the minerals precipitated are derived based on a reasonable model for evaporation of a Martian brine [*Tosca et al.*, 2008]. The volume of water (V_{water}) evaporated per volume of cement precipitated (V_{cement}), or unitless “pore volume,” is calculated for a given degree of brine evaporation based on the volume of precipitated minerals ($m_{mineral}/\rho_{mineral}$) per volume of water in the initial brine (V_{brine}). The results of this calculation are shown in in Figure 2.5, where pore volumes of water (V_{water}/V_{cement}) are plotted against percent of water evaporated (V_{water}/V_{brine}). The plot seems to approach an asymptote, indicating that more water evaporation does not immediately lead to more cement precipitation, at two times; first after the precipitation of jarosite, gypsum, copiapite, and bilinite, and later after the precipitation of epsomite, melanterite, anhydrite, and halite [*Tosca et al.*, 2008]. Points near the two asymptotes are selected to describe the range of pore volumes of water that would be required to deposit the cement volume. As indicated in Figure 2.5, if 99% of the starting brine evaporates, then 6,700 pore volumes of water are required, or (based on the last point in the modeled evaporation sequence) if 99.97% of the brine evaporates, 800 pore volumes of water are required to form the cements. These values fit well in the range of pore volumes estimated for terrestrial porosity occlusion scenarios [*Bethke*, 1985; *Banner and Hanson*, 1990].

To obtain a minimum estimate for the water volume, the volume of cement is derived from the surface area of ridges within the mapped HiRISE unit, 0.35 km^2, multiplied by the thickness of the resistant boxwork layers in the vertical stratigraphy, 5 m, giving a minimum cemented ridge volume of 1.75 x 10^6 m^3. This is a conservative estimate as the boxwork can be traced vertically through up to 40 m of stratigraphy in some locations and may well extend laterally for some distance into the subsurface beneath Mount Sharp, based on continuity of stratigraphy around the entire mound [*Milliken et al.*, 2010]. Two endmember hypotheses were used to calculate the cement volume based on the ridge volume: ridges are 100% cement (cements occur within fractures), or ridges are 30% cement by volume (cements occlude pores within primary rocks adjacent to fractures). The pore-occluding scenario is comparable to several analogous locations on Earth, where rocks in close proximity to a fracture or fault can become strongly cemented, forming diagenetic “halos” [*Knipe*, 1992; *Nelson et al.*, 1999]. Assuming 99.97% of the brine evaporates, the fracture-filling scenario requires a minimum of 1.4 km^3 of water, and the pore-occluding scenario requires 0.42 km^3 of water to form the measured ridges (Figure 2.5).

2.4 Implications for Mount Sharp Formation

These results are surprising because they imply a significant amount of water once percolated through pores in rocks 1050 m above the current base-level for Gale Crater. Several scenarios could deliver the required water, but this analysis must begin with several firm constraints: (1) the boxwork fabric is developed along a bedding plane that emerges from within the stack of layers that define Mt. Sharp, (2) the boxwork fabric terminates abruptly against the overlying stratum, but extends downward for several tens of meters, and (3) the isopachous element of the boxwork fabric indicates mineral precipitation in the phreatic zone, below the local groundwater table. These constraints require the boxwork to be an ancient feature, dating back to the time of sediment accumulation; development of

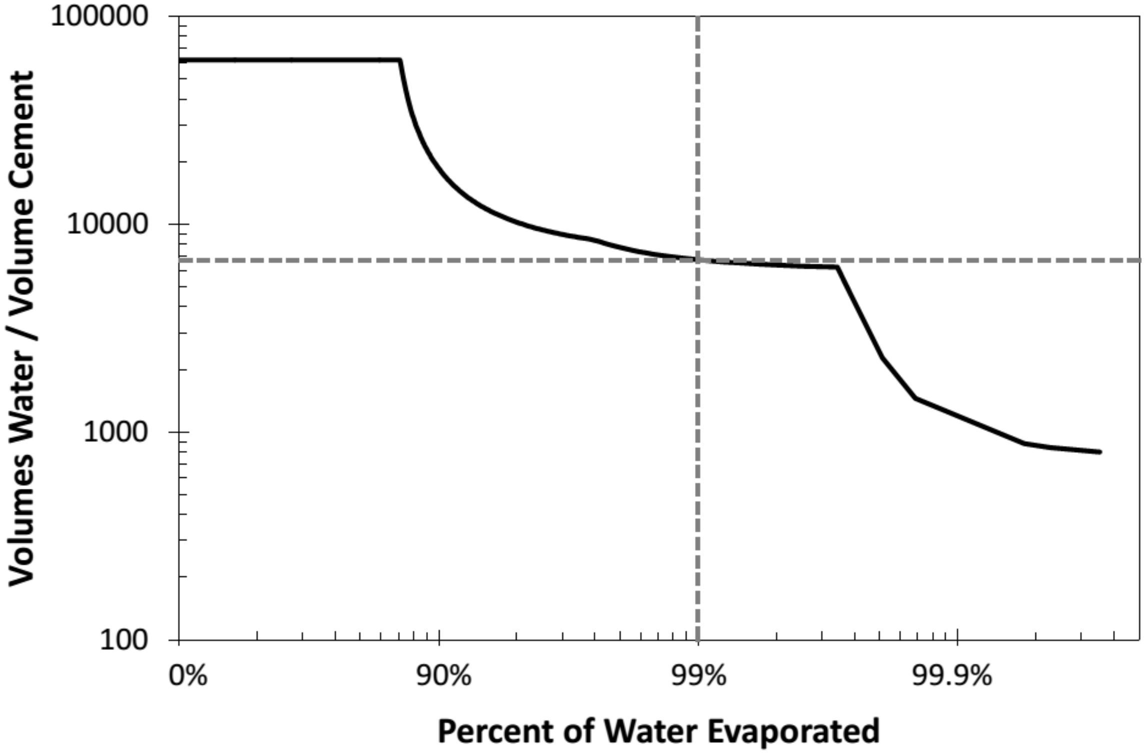

Figure 2.5 Plot of Required Volumes of Water per Volume Cement
Plot showing unit volumes of water evaporated per unit volume of cement precipitated (pore volumes of water) depending on the percent of water evaporated from a Martian brine model based on findings from the Mars Exploration Rover Opportunity [*Tosca et al.*, 2008]. The plot approaches an asymptote, indicating that more water evaporation does not immediately lead to more cement precipitation, twice; first after the precipitation of jarosite, gypsum, copiapite, and bilinite, and later after the precipitation of epsomite, melanterite, anhydrite, and halite [*Tosca et al.*, 2008]. Dotted line shows that if 99% of the brine evaporates, 6,700 pore volumes of water are required per unit of cement deposited. At the last point in the model, when 99.97% of the water has evaporated, only 800 equivalent volumes of water are required per volume of cement.

the fractures was terminated before the time of deposition of the overlying stratum; mineral precipitation occurred in the fractures in the phreatic zone, below the local groundwater table. This volume of groundwater-based cement indicates that the mound was formed not simply by eolian sediments cemented in minor wetting events [e.g. *Kite et al.*, 2013] but that instead there was extensive groundwater flow and aqueous processing of sediments involved in mound formation (see Figure 2.6).

Perhaps the simplest explanation is that the boxwork texture reflects groundwater supplied by atmospheric precipitation either as rain or snow; basin-filling strata accumulating within the lower elevations of Gale crater could have absorbed water in this fashion. The waxing and waning of water derived from seasonal or longer-term climatic cycles could have provided a mechanism for fracture formation [*Lachenbruch*, 1963]. However, this mechanism cannot account for the mineral abundance required to create the fracture-filling cements. Meteoric waters derived from rainfall or melting snow on the -3620 meter bedding plane surface would have been strongly undersaturated and almost certainly would have resulted in dissolution and karst formation given the high solubility of sulfate salts. In contrast, the evidence presented in this paper strongly supports mineral precipitation at this stratigraphic level. There is no evidence for dissolution fabrics which have been detected elsewhere based on remotely-sensed image data [*Belderson et al.*, 1978; *Manda and Gross*, 2006].

A derivative scenario assumes that Mt. Sharp had topographic expression at the time the boxwork-containing strata were accumulating and that precipitation occurred in those highlands. The recharge area underwent leaching to provide the ions required to cause mineral precipitation at some down-gradient distant site – for example, where the boxwork fabric is observed (Figure 2.6a-b). Mt. Sharp has considerable surface area and, depending on the mechanism for its formation, it is conceivable that its summit varied in position; the current summit is about 45 km southeast from the exposed boxwork bedding plane. The stratigraphic interval represented by the fracture network would have been within an aquifer, transporting these fluids down-gradient from the undersaturated recharge area. As fluids moved through this aquifer they would have become increasingly saturated due to dissolution of minerals along the way, and eventually re-precipitated these dissolved

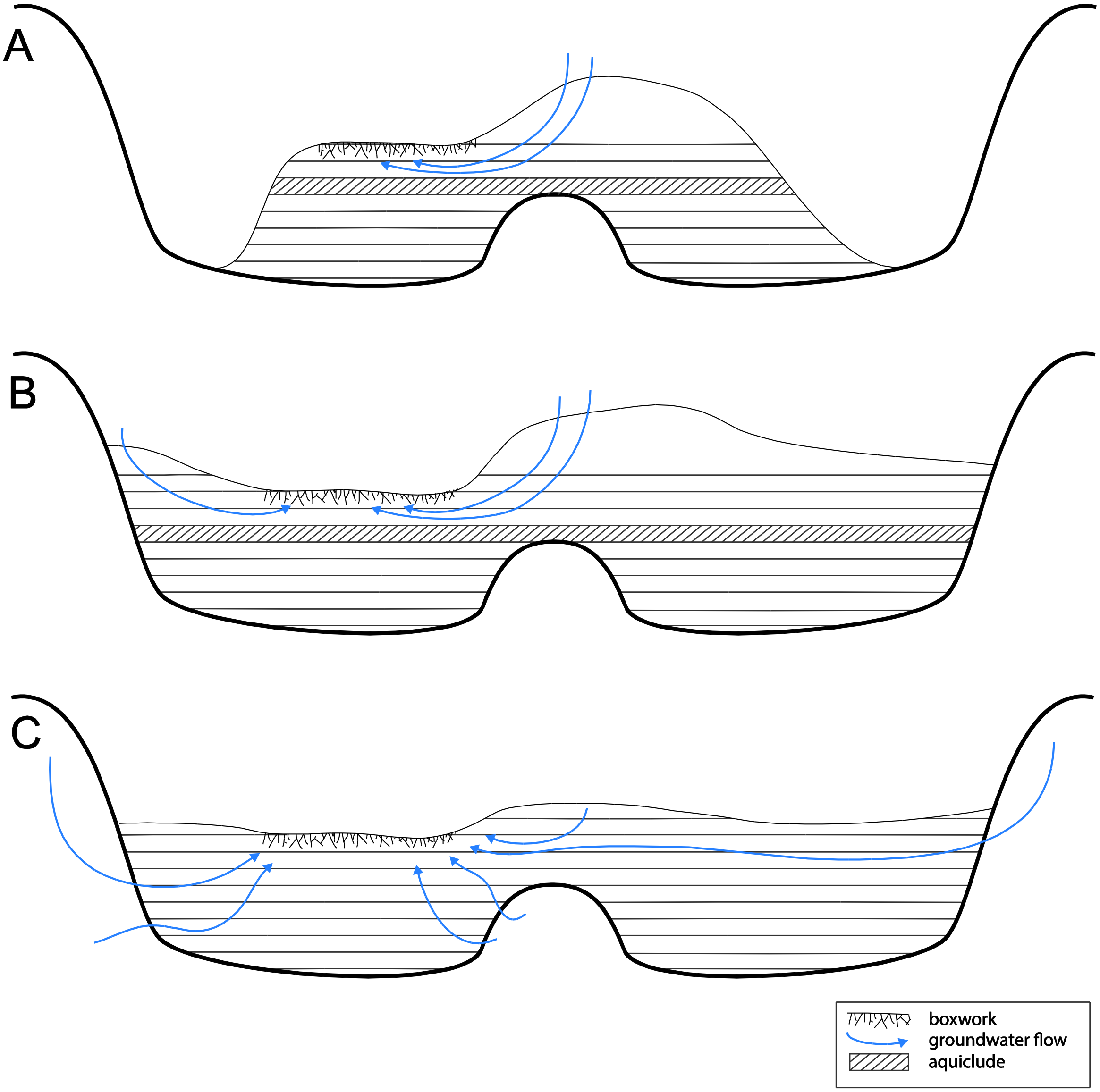

Figure 2.6 Schematic of Mount Sharp Formation Models

Schematic showing possible ancient configurations of Mount Sharp that would allow sufficient groundwater flow to form boxwork structures. Part a shows a scenario where Mount Sharp formed as a central mound with an aquiclude, where groundwater must have originated from precipitation on topographically high parts of the mound, and evaporated in locations with low overburden pressure, forming the boxwork structures. Part b shows a scenario where most of the crater is filled with sediments and the boxwork form in a topographic low because an aquiclude prevents groundwater from sinking in the crater. Part c shows a less conservative scenario where the crater is full of sediments and focuses groundwater from the surrounding region that evaporates to form the boxwork.

ions where physical conditions caused local oversaturation. (A variety of soluble minerals might have been involved in dissolution updip, to precipitation downdip, but such considerations go beyond the scope of the current paper.) This mechanism would have required Mt. Sharp to have a higher elevation than the -3620 m bedding plane to drive the flow. It also likely would have required a perched water table (unless the whole mountain was saturated), underlain by an aquiclude, to prevent infiltration and loss of the fluid at sites far removed from the recharge area. It is conceivable that in the Mt. Sharp stratigraphy there exist lithologies heterogeneous enough to provide contrasts in hydraulic conductivity. This scenario allows for the possibility, but does not require, that Gale Crater was mostly filled with sediment (Figure 2.6b); as long as the aquifer including the boxwork has sufficient topography and area to serve as a recharge area for the groundwater flow, the sediment need not have filled the entire crater (Figure 2.6a).

A less conservative but viable scenario would invoke filling of Gale Crater with sediments up to the level of the -3620 m bedding plane (Figure 2.6c) [*Malin and Edgett*, 2000]. These sediments could have lithified and fractured based on sediment water flux or thermal expansion-contraction. Subsequent burial due to continued sediment accumulation could have resulted in circulation of mineral-saturated groundwaters in the fracture network, with later precipitation of minerals in the fractures. Eventually, these strata were exhumed, creating Mt. Sharp and exposing the bedding plane on which the boxwork fabric is developed.

2.5 Conclusions

Detailed mapping of the filled fracture network on Mount Sharp indicates that this sedimentary layer most likely represents large-scale boxwork fabrics. The original sedimentary rock was lithified, likely by early cementing fluids during shallow burial. Subsequently this layered unit was exposed at the surface and fractured, and then it was again buried. Circulation of mineral-saturated fluids in the phreatic zone further lithified sediments adjacent to the fractures and also at least partially filled the fractures. This sequence of events requires circulation of mineral-saturated groundwater, supporting mound-formation scenarios in which groundwater could migrate from an undersaturated recharge area to precipitate within the boxwork level at least a kilometer above the current crater floor.

Volumes of diagenetic cements can be measured from orbital imagery and, based on these measurements and an assumed chemistry, the minimum volume of water required to form the cements measured was calculated to be about 0.4 km^3. These deposits provide evidence for extensive and relatively rapid cement formation, which could be beneficial to the preservation of organic compounds, 1050 m above the current floor of Gale Crater.

The Mars Science Laboratory *Curiosity* rover is capable of driving to the boxwork layer [*Grotzinger et al.*, 2012] from its landing site on the floor of Gale Crater and investigating the chemical composition and textures of these deposits from the surface. This site is a possible target for investigation by *Curiosity* as a location where a series of post-depositional water-based processes are interpreted that left extensive exposed diagenetic cements, which are indicative of possibly favorable conditions for preservation of organic compounds.

Acknowledgements

This work was supported by the Caltech GPS fellowship fund and a NASA Astrobiology Institute grant #NNA13AA90A to JPG. We thank K. Stack for help determining the DTM precision, N. Tosca for providing brine evaporation results, and Mars Science Laboratory science team colleagues for helpful discussions. Helpful reviews by M. Ramy El-Maarry and R. Irwin improved this manuscript.

Chapter 3

Subaqueous Shrinkage Cracks in the Sheepbed Mudstone: Implications for Early Fluid Diagenesis, Gale Crater, Mars

Kirsten L. Siebach, John P. Grotzinger, Linda C. Kah, Kathryn M. Stack, Michael Malin, Richard Léveillé, and Dawn Y. Sumner

Chapter 3 is published in:
Siebach, K. L., J. P. Grotzinger, L. C. Kah, K. M. Stack, M. Malin, R. Leveille, and D. Y. Sumner. (2014) Subaqueous Shrinkage Cracks in the Sheepbed Mudstone: Implications for Early Fluid Diagenesis, Gale Crater, Mars. *J. Geophys. Res.*, online 17 Jul 2014, doi: 10.1002/2014JE004623.

Key Points

- Raised ridges are early diagenetic cement-filled cracks in Sheepbed mudstone
- Cracks are subaqueous shrinkage cracks likely formed by subsurface gas
- Isopachous cement fills indicate series of pore fluid chemistries

Abstract

The Sheepbed mudstone, Yellowknife Bay formation, Gale crater, represents an ancient lakebed now exhumed and exposed on the Martian surface. The mudstone has four diagenetic textures, including a suite of early diagenetic nodules, hollow nodules, and raised ridges, and later diagenetic light-toned veins that cross-cut those features. In this study, we describe the distribution and characteristics of the raised ridges, a network of short spindle-shaped cracks that cross-cut bedding, do not form polygonal networks, and contain two to four layers of isopachous, erosion-resistant cement. The cracks have a clustered distribution within the Sheepbed member and transition laterally into concentrations of nodules and hollow nodules, suggesting that these features formed penecontemporaneously. Because of the erosion-resistant nature of the crack fills, their three-dimensional structure can be observed. Cracks that transition from sub-vertical to sub-horizontal orientations suggest that the cracks formed within the sediment rather than at the surface. This observation and comparison to terrestrial analogs indicate that these are synaeresis cracks - cracks that formed

subaqueously. Synaeresis cracks form by salinity changes that cause sediment contraction, mechanical shaking of sediment, or gas production within the sediment. Examination of diagenetic features within the Sheepbed mudstone favors a gas production mechanism, which has been shown to create a variety of diagenetic morphologies comparable to the raised ridges and hollow nodules. The crack morphology and the isopachous, layered cement fill show that the cracks were filled in the phreatic zone and that the Sheepbed mudstone remained fluid-saturated after deposition and through early burial and lithification.

3.1 Introduction

Whereas Mars was once considered to be a mostly volcanic planet, the last ten years of exploration have shown that there are a significant number of sedimentary deposits on Mars, and that these rocks record a complex history of water-rock interaction [*McLennan and Grotzinger*, 2008a; *Grotzinger and Milliken*, 2012]. Orbitally-based observations have shown that these rocks form in a range of depositional environments and show a wide variety of spectral signatures [e.g. *Ehlmann et al.*, 2008a; *McLennan*, 2012]. More detailed investigations into sedimentary clast origins, depositional textures, rock lithification, and later rock modifications must be completed at the rover-scale. Diagenesis, in particular, includes all processes that occur after initial sediment deposition and prior to weathering and erosion of an exhumed rock, including the lithification of sediments into rock. Investigation into the diagenetic stages that sediments have undergone helps constrain the duration, continuity, and chemistry of different stages of water-rock interaction. Diagenesis of sediments usually encompasses loss of porosity due to grain reorganization, compaction, and cementation of the rock, and may also include authigenic mineral precipitation, void formation, and sediment deformation [*Worden and Burley*, 2003]. Later diagenetic affects may also include events related to creation of new pore networks, often associated with fracturing and subsequent fluid migration events [*Long et al.*, 1996]. Detailed studies of mineralogy, chemical variability, and textural features can aid in reconstruction of these diagenetic events. Ultimately, understanding diagenetic histories can provide critical constraints on the reconstruction of ancient depositional environments, and the chemical evolution of sedimentary pore fluids.

Effects of sediment diagenesis have been observed on Mars at both rover [*Clark et al.*, 2005; *McLennan et al.*, 2005] and orbiter scales [*Okubo and McEwen*, 2007; *Ehlmann et al.*, 2011; *Siebach and Grotzinger*, 2014a] and have been attributed to the circulation of liquid water through pore networks. In some cases, these observations provide plausible constraints on the volume of water required to form diagenetic signals (e.g. [*McLennan et al.*, 2005; *Siebach and Grotzinger*, 2014a]). At present, most of the diagenetic processes observed by landed missions on Mars, like the sulfate cementation at Meridiani Planum, have pointed to acidic, highly saline groundwaters with low water activity [*Grotzinger et al.*, 2005; *McLennan et al.*, 2005; *Knoll and Grotzinger*, 2006; *Tosca et al.*, 2008], however these compositions may be inherently biased due to the small number of landed missions. More recent findings from the Mars Exploration Rover and Mars Science Laboratory (MSL) missions have shown that more neutral-pH environments, with lower salinity and elevated water activity, were also present on early Mars [*Arvidson et al.*, 2014; *McLennan et al.*, 2014; *Vaniman et al.*, 2014], and that these were potentially habitable environments that could have been suitable for chemolithoautotrophic microbes [*Grotzinger et al.*, 2014].

Since landing in August 2012, the *Curiosity* rover has identified multiple types of sedimentary rock, ranging from conglomerate [*Williams et al.*, 2013] to sandstone and fine-grained mudstone, each of which provide evidence for diagenesis [*Grotzinger et al.*, 2014]. The Sheepbed mudstone, interpreted to have been deposited in an ancient freshwater lake, has undergone extensive study with the full range of analytical instruments on the *Curiosity* rover [*Grotzinger et al.*, 2014]. The Sheepbed mudstone is uniformly fine-grained (<63 μm grain sizes), composed of >15% authigenic clay minerals [*McLennan et al.*, 2014; *Vaniman et al.*, 2014], and contains at least four distinct diagenetic textures: nodules (spheroidal protrusions with no discernable internal structure), hollow nodules (spheroidal protrusions showing a central void), raised ridges, and a later generation of gypsiferous, mineralized veins [*Grotzinger et al.*, 2014; *Nachon et al.*, 2014; *Stack et al.*, 2014]. Collectively, these features record long-term exposure to water, and reveal a once-habitable environment in Yellowknife Bay, Mars [*Grotzinger et al.*, 2014]. Here, we investigate the importance of the raised ridge features and use their characteristics to show that the Sheepbed mudstone was most likely deposited subaqueously and had fluid-saturated pore spaces throughout early lithification and cementation of the mudstone.

3.2 Geologic Context

After landing at Bradbury Rise (4.589°N, 137.441°E), Gale crater, Mars, the *Curiosity* rover traversed 445 meters west to the Glenelg region [*Parker et al.*, 2013; *Grotzinger et al.*, 2014]. This region represents the conjunction of three units, defined in orbital images based on geomorphic and thermal inertia attributes, which are located at the distal end of an alluvial fan system [*Grotzinger et al.*, 2014]. One of the units that *Curiosity* investigated in detail was the bright, fractured (BF) unit, characterized by relatively high thermal inertia, exposed light-toned bedrock, and ubiquitous decimeter-scale fractures. An approximately five meter-thick exposure of stratigraphic section of the BF unit occurs at Glenelg and has been described as the Yellowknife Bay formation [*Grotzinger et al.*, 2014]. In ascending order, the latter is subdivided into the Sheepbed, Gillespie Lake, and Glenelg members (Figure 3.1). The uppermost Glenelg member consists of fine- to coarse-grained, locally cross-stratified, basaltic sandstone that is interpreted to reflect fluvial or eolian deposition [*Grotzinger et al.*, 2014]. The Gillespie Lake member, also interpreted as a fluvial deposit, consists of a medium-grained sandstone of basaltic composition. Underlying these two relatively coarse-grained deposits rests the Sheepbed member, a mudstone, also of basaltic composition, that is interpreted to have been deposited in a lacustrine setting [*Grotzinger et al.*, 2014]. The contact of the Sheepbed member with the overlying Gillespie Lake member is sharp, and traceable in orbital imagery.

The stratigraphically lowest unit in the Glenelg region, the Sheepbed member, is exposed in the floor of Yellowknife Bay. Based on *Curiosity*'s observations, it extends across at least the ~60 m traversed within Yellowknife Bay. Given that it can be traced from orbit, and likely closely coincides with the BF unit, the Sheepbed member is inferred to extend laterally at least several hundred more meters to the east and north, and is possibly laterally continuous for hundreds of meters or kilometers beneath the overlying units of the Yellowknife Bay formation [*Grotzinger et al.*, 2014]. The Sheepbed member is the best-characterized member of the Yellowknife Bay formation because two drilled samples, John

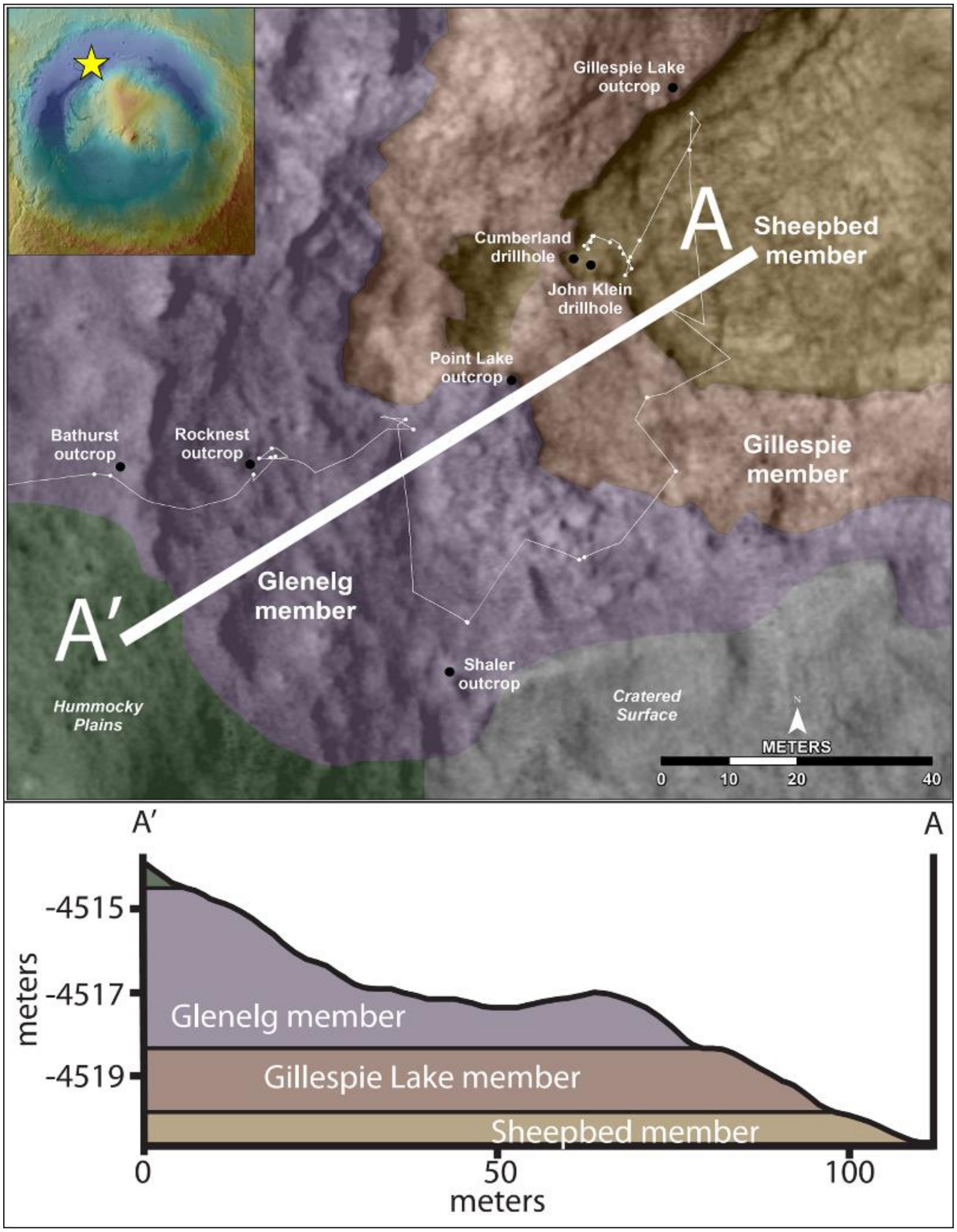

Figure 3.1 Geologic Map of Yellowknife Bay
After *Grotzinger et al.* [2014]. Upper left inset shows Gale crater, 155 km across, with star at Yellowknife Bay location. Lower portion shows members of the Yellowknife Bay formation projected into a HiRISE-extracted elevation profile.

Klein and Cumberland, were acquired from this member and analyzed by *Curiosity's* full analytical instrument suite, including a mass spectrometer and X-Ray Diffraction (XRD) instrument [*Ming et al.*, 2014; *Vaniman et al.*, 2014]. In addition, a suite of Alpha Particle X-Ray Spectrometer (APXS) measurements were collected within the unit [*Grotzinger et al.*, 2014; *McLennan et al.*, 2014] and numerous ChemCam laser-induced breakdown spectroscopy analyses were obtained to help characterize the site [*Léveillé et al.*, 2014; *Nachon et al.*, 2014]. *Curiosity's* investigation demonstrated that the Sheepbed member is uniformly fine-grained, with a near-typical basalt composition, and contains nearly 20% saponitic smectite clay minerals [*Grotzinger et al.*, 2014; *McLennan et al.*, 2014; *Vaniman et al.*, 2014]. The smectite clay, identified by the XRD analysis, was inferred to be authigenic based on the distributed APXS measurements, which showed that the rock chemically matches slightly-alkaline average Martian crustal basalt in all of the samples, suggesting isochemical weathering [*McLennan et al.*, 2014]. Mudstones are generally deposited in low-energy, standing water environments, and the Sheepbed unit, in particular, has been interpreted to have been deposited in a lake that formed at the distal limit of an alluvial fan [*Grotzinger et al.*, 2014].

Diagenetic textures representing at least two distinct post-depositional fluid environments are present in the Sheepbed mudstone. These include nodules, hollow nodules, raised ridges, and light-toned, cross-cutting, calcium sulfate-rich light-toned veins (Figure 3.2) [*Grotzinger et al.*, 2014]. The nodules and hollow nodules are mm-scale resistant spherical protrusions (sometimes with a less-resistant or hollow center) that are densely clustered in some locations [*Stack et al.*, 2014] and pass laterally into concentrations of raised ridges. The light-toned veins weather flush with the surrounding rock and cross-cut the raised ridges, nodules, and hollow nodules (Figure 3.2).

3.3 Methods

Raised ridges—mineralized cracks, only a few mm in width, which are distributed within the Sheepbed member—were mapped over 27 m^2 of the exposed surface of the Sheepbed unit using ArcGIS software and images available through the NASA Planetary Data System. Context for this mapping was derived from High Resolution Imaging Science

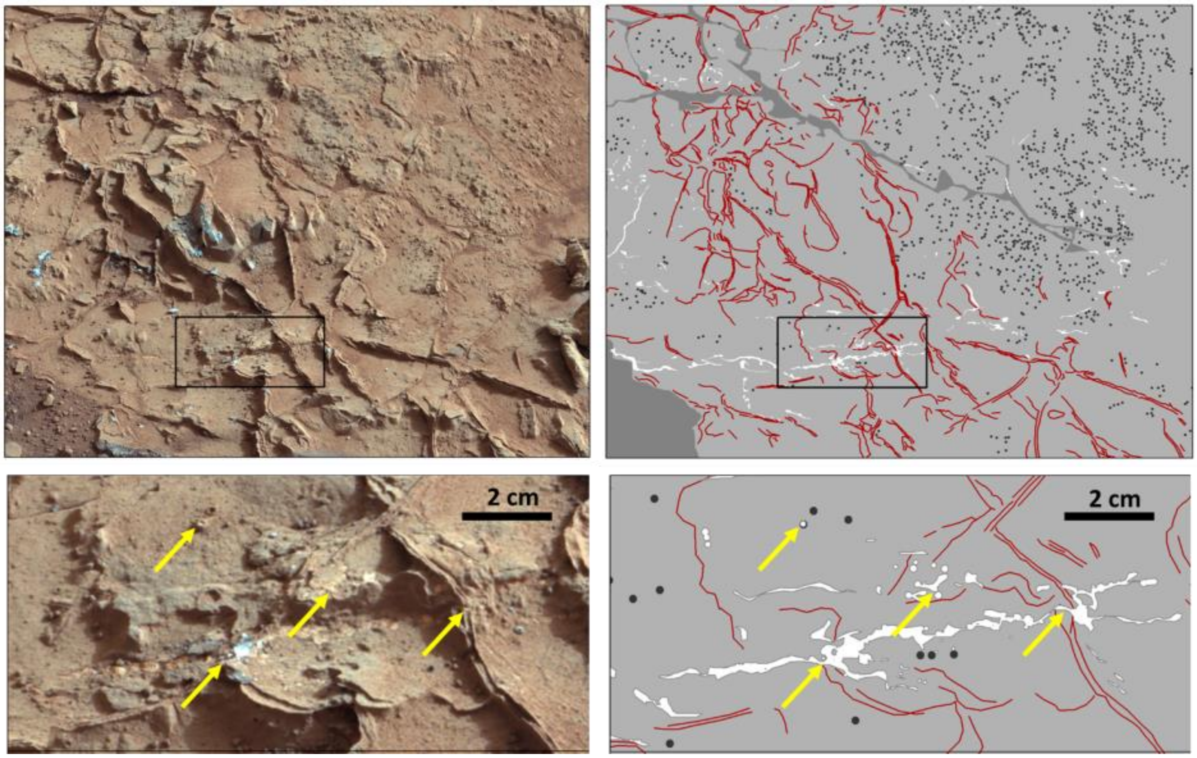

Figure 3.2 Mastcam Image and Interpretation of Raised Ridges
Portions of Mastcam M-100 mosaic (mcam00885, sol 164), with accompanying sketches, showing relationships between diagenetic textures in the Sheepbed unit. Inset box is approximately 13 cm x 6 cm; 2 cm scale bar in inset. Red lines are erosion-resistant cements that compose the raised ridges, dark grey circles are nodules and hollow nodules, white fill shows light-toned veins visible at the surface (many are dust-covered), and dark grey depicts dust covered regions of the mudstone. Yellow arrows in inset highlight cross-cutting relationship showing that the light-toned veins are a later texture that cut through the raised ridges and hollow nodules, sometimes even filling previously-hollow nodules.

Experiment (HiRISE) images (25 cm/pixel) [*McEwen et al.*, 2007a] and orthorectified MSL Navigation Camera (Navcam) imagery [*Maki et al.*, 2012], which have been localized along the rover's traverse by the MSL science team localization scientists based on a controlled photomosaic of sequentially higher resolution data sets tied to the Mars Orbital Laser Altimetry global base map [*Parker et al.*, 2013]. HiRISE imagery was used as a basemap for stratigraphic analysis, and rover-based Navcam imagery was used to create contours and localize ChemCam and drill targets. Neither of these image sets, however, provide adequate resolution to map the raised ridge features.

The *Curiosity* Mast Camera (Mastcam) imagery proved to be the best available imagery to map the sub-mm-scale raised ridge features over a large spatial area (~27 m^2). The Mastcam consists of two mast-mounted cameras that sit approximately 2.1 m above the surface. The right Mastcam (M-100) has a 100-mm focal length, f/10 lens, with a 6.3° x 5.1° field of view (FOV), and the left Mastcam (M-34) has a 34-mm focal length, f/8 lens, with an 18.4° x 15° FOV. The two cameras are separated by a 24.5 cm stereo baseline [*Malin et al.*, 2010; *Bell et al.*, 2013]. Image mosaics taken with the M-100 camera are preferable for mapping the raised ridge features because of their inherent higher image resolution; even for surfaces 5 m away from the rover, the M-100 camera provides a resolution of 0.37 mm/pixel, whereas the M-34 has a resolution of 1.1 mm/pixel. However, because the images are not taken vertically, but at a variable angle, raw M-100 imagery is necessarily distorted relative to the actual topography of the raised ridges. Thus, where available, stereo imagery was used to create orthorectified Mastcam mosaics using the Ames stereo pipeline [*Moratto et al.*, 2010], which was adapted by Malin Space Science Systems to work with the different resolution of the two Mastcams (see Appendix A). Orthorectified Mastcam mosaics were able to be more accurately correlated to the Navcam-based map, and permitted raised ridges to be traced over the key areas of the Sheepbed member, with reference to the vertically projected M-100 mosaics when needed for higher resolution (or to correct distortions introduced in the image orthorectification process).

In addition to the large-scale mapping, a Mastcam mosaic, mcam00885, taken on sol 164, was selected for fine-detail mapping of the individual cement layers in the raised ridges and the relationship of the raised ridges to the other diagenetic features in the

Sheepbed member. This mapping was also accomplished in ArcGIS, but in this case, because it was critical that the features not be distorted, the rover-perspective white-balanced mosaic was used and the average scene pixel scale (0.206 μm/pixel) was used for measurements of the length and width of 300 individual ridges and cements.

3.4 Observations

Raised ridges within the Sheepbed mudstone occur as cracks in the mudstone filled with multiple layers of cement. The outermost layer of cement fill is resistant to erosion, resulting in curvilinear ridges that outline the original crack shape, stand above the host rock, and give these features the name "raised ridges." Interior cement layers are usually less resistant, although in some cracks multiple layers of resistant cements are visible (e.g. Figure 3.2). The redundancy in the term "raised ridges" is meant to emphasize the height of the ridges relative to their width.

Raised ridges were mapped comprehensively in the vicinity of the John Klein and Cumberland drill sites where near-rover orthorectified overhead imagery was available (Figure 3.3). Bedding is rarely visible in this local area, but it is assumed to be near-horizontal and to follow contour lines based on an observed near-horizontal conformable contact with the Gillespie Lake member [*Grotzinger et al.*, 2014]. The most obvious feature of the raised ridges at the meter scale is their clustered distribution (Figure 3.3). Laterally, a few concentrated clusters of raised ridges are visible, each region measuring tens of cm in diameter. Individual ridge networks do not continue laterally within the same contour interval (i.e. within the same stratigraphic horizon), but transition into either relatively featureless mudstone or areas of concentrated nodules and hollow nodules (e.g. Figure 3.2; [*Stack et al.*, 2014]). Additionally, both individual ridges and ridge networks cross-cut topographic contours (Figure 3.3). Some raised ridges are not localized within the larger clusters, but scattered both laterally and vertically through the mudstone. There is no consistent preferred crack orientation (Figure 3.3). At least two ridge clusters (one in Figure 3.3 and another called the "Rowatt" cluster, Figure 3.9) occur immediately beneath the Sheepbed-Gillespie Lake contact; and in one location a single raised ridge appears to cross-cut the Sheepbed-Gillespie Lake contact.

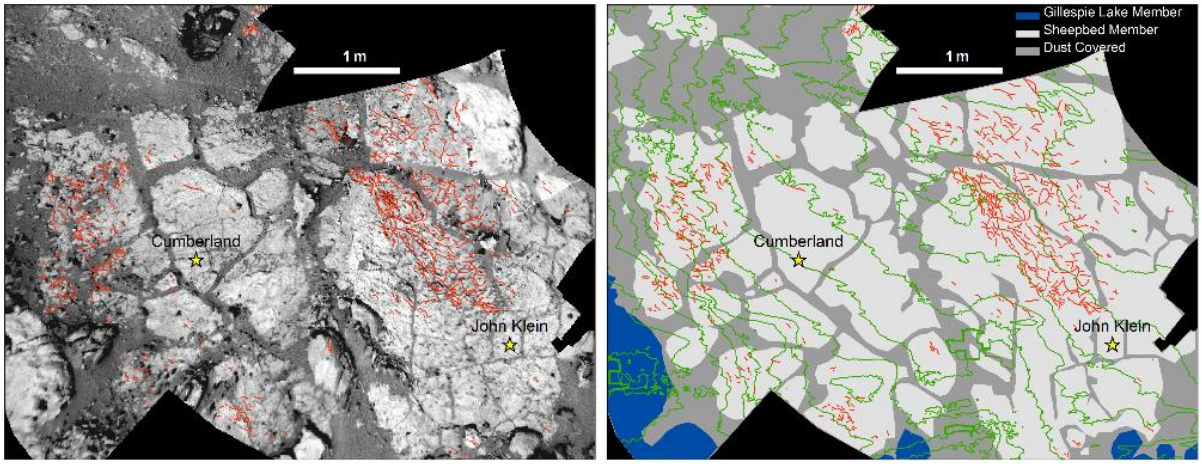

Figure 3.3 Overhead Map Showing Raised Ridge Distribution
Vertically-projected map, showing the distribution of raised ridges (red lines) throughout the mapped area. On the left side, the ridges are shown on a mosaic of rover navigation camera images. On the right side, the same mosaic is mapped to show Sheepbed member exposures in light gray, Gillespie Lake member in blue, and dust-covered regions in dark grey. Five cm contours based on the Navcam mosaic from sol 159 are shown in green. The John Klein and Cumberland drill sites are identified with yellow stars. Ridges show a clustered distribution both horizontally (within contours) and vertically (across contours) and therefore are not confined by bedding planes.

Detailed mapping of lengths, widths, and shapes of raised ridges within the dense cluster of ridges near the John Klein drill site (Figure 3.4) shows the characteristics of the crack morphologies and details of fill patterns (e.g. Figure 3.5). Erosionally resistant infill permits clear identification of the original crack morphology as represented by current ridge morphology. The raised ridges average 6.8 cm in length, but can reach up to 50 cm, and widths range between 1.1 mm to 5.6 mm, averaging 2.6 mm. Terminations of the ridges, where visible, are tapered to a spindle-shaped point. Raised ridges do not form discrete polygons; where they do intersect, it is at an arbitrary variety of angles (Figure 3.5d-f). The two-dimensional morphology of ridge exposures range from straight to sinuous (e.g. Figure 3.5). In some cases, adjacent ridges turn toward each other near the termini (e.g. Figure 3.5e).

Projection of raised ridges above the mudstone surface resulting from resistant crack-filling cement enables viewing of original crack orientation in three dimensions. Ridges range from vertical to subhorizontal in dip, and are curviplanar; several ridges are observed transitioning from sub-vertical dip angles to sub-horizontal dip angles that reflect crack intersections at oblique angles (Figures 3.5f-h). Additionally, a variety of erosionally resistant, gently sloped features, marked by parallel bands morphologically similar to ridge cement, are visible in the mudstone up to a couple of cm above the surface and are interpreted as exhumed sub-horizontal crack-fills (e.g. Figure 3.5h, i).

As noted, these raised ridges reflect initial cracks that are currently filled with two to four layers of erosionally-resistant infill. The crystal size of this cement infill is not visible, even at Mars Hand Lens Imager scales of 15-20 micrometers per pixel. The outermost cement, which represents the boundary between the sediment and the initial crack wall, is approximately 1 mm thick (measured normal to the crack surface) and has consistent thickness on all walls within individual raised ridges regardless of local curvature (i.e. it is an isopachous cement coating [*Pettijohn and Potter*, 1964]). The thickness of the cement varies in different ridge sets, from 0.6 mm to 1.2 mm (averaging 1.0 mm), but does not vary within individual ridges; within a given crack, the precipitation was isopachous. When two ridges intersect, this resistant cement continuously lines the

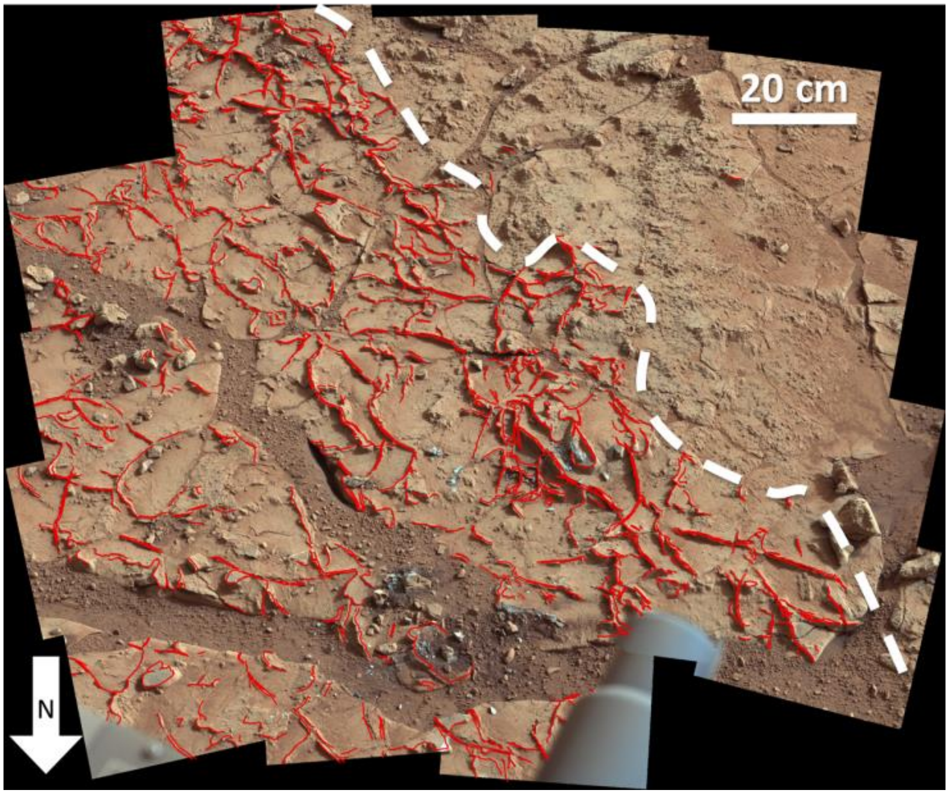

Figure 3.4 Detailed Map of Individual Raised Ridges
Detailed map of individual raised ridges (red) traced on Mastcam mosaic mcam00885 from sol 164. White dashed line highlights lateral shift in texture from raised ridges (left side) to nodules plus hollow nodules (right side).

(Figure on following page)

Figure 3.5 Panel Showing Raised Ridge Morphologies
Insets showing details of raised ridge morphology with frames from white-balanced rover-perspective mosaic mcam00885, sol 164. Scale bars for images A, D, and G are 5 cm, scale bars for insets are 1 cm. Exposed grey rock surfaces were broken by the rover wheel. Yellow arrows highlight spindle-shaped cracks with tapered termini, white arrows highlight curvilinear features for comparison to Figure 3.6. Images A-C highlight the isopachous cement lining that creates parallel-sided ridges outlining the cracks, and sometimes, as in image c, the multiple cement layers within the cracks. Image D shows that the cracks are short and taper rapidly into a spindle shape. Inset E focuses on two cracks that appear to bend towards each other, indicating that the cracks all formed in one stage and traced planes of weakness in the rock. Image F highlights the non-polygonal nature of the cracks and resulting variety of crack intersection angles. Image G shows multiple cracks that transition from near-vertical to sub-horizontal spatial orientations. Inset H highlights an intersection between a near-vertical crack and a sub-horizontal crack. Image I shows a ramped feature that appears to be a sub-horizontal raised ridge preserved because of the resistant cement.

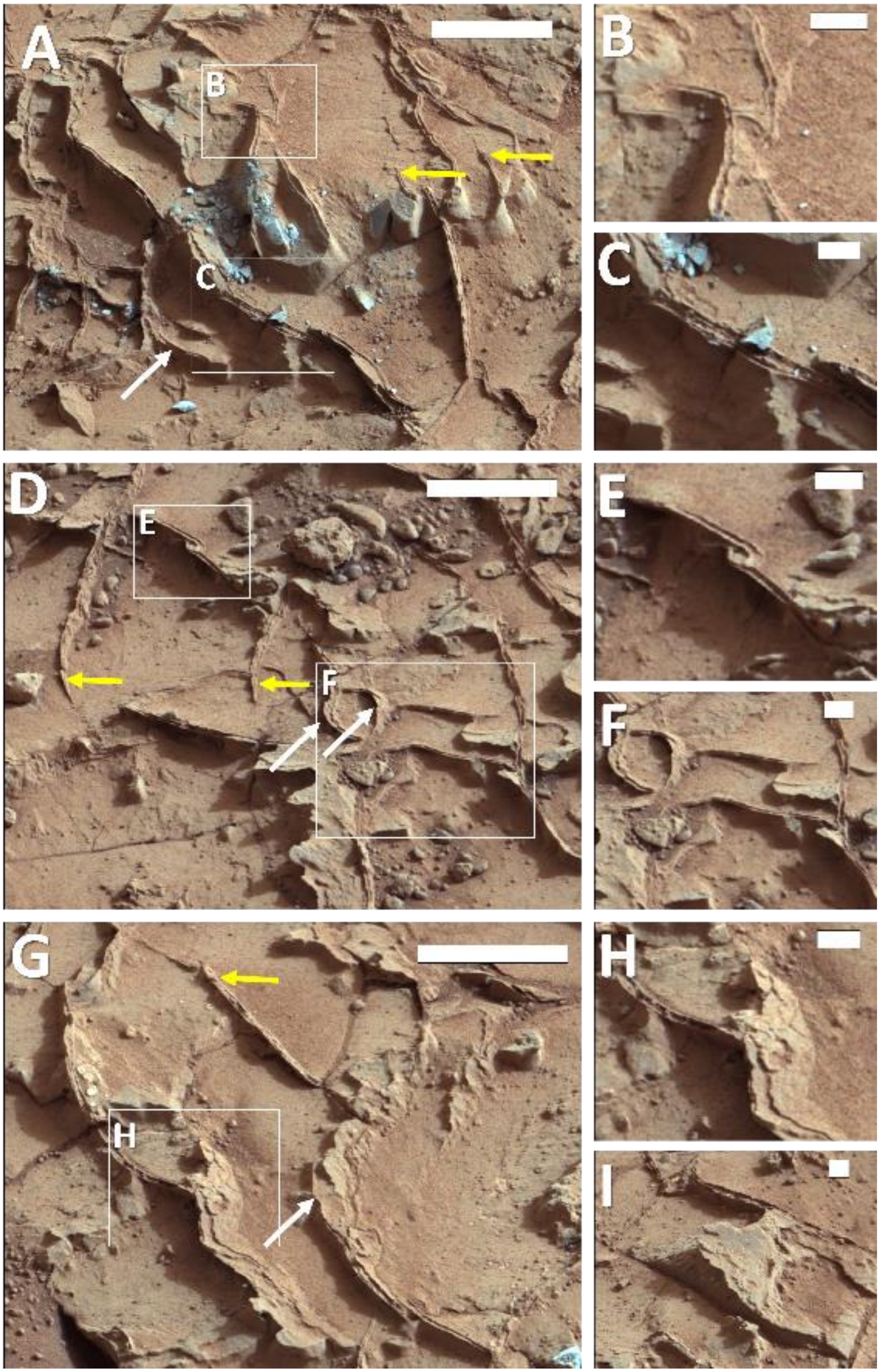
A
B
C
B
C
D
E
F
E
F
G
H
H
I

edges of the intersecting features, regardless of the orientation of the initial cracks (e.g. Figure 3.5b). No evidence is seen for detrital sediment infilling of the cracks.

The APXS, ChemCam, and CheMin instruments onboard *Curiosity* were used to explore the composition of the resistant cement fill relative to the Sheepbed mudstone [*Grotzinger et al.*, 2014; *Léveillé et al.*, 2014; *McLennan et al.*, 2014; *Vaniman et al.*, 2014]. The ChemCam instrument (laser-induced-breakdown spectroscopy) has a spot size of about 0.5 mm, and therefore was able to target laser shots along the outermost cement layer of the McGrath raised ridge target. Those analyses indicated that the outermost cement layer of the McGrath raised ridge is enriched in Mg, somewhat enriched in Li, and depleted in Al relative to the rest of the mudstone [*Léveillé et al.*, 2014]. The APXS has a 2.25 cm^2 spot area and also analyzed the sub-horizontal McGrath target, finding that the ridge was enriched in Mg and Fe, and that these were both correlated to enriched Cl relative to the Sheepbed mudstone [*McLennan et al.*, 2014]. Additionally, the CheMin x-ray diffraction instrument analyzed two samples within the Sheepbed unit, neither of which contained a visible component representing the raised ridges. The Cumberland target, however, contained a notable contribution from nodules and hollow nodules, which appears to be reflected in a several percent increase in akaganeite (an iron oxide-hydroxide/chloride mineral) and magnetite relative to the John Klein drill hole, only about 2 m away [*McLennan et al.*, 2014; *Stack et al.*, 2014; *Vaniman et al.*, 2014]. Based on these observations, it has been suggested that the resistant cement may be composed of akaganeite, magnetite, and/or some authigenic smectitic clay component, such as griffithite [*Grotzinger et al.*, 2014; *Léveillé et al.*, 2014; *McLennan et al.*, 2014; *Vaniman et al.*, 2014].

3.5 Discussion

Any proposed formation model must account for these observations: (1) Crack networks—as defined by their erosion-resistant infill—penetrate the mudstone, are spatially restricted, and transition laterally into high concentrations of nodules and hollow nodules or featureless mudstone; (2) individual cracks are curviplanar in three dimensions and cross-cut stratigraphic contours; and (3) after opening, the cracks are filled with multiple generations of isopachous cement.

3.5.1 Origin of Raised Ridges

3.5.1.1 Formation Environment

Raised ridges within the Sheepbed mudstone appear to have originated as early diagenetic cracks within the mudstone. Their present morphology, as elevated ridges, is based on preferential erosion of the surrounding sediment relative to the crack fill (e.g. Figure 3.5b). The observation that cement continuously traces crack edges even when two cracks intersect demonstrates that the cracks were open before the cement layer began to precipitate within open void space (Figure 3.5b). Apparent spatial clustering of both nodular features [*Stack et al.*, 2014] and raised ridge networks suggests that either the distribution of one feature controlled the distribution of the other (for instance, via a change in mudstone rheology caused by the formation of one of the features), or that these are penecontemporaneous structures [e.g. *Calver and Baillie*, 1990; *Duck*, 1995]. In either case, cross-cutting relationships indicate that both nodular features and raised ridges had formed and mineralized prior to formation of late-stage, sulfate-mineralized fractures (the sulfate-mineralized fractures clearly cut through raised ridges and through nodules, shown in Figure 3.2) [*Grotzinger et al.*, 2014; *Nachon et al.*, 2014]. If raised ridges and nodules are penecontemporaneous structures, we must examine the possibility that nodules and raised ridges share a common diagenetic environment.

In addition to their distribution, a critical observation that may constrain the origin of the raised ridge features is that the cracks that comprise raised ridge networks are short, curviplanar, and have narrow to spindle-shaped terminations in three dimensions. This style of short, spindle-ended cracking occurs prior to complete lithification of the sediment [*Burst*, 1965; *Calver and Baillie*, 1990]. Additionally, cracks cross stratigraphic contours and intersect at arbitrary angles that do not form polygons (Figure 3.5). Polygonal cracking typically develops in response to internal, contractional stresses within the sediment (e.g. dewatering [*Shorlin et al.*, 2000] or cooling [*Peck and Minakami*, 1968]) wherein the polygonal morphology acts to minimize stresses within the material. Because nonorthogonal, irregular crack intersections do not minimize stress, irregular crack orientations are typically interpreted to have formed quickly, exploiting inhomogeneities within the sediment [*Lachenbruch*, 1962; *Sletten et al.*, 2003]. Furthermore, the extension of irregular intersections in three dimensions, the curviplanar morphology of cracks which result in transitions from sub-vertical to sub-horizontal orientations, and the presence of cracks that cross-cut stratigraphic contours (i.e. cracks do not appear to either terminate or originate at common bedding planes) all indicate crack formation in the subsurface [*O'Connor*, 1972; *Horodyski*, 1976; *Plummer and Gostin*, 1981], where overburden pressures are sufficient to equalize vertical and horizontal stresses.

3.5.1.2 Comparison with Terrestrial Early Diagenetic Cracks

Combined, these lines of evidence suggest that raised ridges originated as sub-planar cracks, or voids, contained fully within the sediment. This model is very different from the most familiar mode of early diagenetic fracturing on Earth—the formation of desiccation cracks. Desiccation cracks form at the sediment-air interface because water loss leads to contraction of the sediment [*Lachenbruch*, 1962; *Plummer and Gostin*, 1981]. Such desiccation features originate at a discrete sedimentary surface (a future bedding plane), and extend vertically into the subsurface, forming a wedge shape that narrows and ultimately terminates at some depth (often at variable depths) within the sediment [*Weinberger*, 1999]. Although early stages of crack formation may be recognized by the presence of short, isolated cracks (e.g. “incomplete mudcracks”, [*Plummer and Gostin*, 1981]), these initial cracks typically expand and intersect in a polygonal pattern to minimize contractional stresses within the surface layers [*Sletten et al.*, 2003]. Regardless of the extent to which this ultimate, polygonal morphology is reached, desiccation cracks that enter the rock record are invariably filled by detrital sediment from the sediments that directly overlie the desiccated strata [*Pettijohn and Potter*, 1964]. Indeed, desiccation cracks in the rock record are recognized by the sediments that fill them. This is in sharp contrast to the Sheepbed cracks, which were neither filled with fine-grained Sheepbed sediment nor relatively coarse-grained sands from the Gillespie Lake sediment, but instead show multiple isopachous cement layers. Furthermore, the Sheepbed cracks are curviplanar in three dimensions and do not form polygons or terminate along bedding planes.

Although less common, subaqueous cracking of sediments is not unknown in terrestrial environments (e.g. Figure 3.6). Subaqueous crack formation was first recognized by White [1961], who suggested that subaqueous cracks could result from *in situ* salinity changes in clay colloids leading to fabric collapse and then contraction and tighter packing of the clays. This process generates crack-shaped voids that are filled with the displaced fluids (Figure 3.7a). The term "synaeresis" was applied to these cracks to refer to the contractional stresses within the sediment that resulted during fabric collapse within the clay [*White*, 1961]. The potential for saline fluids to result in such volumetric shrinkage was experimentally confirmed by Burst [*Burst*, 1965], and the resulting features share many commonalities with raised ridges in the Sheepbed mudstone. For instance, synaeresis cracks tend to be short, straight to sinuous, are generally spindle-shaped, with tapering termini [*O'Connor*, 1972; *Plummer and Gostin*, 1981], form in the very shallow subsurface (all predate sediment compaction), and cross-cut bedding planes [*Horodyski*, 1976; *Plummer and Gostin*, 1981]. Additionally, the presence of a significant amount of smectite clays within the Sheepbed mudstone [*McLennan et al.*, 2014; *Vaniman et al.*, 2014] suggest that environmental conditions may have been favorable for saline-fluid-based synaeresis (Figure 3.7a).

More recently, several additional formation processes for synaeresis cracks have been proposed. In one alternative, synaeresis-like features result from tensional stresses imposed upon sediment from an external source [*Cowan and James*, 1992; *Pratt*, 1998b; a; *Bishop et al.*, 2006]. One subcategory of cracks that clearly form by this mechanism, termed "diastasis" cracks [*Cowan and James*, 1992], are sub-planar, sub-vertical, often well-aligned spindle-shaped cracks that form in clay-rich, cohesive layers as these layers are placed under tension from wave-driven motion of overlying and underlying sandy, or less cohesive, layers. Rupture of the cohesive layer permits rapid infilling of diastasis cracks via injection of less cohesive sediment from either above or below the cohesive layer. A critical observation leading to the interpretation of diastasis cracks, however, is

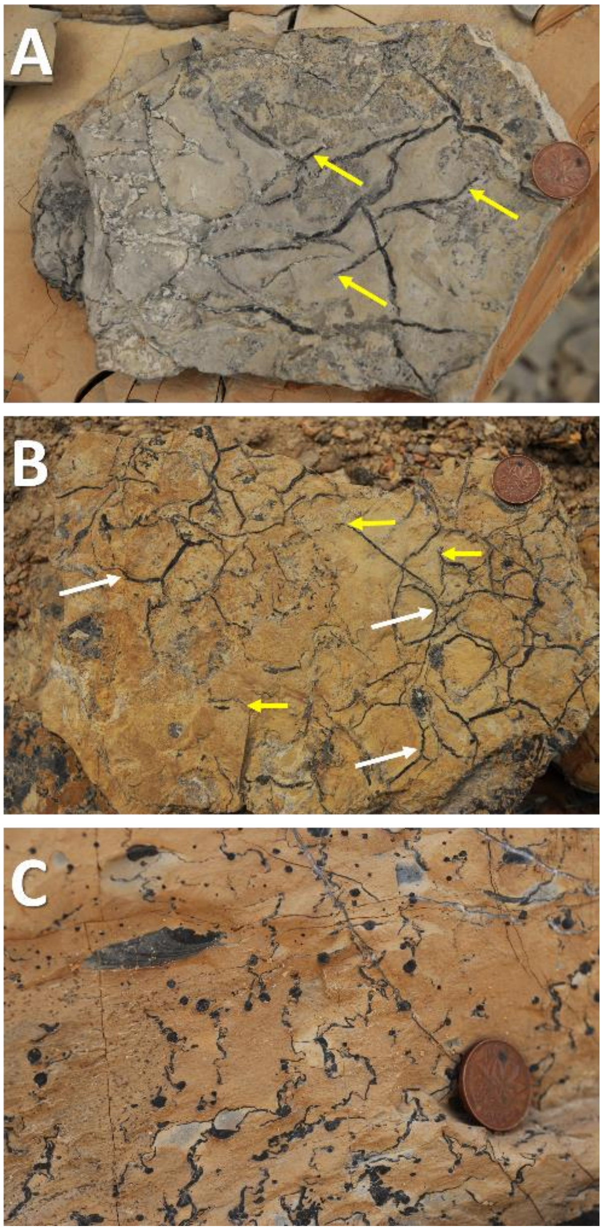

Figure 3.6 Proterozoic Molar Tooth Structure Analogs
Proterozoic molar tooth structures from the Helena formation in the Belt Supergroup, MT, USA. Coin is 19 mm across for scale. Images a and b show preserved bedding planes with short, curvilinear, spindle-shaped cracks. Yellow arrows highlight spindle-shaped cracks with tapered termini, white arrows highlight curvilinear features for comparison to Figure 3.5. These crack morphologies are very comparable to the raised ridge crack morphologies, although the cement is not resistant to erosion in this case. Note curvilinear cracks and irregular clustered distribution in image b. Image c shows a cross-section of molar tooth ribbons and blobs. Note interfingering transition between ribbon and blob facies and horizontal-to-vertical transitions of ribbons.

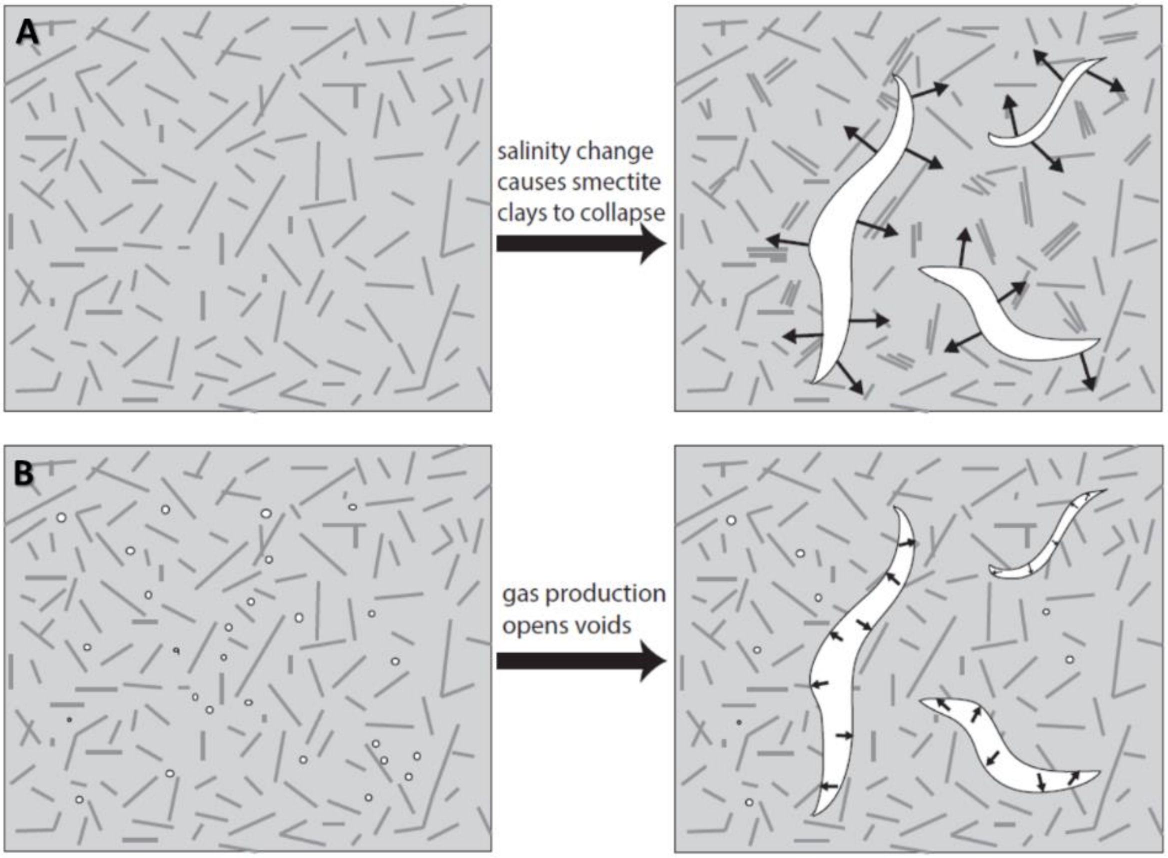

Figure 3.7 Schematic of Synaeresis Crack Formation Mechanisms
Schematic showing possible formation mechanisms for synaeresis crack formation. (A) depicts a change in pore fluid chemistry that causes collapse of smectite clay interlayers, causing volumetric compaction of the sediment, which opens synaeresis cracks. (B) depicts a gas production process such that if the gas becomes trapped, it can create void spaces within the mudstone, which could form both hollow nodules and synaeresis or raised ridge shapes.

the presence of systematic crack orientations resulting from a directed tensional stress field. Raised ridges within the Sheepbed mudstone show no such preferred orientation (see Figure 3.3), suggesting that diastasis is an unlikely mechanism of formation. A similar formation mechanism that does not require layered sediments suggests that these cracks could open due to shaking of the sediment from nearby seismic activity (possibly due to landslides or impacts in this case) even in homogeneous cohesive material [*Pratt*, 1998b; a]. This mechanism would not produce aligned cracks and so cannot be ruled out for the raised ridge features.

In a third scenario, synaeresis-like cracks are inferred to result from the production of gasses within sedimentary pore-fluids, creating localized dilational stresses within the sediment. On Earth, Proterozoic "molar-tooth" structures are typically interpreted to have formed this way [*Smith*, 1968; *Plummer and Gostin*, 1981; *Furniss et al.*, 1998]. Predictable behavior resulting from the production (or exsolution) of gas within pore fluids of the surrounding sediment [*Terzaghi*, 1944; *Mitchener and Torfs*, 1996; *Pollock et al.*, 2006; *Stack et al.*, 2014] creates structures that provide an interesting comparison to the morphology of primary void spaces within the Sheepbed mudstone. The primary parameter in determining the behavior of gasses within unconsolidated substrate is the cohesive strength of the sediment [*Terzaghi*, 1944], which commonly reflects a combination of grain size and composition. Composition is critical because the presence of >15% clay minerals within the sediment has been shown to substantially increase its cohesive strength [*Mitchener and Torfs*, 1996]. Once gasses form bubbles that are larger than inter-particle void space, these bubbles will provide dilational stresses that deform and compact the surrounding sediment. Because gasses will tend to rise and escape, grain-scale inhomogeneities will be exploited and favor the upward movement of gas. In the case of poorly consolidated sediments, upward migration of gas bubbles will often result in dewatering and an increase in the consolidation of sediments. In the case of higher strength sediments (such as cohesive, and clay-rich sediments), gas bubbles will tend to be trapped as consolidation of grains along the bubble margin increases local sediment strength. Under these conditions, crack formation can occur when gas pressures exceed the local sediment yield strength, and cracks will commonly propagate in a range of orientations, from vertical (denoting the favored orientation for gas escape) to horizontal (denoting a common direction of weakness within layered sediment) [*Pollock et al.*, 2006].

Exsolution of gasses within substrate pore space has recently been proposed as a mechanism for the formation of nodules and hollow nodules within the Sheepbed mudstone [*Stack et al.*, 2014]. A mechanism of void formation resulting from release of sediment gasses can plausibly explain both the formation of early diagenetic hollow nodules [*Stack et al.*, 2014] and cracks associated with the raised ridges. Differences in the morphology of gas-induced structures may reflect either differences in the rate of production of gasses within the sediment or spatial differences in the cohesive strength of the sediment [*Pollock et al.*, 2006]. *Stack et al.* [2014] further suggest a combination of these last two mechanisms of crack formation, in which release of pore-fluid gasses may plausibly be related to the propagation of impact-induced seismic waves during deposition of the Yellowknife Bay formation. In this scenario, complex interference patterns could produce zones of greater or lesser seismic pressure, which might affect the extent to which pressure-induced degassing occurs, and thereby control the spatial distribution of nodular features and crack networks. Similarly, slight changes in the cohesive strength of the substrate, resulting from either differential compaction or spatial differences in clay content, may be reflected in the spatial distribution of gas-induced features.

Formation of raised ridges as curviplanar voids in the subsurface formed via gas expansion supports the observations of crack clustering and the cross-cutting of stratigraphic contour intervals. Similarly, such a mechanism supports the varied orientation of observed features, which presumably reflect lithologic zones of weakness and inhomogeneities in the sediment (Figure 3.3). Finally, the observation of multiple clusters of raised ridges directly beneath and, in one case, intersecting the Gillespie Lake member suggest that crack formation must have occurred penecontemporaneously with or soon after deposition of the basal Gillespie Lake sandstone. These observations suggest that crack formation occurred prior to burial-induced dewatering, and provide the possibility that the relatively coarse-grained Gillespie Lake member may have provided critical overburden pressure necessary to increase gas pressures during exsolution of gasses within Sheepbed pore-fluids.

3.5.2 Lithification of Raised Ridges

Regardless of the formation mechanism of sub-planar cracks and voids within the Sheepbed mudstone, it is necessary to discuss their mechanism of preservation. Fine-grained sediment can preserve cracks formed during or shortly after sediment deposition under several distinct conditions. First, there is a possibility that sediment is sufficiently lithified via early cementation so that it can retain otherwise unsupported void space. However, more commonly, the void space fills with sediment or detritus or is propped open by cement that occludes porosity [*Halley and Schmoker*, 1983]. In general, if cracking occurs at the sediment-water (or sediment-air) interface, cracks will typically be filled with sediment from above [*Pettijohn and Potter*, 1964]. Similarly, subaqueous shrinkage cracks formed via diastasis will typically be filled with sediment injected from less cohesive sedimentary units either directly above or below the cracked horizon [*Cowen and James*, 1992]. By contrast, subaqueous cracks on Earth that originate from gas expansion are commonly filled with *in situ* mineral precipitates [*Furniss et al.*, 1998; *Bishop and Sumner*, 2006; *Pollock et al.*, 2006]. In the case of the Sheepbed features, after crack formation, voids were filled by a succession of isopachous cement layers. The initial erosion-resistant cement layer is approximately 1 mm thick, measured normal to the crack surface, regardless of local curvature, and thus provides an equal-thickness coating on all available surfaces. Isopachous coatings indicate that the cement was precipitated in a phreatic, or water-saturated, environment (e.g. [*Longman*, 1980; *Amieux et al.*, 1989]). Erosionally-resistant isopachous cement is the defining attribute of the raised ridges throughout the observed Sheepbed member and likely reflects pore-fluid chemistry, or the chemical interaction between pore-fluids and released gasses, at the time of crack formation.

After this initial cement was deposited, an erosionally less-resistant cement precipitated within the remaining void space, further infilling and occluding the porosity. In wider cracks, this was followed by another erosionally resistant cement layer, and, if residual porosity remained it was occluded by a final, erosionally less-resistant cement. This type of layered and laterally repeated cementation of voids is common on Earth where it is utilized in "cement stratigraphy" [*Evamy*, 1969; *Meyers*, 1991], a methodology where sequences of different cement layers are traced on a regional scale and used to map ancient groundwater or pore water systems [*Grover and Read*, 1983; *Kaufman et al.*, 1988]. Different cement layers are usually attributed to evolving fluid chemistries, and sometimes related to distinct fluid flow events [*Meyers*, 1974; *Meyers and Lohmann*, 1985; *Dorobek*, 1987]. In the raised ridges, variation in erosional resistance of successive cement layers most likely indicates a change in cement composition that reflects changes in the pore fluid chemistry. Such interpretation is supported by the ChemCam observation that the outermost resistant cement is enriched in Mg and depleted in Al relative to the interior layers [*Léveillé et al.*, 2014]. At present, it is impossible to constrain the detailed timing of these different cement layers. Once the initial erosionally resistant cement was precipitated, it would have acted to reinforce void walls, permitting voids to potentially remain open for extended periods of time. The absence, however, of significant calcium sulfate mineralization within the cracks suggests that cementation of the raised ridges was complete prior to late-stage hydrofracture of the Yellowknife Bay formation [*Grotzinger et al.*, 2014; *Nachon et al.*, 2014].

3.5.3 Formation Summary and Comparison with Earth Analogs

Key first-order interpretations that we can derive from observations of the raised ridges are (1) the cracks formed during early diagenesis of the Sheepbed mudstone, (2) the cracks formed in a near-isotropic stress environment created by overburden pressure from overlying sediments, (3) mineral precipitation within the crack initiated soon after crack formation in a water-saturated environment, and proceeded with a series of precipitated cements of differing mineralogy and/or resistance to erosion, and (4) the morphology and distribution of the Sheepbed cracks matches the characteristics identified for synaeresis cracks, which form via sediment contraction with pore-fluid salinity changes, mechanical shaking, exsolution of pore-fluid gasses, or some combination thereof.

Having established this set of constraints concerning the early diagenetic, subsurface, pore-fluid saturated environment in which the raised ridges formed and filled, the remaining challenge is to evaluate the set of synaeresis crack formation hypotheses for applicability to the Sheepbed member structures based on Earth analogs. Although isolating specific crack formation mechanisms for subaqueous/shallow burial conditions is difficult for ancient sedimentary rocks, even on Earth, because of the absence of good modern analogs [e.g. *Smith*, 1968; *Frank and Lyons*, 1998; *Furniss et al.*, 1998; *James et al.*, 1998; *Pratt*, 1998a; *Marshall and Anglin*, 2004], the observations of the Sheepbed member and the restricted set of plausible environments on Mars help constrain the likely possibilities.

The most accepted hypotheses for synaeresis crack formation, as discussed, include (1) pore-fluid salinity changes causing clay layer collapse and volumetric shrinkage of the sediment, (2) mechanical shaking of the sediments causing tensional stresses, and (3) gas production in the sediment creating dilational stresses. Key observations in the Sheepbed unit that must be explained by the specific formation hypothesis include the clustered, irregular distribution of raised ridges, the lack of a preferred ridge orientation, and the cement (rather than sediment) crack infill.

Pore-fluid salinity changes causing clay layer collapse create synaeresis cracks preferentially in clay-rich areas [*White*, 1961; *Burst*, 1965]. This method of crack formation could create a clustered distribution of raised ridges if clay-rich zones were heterogeneously distributed in the mudstone. Although this is not specifically constrained by *Curiosity's* observations, since only two holes were drilled and sampled for XRD mineral compositions, it is plausible given the presence of smectite within the unit and the compositional differences between the John Klein and Cumberland drill sites [*McLennan et al.*, 2014; *Vaniman et al.*, 2014]. Preferred ridge orientations would not be expected for this formation mechanism as cracks would follow inhomogeneities in the sediment. Although cracks formed in this manner on Earth are usually preserved by sediment infill rather than precipitated cements, this mechanism for forming void spaces cannot be ruled out for the Sheepbed raised ridges.

Earthquake-induced shaking [*Cowan and James*, 1992; *Fairchild et al.*, 1997; *Pratt*, 1998b; a] or repeated wave action [*James et al.*, 1998; *Bishop et al.*, 2006] mechanically breaking up cohesive but unlithified sediments have also been used to explain synaeresis crack formation. There is no evidence for wave-induced sedimentary structures in the Sheepbed mudstone [*Grotzinger et al.*, 2014] and seismicity is rare on Mars

[*Anderson et al.*, 1977; *Golombek et al.*, 1992], however, impact-induced shaking could be a possible Martian alternative for mechanical shaking of sediments to form synaeresis cracks. The clustered distribution of cracks in the Sheepbed could be based on slight lithological differences in the sediment. However, cracks formed by this mechanism are inevitably preserved in ancient rocks by sediment infill rather than mineral precipitation, so this is not a favored hypothesis for the Sheepbed raised ridges.

Whereas both salinity changes and mechanical shaking could viably have occurred during deposition of the Sheepbed mudstone, the most distinctive characteristic of the raised ridges relative to the majority of terrestrial synaeresis cracks is that they are filled with cement, rather than sediment (e.g. [*White*, 1961; *Pettijohn and Potter*, 1964; *Burst*, 1965; *Cowan and James*, 1992]). The one notable terrestrial example of a class of synaeresis cracks where cement rather than sediment fills the voids is called “molar tooth” and the production of these structures is most often attributed to gas production in the subsurface [*Bauerman*, 1885; *Furniss et al.*, 1998; *Pollock et al.*, 2006]. This gas formation hypothesis predicts an irregular distribution of synaeresis cracks and other diagenetic morphologies based on minor differences in sediment lithology, and does not predict a preferred ridge orientation. Furthermore, molar tooth cracks are always filled with cement; the cements that fill molar tooth cracks precipitate so early that sometimes they are reworked during current scouring, leaving void-fill present as sedimentary clasts in immediately overlying beds [*Smith*, 1968; *O'Connor*, 1972; *James et al.*, 1998; *Bishop et al.*, 2006]. In terrestrial environments, these void-filling cements are primarily calcite, although in at least one location, early diagenetic saponite (presently talc) likely precipitates as cement [*Tosca et al.*, 2011]. Raised ridges within the Sheepbed member similarly contain early diagenetic cement infill, potentially smectite, and/or a chlorite phase such as akaganeite [*Léveillé et al.*, 2014; *McLennan et al.*, 2014].

The multiple morphologies of terrestrial “molar tooth” textures, all interpreted as due to gas production in the subsurface, invite further comparison with the diagenetic textures in the Sheepbed unit. The most common molar tooth morphologies are “ribbons” and “blobs” [*O'Connor*, 1972]. In scale and morphology, “ribbons”, the synaeresis-like components of molar tooth structure, are very similar to the raised ridges in the Sheepbed unit; they are narrow, at times sinuous, spindle-terminated cement-filled fractures and they are observed to transition between horizontal and vertical dimensions (Figure 3.6) [*O'Connor*, 1972; *Horodyski*, 1976; *Plummer and Gostin*, 1981]. Molar tooth "blobs" are typically mm- to cm-scale spheroidal pockets, suggested to have formed as gas bubbles, either interfingered with the ribbons or in separate clusters, filled with the same calcite cement [*O'Connor*, 1972; *Pollock et al.*, 2006]. These blobs may be comparable to the early diagenetic hollow nodules described in the Sheepbed unit as rimmed, erosion-resistant, spheroidal structures about 1.2 mm in diameter, that are clustered in some locations and laterally transition into raised ridge clusters [*Grotzinger et al.*, 2014; *Stack et al.*, 2014]. Both the ribbon and blob morphologies are explained by gas production in mudstone, where slight variations in lithology and cementation or in localized gas production have been used to explain transitions between unaltered mudstone, blobs, and ribbons [*Pollock et al.*, 2006]. These features are illustrated in Figure 3.6 with arrows pointing out the features that are also visible in the Sheepbed raised ridges (Figure 3.5). It is important to note that the cements that fill molar tooth structures are not isopachous and are not resistant relative to the surrounding rock, so the three-dimensional structure (including the sub-vertical to sub-horizontal transitions) is only visible when looking at the rock in cross-section (e.g. Figure 3.6c). However, comparison of the two-dimensional crack shapes reveals the similarity in spindle terminations, curvilinear crack geometry, clustered distribution, and transitions between morphologies. In summary, although the composition and style of the infilling cement in the Sheepbed unit is distinct from that usually found in molar tooth structures, the analog is unique because it is filled by cement rather than sediment, and because it suggests that gas formation or a similar single formation mechanism could potentially create more than one of the early diagenetic morphologies in the Sheepbed unit. This would fit with the observations of lateral transitions between diagenetic textures.

3.6 Summary

- Resistant cement-filled cracks ("raised ridges") in the Sheepbed mudstone were observed and mapped using imagery from the *Curiosity* rover.

- The raised ridges are shown to be early diagenetic features based on lateral transitions with other diagenetic textures. Later sulfate-filled veins crosscut these early diagenetic features.
- Comparison with analogous early diagenetic mud crack morphologies indicates that the raised ridges are synaeresis cracks (subaqueous shrinkage cracks).
- Isopachous cement fills with differing erosion-resistance likely represent a series of different cements indicating changing pore-fluid chemistries within the phreatic zone.
- Synaeresis crack formation mechanisms viable in the Sheepbed unit include pore fluid salinity changes causing volumetric shrinkage of smectitic clay fabrics, impact-induced mechanical shaking, or gas production.
- Proterozoic molar tooth structures, formed by gas production, provide an intriguing analog for the raised ridges because they (1) are cement-filled and (2) have multiple morphologies comparable to the diagenetic morphologies in the Sheepbed mudstone.

3.7 Appendix

3.7.1 Description of Processing of Mastcam Images

Mastcam images are acquired at 12 bits, with the noise level captured by the least significant bit. The data are then converted to 8-bit using an 11-bit lookup table. Although several tables exist, a modified square-root table (Figure 3.8) was used to encode the vast majority of the images. This table will encode multiple input values to a single output value, approximating the statistical variation of the signal. After encoding, the images are stowed within the camera’s large buffer memory. When downlinked, the images can be compressed with a predictive lossless compressor, or more normally, with a JPEG compressor with selectable quality factor. Typically quality factors of 85 or higher are used for geology targets.

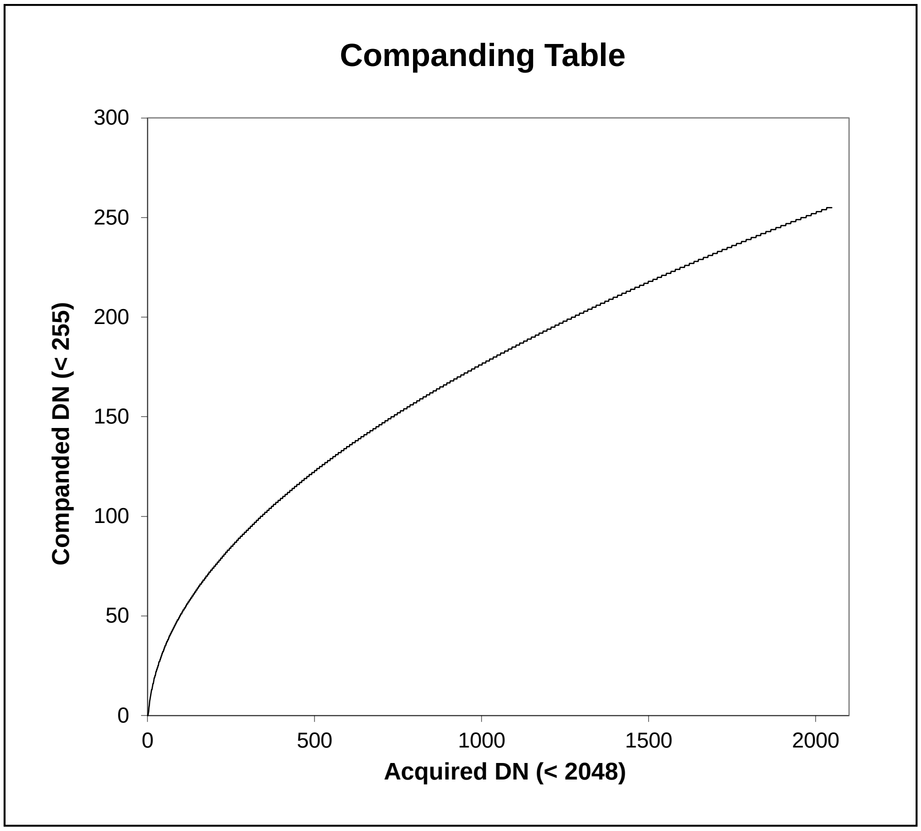

Figure 3.8 Plot of Mastcam Image Companding Table
Modified square-root companding table used to encode the images in *Curiosity*’s Mastcam buffer. Encodes multiple input values into a single output value to approximate the signal’s statistical variability.

3.7.1.1 Radiometric ground image processing

Radiometric ground image processing proceeds as follows: images are first decompressed and then expanded back to their original dynamic range using an inverse of the encoding table; no interpolation is applied in an attempt to recover the full variance around each mean value. For computational convenience, these data are stored in 16-bit words. A temperature dependent correction is then applied to adjust for thermally-generated electrons (noise). For short exposures, an electronic shutter smear correction is applied (generally, the images used in this study did not need this correction). A flat field correction is then applied to cancel lens brightness non-uniformity. The final photometric process is to adjust for detector sensitivity to create radiance images. Images that have gone through this processing are available through the Planetary Data System (PDS) as Reduced Data Records (RDR), designated by the letters in the Picture ID *_DRXX.IMG.

3.7.1.2 Geometric image processing

Geometric processing proceeds as follows: each image is geometrically linearized to remove camera lens distortion and prepare the image for further geometric processing. Images at this stage of processing are also available from the PDS as *_DRLX.IMG products. This processing is further described in the Mastcam/MAHLI/MARDI Software Interface Specification [*NASA-JPL*, 2013].

Images acquired as stereoscopic sets (pairs or larger mosaics) are aggregated into a separate directory and processed by a modification of the Ames Stereo Pipeline created by Mastcam Co-Investigator Laurence Edwards. This processing includes five steps. First relevant acquisition parameters are extracted from each image's metadata, its analogous pair is identified, and the images are converted from the PDS format to an internal format. Second, an image alignment is performed along with a reprojection transformation using the camera models (required because the two Mastcameras have disparate focal lengths). By default, the alignment and reprojection produces an epipolar aligned image pair, although other schemes can be chosen for unusual imaging geometries. Third, stereoprocessing of each image pair is completed: a filter is applied to each image that enhances edges and reduces sensitivity to differing lighting conditions. A pyramidal correlation scheme utilizing 3 or more reduced scale versions of each image and a fixed-sized correlation window quickly generate disparity search constraints. The initial search constraints are used as input to an integer correlator stage operating on the full resolution images. The results from the integer correlator are in turn utilized by a sub-pixel correlator stage generating dense high-resolution disparity maps with sub-pixel accuracy, and then automated pruning of bad correlations, based on a bi-directional consistency check and numerical confidence levels computed by the correlation software, occurs at each stage. Fourth, the final sub-pixel disparity map is interpolated and smoothed, and the camera models are used to generate 3D coordinates for each pixel where a valid match was determined. Fifth, output from each run includes intermediate processing images used in correlation, a pointcloud, XYZ maps, and mesh models in SGI OpenInventor format, with textures derived from the higher resolution camera image data (right eye). For multiple image stereo mosaics, an index mesh collection file is also created. All 3D data is in rover navigation coordinates.

The output of the stereo processing can be viewed in Triangulated Integrated Network (TIN) format in software capable of reading SGI *.iv files. For further processing into Digital Terrain Models (DTMs) and associated orthographic map projected images, the TIN to DTM conversion capability of the Ames Research Center Antares visualization software is employed. This software resamples the mesh into height and texture raster images, allowing the user to specify the sampling interval, interpolating where necessary. The final output consists of two GeoTiff image files: a signed 32-bit DEM, and a 24-bit (8 bits per channel) color texture image, both in orthographic projection, with labels in GeoTiff format and local site coordinates.

3.7.2 Location of Raised Ridges targeted by ChemCam

Raised ridge clusters outside of the range of Figure 3.3 that were targeted by ChemCam include Rowatt and Discovery Creek. The locations of these images in the Sheepbed unit are shown in Figure 3.9 along with the rover traverse through Yellowknife Bay.

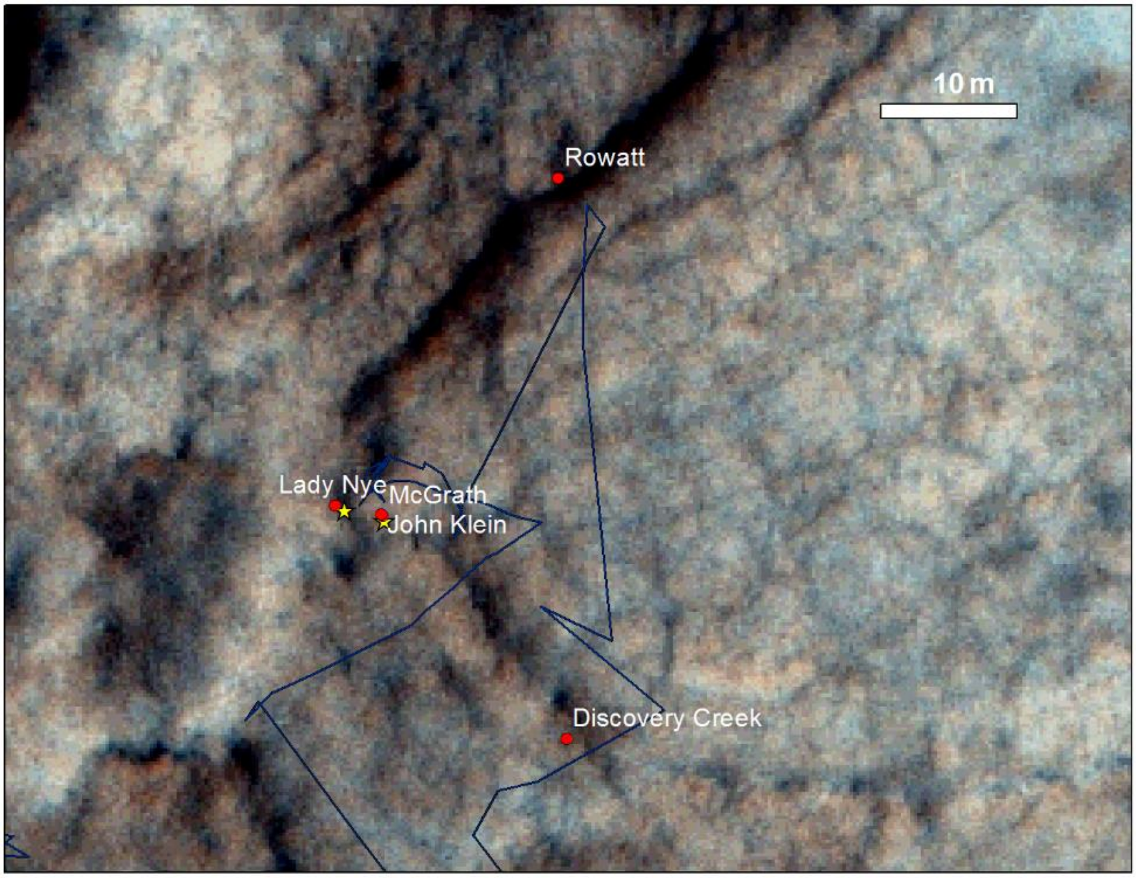

Figure 3.9 Map Showing Raised Ridge ChemCam Targets
Map showing locations of all raised ridge targets (red circles) that were shot by the ChemCam LIBS instrument. Yellow stars show drill sites, Cumberland on the left and John Klein on the right. Dark blue path represents rover traverse.

Acknowledgments

This work was supported by NASA Mars Science Laboratory grant 1449659 to JPG. We are grateful to our Mars Science Laboratory science team colleagues for helpful discussions, and particularly thank science team members J. Schieber and D. Oehler for helpful comments on an earlier version of this manuscript. Comments from two anonymous reviewers further improved this manuscript.

Chapter 4

Sorting out Compositional Trends in Sedimentary Rocks of the Bradbury Group (Aeolus Palus), Gale Crater, Mars

Kirsten L. Siebach, Michael B. Baker, John P. Grotzinger, Scott M. McLennan, Ralf Gellert, and Joel A. Hurowitz

Key Points

- *Curiosity* obtained bulk chemistry for sedimentary rocks in the Bradbury group
- Coarse-grained rocks are enriched in plagioclase
- Geochemical trends are consistent with mineral sorting during transport

Abstract

The compositional variations between sedimentary rocks analyzed by the *Curiosity* rover on the floor of Gale Crater are consistent with hydrodynamic sorting of mineral grains during transport from a relatively homogeneous basaltic provenance. During an 860-sol traverse across 9.5 km of the floor of Gale Crater, *Curiosity* obtained bulk chemistry measurements of over 100 fluvio-lacustrine sedimentary rocks in the Bradbury group using the Alpha Particle X-ray Spectrometer. These sedimentary rock compositions represent the set of source rock compositions altered by weathering, sorted by transport, and cemented during diagenesis. The Bradbury group samples are uniquely suited for sedimentary provenance analysis because they experienced negligible cation-loss, or open system chemical weathering, and their compositions can be modeled as sums of primary unaltered basaltic minerals using a Monte-Carlo model constrained by in-situ analyses. These samples were divided into seven categories based on grain size and texture, revealing that the coarse-grained textures are enriched in Al_2O_3, SiO_2, and Na_2O and the fine-grained textures are enriched in mafic components. Geochemical and mineralogical modeling shows that the variation between grain sizes is correlated to addition or depletion of plagioclase minerals relative to mafic minerals. The presence of a K_2O-rich stratigraphic interval within the Bradbury group shows that one other distinctive protolith contributed

to basin fill. However, the dominant compositional trends are defined by mineral sorting consistent with hydrodynamic sorting of coarse plagioclase grains and fine mafic fragments from breakdown of a porphyritic basaltic provenance during transport into Gale Crater.

4.1 Introduction

Sedimentary rocks are repositories for detrital grains that are derived from all rock types present in their watersheds, altered by weathering, sorted by transport processes, and cemented by diagenetic fluids. The Mars Science Laboratory rover, *Curiosity*, has shown that Gale Crater preserves remnants of originally significant volumes of sedimentary rock, creating both the modern floor of the crater (Aeolus Palus) and the 5-km tall stack of sediments in the middle of the crater that makes up Mount Sharp (Aeolus Mons) [*Grotzinger et al.*, 2015]. As of sol 860, *Curiosity* had traversed across 9.5 km of the crater floor and covered over 65 vertical m of stratigraphy dominated by lithified fluvial deposits known as the Bradbury group [*Grotzinger et al.*, 2015]. These sedimentary deposits are invaluable tools for understanding the nature and variety of rock types in the Noachian-era terrain that makes up the region around Gale Crater and which was eroded to produce the material that filled the crater basin. However, deriving provenance information from bulk compositions of sedimentary rocks requires accounting for weathering, transport, alteration, and cementation processes that could modify the sedimentary rock compositions relative to their sources.

The bulk compositions of sedimentary rocks are significantly simpler to relate to the compositions of their source rocks if no open-system chemical alteration — i.e., changes in the bulk chemistry related to preferential leaching or retention of select elements — has occurred due to initial weathering of bedrock source regions or due to later diagenesis during sediment burial. A useful tool for measuring the extent of open system chemical alteration with only compositional data in terrestrial and martian sediments is the Chemical Index of Alteration (CIA), a ratio of Al_2O_3 to labile cations designed as a chemical proxy for the degree of alteration of feldspars [*Nesbitt and Young*, 1982; 1984; *McLennan et al.*, 2014]. CIA values for Aeolus Palus are uniformly low, below even those values associated with incipient weathering, and the sediments fall within unaltered basalt compositions on a mafic ternary diagram, indicating that chemical alteration of these sediments has been cation-conservative at the scale of the bulk chemistry [e.g. *McLennan et al.*, 2014]. Based on this evidence, we proceed with the simplest interpretation of the CIA data, that there was no significant open-system weathering in Aeolus Palus sediments. Assumptions inherent to this model are discussed further below.

In the assumed absence of open system chemical weathering, there are three significant components that contribute to the composition of sedimentary rocks: (1) the source rocks in the watershed, (2) erosion and transport processes that sort detrital and mineral grains by size and density [*Fedo et al.*, 2015], and (3) addition of diagenetic cements [*McLennan et al.*, 2003; *Nesbitt*, 2003]. Each of these contributors must be considered as a possible source of compositional change before implications of compositional deviations can be assessed.

(1) The source rocks contributing to a watershed vary with space and time. Erosion is not uniform in space or time and can cause variations in the proportional contributions of different exposed rock units, and/or exposure of new rock units. For the Bradbury group, this problem is made tractable by (a) uniformly low CIA values, indicating that all or the large majority of contributing source rocks are primary basaltic rocks, with each reflecting equilibrium petrologic constraints [*Nesbitt and Young*, 1982; 1996], and (b) a series of measurements of rocks at different stratigraphic heights, allowing the ebb and flow of distinctive units to be traced [e.g. *Nesbitt and Young*, 1982; *Fedo et al.*, 1997].

(2) Rock breakdown [*Fedo et al.*, 2015] and transport [*Frihy et al.*, 1995; *Ferguson et al.*, 1996; *Nesbitt and Young*, 1996; *Komar*, 2007] processes have long been known to sort minerals and lithic fragments by size and density [*Mackie*, 1923]. Initial erosion/breakdown tends to isolate phenocryst minerals and can segregate other minerals based on erodibility [*Nesbitt and Young*, 1996; *Fedo et al.*, 2015]. Transport processes further sort both mineral grains and lithic fragments by density and size, sometimes well enough to create heavy mineral placers of economic significance [*Frihy et al.*, 1995; *Hughes et al.*, 2000]. These processes strongly affect the relationship between the sedimentary rock compositions and the source

rock compositions, and can be assessed by comparison of the sedimentary rock compositions with their grain sizes and depositional environments.

(3) Lithification of sedimentary rock typically involves physical compaction and chemical cementation by oversaturated groundwater fluids that interact with the sediments after they are deposited and precipitate minerals in the intergranular space [*Worden and Burley*, 2003]. Compaction alone does not change rock composition, but cementing interactions with groundwater fluids can alter the initial sediment composition by cement addition or by chemical alteration (dissolution and leaching of minerals in the detrital grains). Low CIA values likely indicate that diagenetic fluids did not significantly alter the compositions of the Gale Crater rocks, but possible addition of diagenetic cements must be carefully assessed by looking for compositional gradients or elemental enrichments within the rock suite. Cementation is assured for Bradbury rocks owing to their high degree of lithification and small amounts of residual porosity.

More than 100 measurements of the bulk compositions of outcrop and float rocks, taken by the Alpha Particle X-ray Spectrometer (APXS) instrument onboard *Curiosity*, provide a compositional dataset spanning a significant range of the rock textures and compositions present within Aeolus Palus. This study aims to use the compositions of the rocks observed by *Curiosity* to constrain a reasonable range of each of these effects, with implications for the range of contributing basaltic provenances and the extent of aqueous diagenesis.

4.2 Geologic Context

Gale Crater is a 155 km diameter crater sitting on fluvially dissected Noachian terrain on the Martian topographical dichotomy boundary. Crater counts of the ejecta blanket indicate that the impact occurred 3.8-3.6 Gya. Perhaps the most dominant feature of Gale crater is the 5-km-tall stack of sediments forming the crescent-shaped Mount Sharp (Aeolus Mons) in the center of the crater [*Malin and Edgett*, 2000]. This stack of sediments includes layers that were correlated with phyllosilicate and sulfate mineral detections in orbital spectroscopy datasets, and motivated the selection of Gale Crater as the landing site for the *Curiosity* rover [*Anderson and Bell*, 2010; *Milliken et al.*, 2010].

Comparisons between Gale and other complex craters of its size indicate that Mount Sharp is constructed around a tall central peak and the modern floor of Gale Crater is likely underlain by 1-2 km of sedimentary rock [*Grotzinger et al.*, 2015]. This and other work with infilled craters suggests that much of the crater was once filled with sediments, and the current topography is based on eolian erosion of the "moat" around the central peak/Mount Sharp complex [*Malin and Edgett*, 2000; *Farley et al.*, 2014; *Grotzinger et al.*, 2015]. This hypothesis implies that sedimentary rocks in the "moat" (Bradbury group) may be genetically related to the lowest exposed layers in Mount Sharp [*Grotzinger et al.*, 2015].

The *Curiosity* rover landed at Bradbury Rise, a topographic high within Aeolus Palus about 9 km from the geologic contact between the Bradbury group and Murray formation (Figure 4.1), and explored ~61 m of the Bradbury group stratigraphy. Lacustrine mudstones were discovered at the base of the stratigraphic section in Yellowknife Bay and also in the Murray formation at Pahrump Hills. The bulk of the intervening Bradbury group comprises a series of pebbly sandstones, conglomerates, and siltstone sedimentary rocks of fluvio-deltaic origin (Figure 4.1) [*Grotzinger et al.*, 2015]. While some large conglomerate clasts and float rocks are potentially igneous in composition, the observed stratigraphic sequence of in-place rocks in Aeolus Palus is composed exclusively of sedimentary rocks. All measured beds within this portion of the traverse are approximately horizontal, so we will assume that elevation is a good proxy for stratigraphic position within these units [*Grotzinger et al.*, 2014; *Grotzinger et al.*, 2015].

4.3 Methods

4.3.1 APXS

The Alpha-Particle X-ray Spectrometer (APXS) instrument mounted on *Curiosity*'s robotic arm enables in-situ X-ray spectroscopy, providing the average composition of a sample within a 1.7 cm diameter circle. The instrument uses X-rays produced by a ^{244}Cm source and the penetration depth varies between 2 to 80 μm for reported elements between

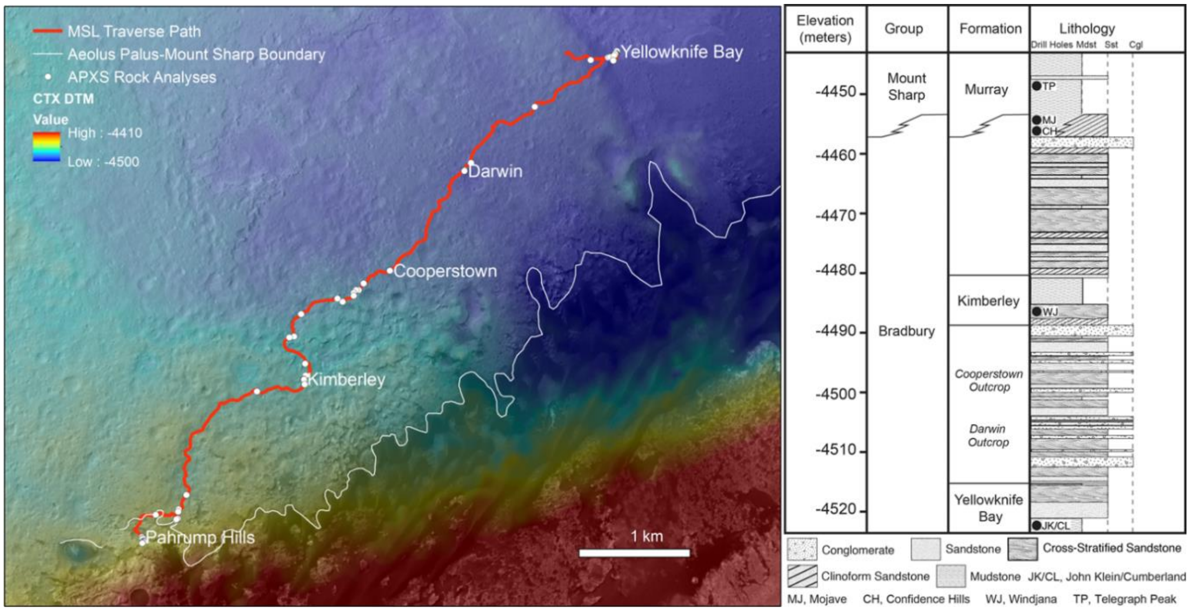

Figure 4.1 Overhead Map of *Curiosity* Traverse and APXS Locations
Overhead map showing the location and climbing elevation of the 9.5 km traverse path of the *Curiosity* rover during the first 860 sols after landing, with the stratigraphic column over the same portion of the traverse (based on elevation) on the right. Major outcrops labeled. Rover traverse begins west of Yellowknife Bay, jogs east to Yellowknife Bay, and then continues to the southwest. Locations of APXS analyses marked with white dots. White line on map represents main transition from Aeolus Palus (Bradbury group) rocks to Mount Sharp group rocks at the Pahrump Hills outcrop, reached on sol 750, although these facies are interfingered as shown in stratigraphic column.

Na and Fe, increasing with elemental mass. The intensity of characteristic X-ray energy responses from each element based on particle-induced X-ray emission and X-ray fluorescence is used to quantify elemental abundances for major elements and some trace elements [*Gellert et al.*, 2009; *Campbell et al.*, 2012; *Gellert and Clark*, 2015]. Regularly reported oxides and trace elements are (wt%): Na_2O, MgO, Al_2O_3, SiO_2, P_2O_5, SO_3, Cl, K_2O, CaO, TiO_2, Cr_2O_3, MnO, FeO_T, and (ppm): Ni, Zn, Br. Reported errors are statistical (2σ) errors based on the measurement duration, standoff distance, and temperature as reflected in the spectrum fitting routine, not errors associated with the instrument calibration. See Campbell et al. for more details on the instrument calibration and estimates of analytical accuracy [*Campbell et al.*, 2012].

APXS data are frequently normalized to remove volatile elements SO_3 and Cl (but not lighter elements) in order to correct for dust cover [*Rieder et al.*, 1997; *Schmidt et al.*, 2014]. This may be problematic if there is SO_3 or Cl in the rocks themselves or if there are excess light elements in the dust, and there is evidence that Martian magmas may be slightly enriched in sulfur and chlorine relative to terrestrial magmas [*Dreibus and Wanke*, 1985; *Filiberto and Treiman*, 2009], but it is a simple first-order correction. Here, we use sulfur- and chlorine-free normalization for mineral modeling. In element-element diagrams, in order to acknowledge the presence of dust but avoid assumptions about the dust and rock composition, we calculated the average weight percent that would have been removed had we normalized without SO_3 and Cl (avg SO_3 + avg Cl = 6%) and used this weight percent to make an acceptable error envelope around modeled predictions to compare to observations. This enables the reader to see the original measured APXS data, and the envelope surrounding an average dust-cover window without assuming any specific dust composition.

APXS targets are often analyzed under multiple conditions in order to obtain the most information possible from a contact science stop with the rover for that target. The same target spot may be analyzed at multiple times of day in order to work around planning schedules. A raster across the rock may analyze up to ~5 overlapping spots on a heterogeneous rock in order to constrain the compositions of the various components observed. A target may be analyzed as-is and then either analyzed with the ChemCam instrument (the shock front produced by the LIBS technique frequently removes dust) or brushed with the dust removal tool (DRT), and then analyzed with the APXS instrument again with less dust cover. In some cases, the target was analyzed only after dust removal. If a target was drilled, the drill tailings adjacent to the hole were analyzed, as well as the discarded sample processed by sieving. For targets within the Bradbury group, 112 APXS analyses were completed on or offset from 73 distinct named rock targets. The DRT was only used on 8 distinct named targets. For this study, in order to capture the variation between rock surface textures most completely, we include observations both before and after dust removal as distinct observations. In cases where the same target was analyzed at multiple times of day, we use only the observation with the longest integration time (or best distance to target and thermal conditions), judged by the smallest reported statistical error associated with the measurement. Overlapping, or ‘offset’ targets are typically included, because variability occurs on short distance scales, but these are excluded to minimize bias in some plots (labeled as ‘offset targets excluded’).

4.3.2 MAHLI

The Mars Hand Lens Imager (MAHLI) instrument is a high-resolution focusing color camera mounted on *Curiosity*’s robotic arm. It can focus between ~2.1 cm and infinity and is typically used for high-resolution (14+ µm/pixel) imaging of targets of interest, including all APXS targets [*Edgett et al.*, 2012]. For this study, the MAHLI images taken with ~5 cm standoff distance (~30 µm/pixel) for each of the APXS targets were used for initial textural comparison. In the few cases where such imagery was not taken, higher standoff distances or images from the Mastcam were used to determine textures. For some targets, higher resolution imagery was also available and this was used whenever possible to clarify grain sizes and compare textures.

4.4 Results

4.4.1 Rock Classification by Texture

The classification of detrital sedimentary rocks is typically based on the sizes of the grains within the rock. On Mars, grain size assessment can be complicated because of several reasons: first, the MAHLI resolution limit at a typical standoff distance is ~ 30 µm/px, so only distinctive grains larger than ~50-100 µm are distinguishable; second, the in-situ rock surfaces are frequently dust-covered, obscuring grain boundaries; and third, many of the targets *Curiosity* has observed have extremely homogeneous coloring, making it even more difficult to clearly distinguish grains from cement or matrix. Therefore, for the collection of targets that MSL analyzed with APXS and MAHLI in the first 860 sols, the classification system defined here was based on grain size wherever possible, surface texture and coloring when grain sizes could not be distinguished, and the two mudstone formations (Sheepbed mudstone of the basal Bradbury group and Murray formation mudstone of the Mount Sharp group exposed in the Pahrump Hills) were separated by stratigraphic group. Samples with clear diagenetic overprinting (e.g. nodular and dendritic concretions, fracture fills) were further split into their own category. In total, eight textural classes were identified to encompass the range of MAHLI and APXS targets observed by *Curiosity* in the first 860 sols: Sheepbed mudstone (Figure 4.2a), fine sandstone (Figure 4.2b), sandstone (Figure 4.2c), conglomerate (Figure 4.2d), uncertain (Figure 4.2e), possible igneous (Figure 4.2f), diagenetic (Figure 4.2g), and Murray mudstone (Figure 4.2h). Each of these textural classes is described in detail below:

Sheepbed Mudstone. (n = 10, Figure 4.2a) The Sheepbed mudstone member is the lowermost stratigraphic unit of the Yellowknife Bay formation, described in detail in Grotzinger et al (2014). The rock texture in this unit was extremely smooth at the MAHLI resolution (up to 15 µm/pixel). There were a variety of diagenetic targets within this unit (n=20) where we examined concretions, raised ridge features, and/or light-toned veins, which were categorized as diagenetic targets and excluded from the Sheepbed mudstone category. Several of the observations in this category were on dusty surfaces.

Fine Sandstone. (n = 15, Figure 4.2b) The fine sandstone category includes observations of sandstones or siltstones with grain sizes approximately at the MAHLI limit

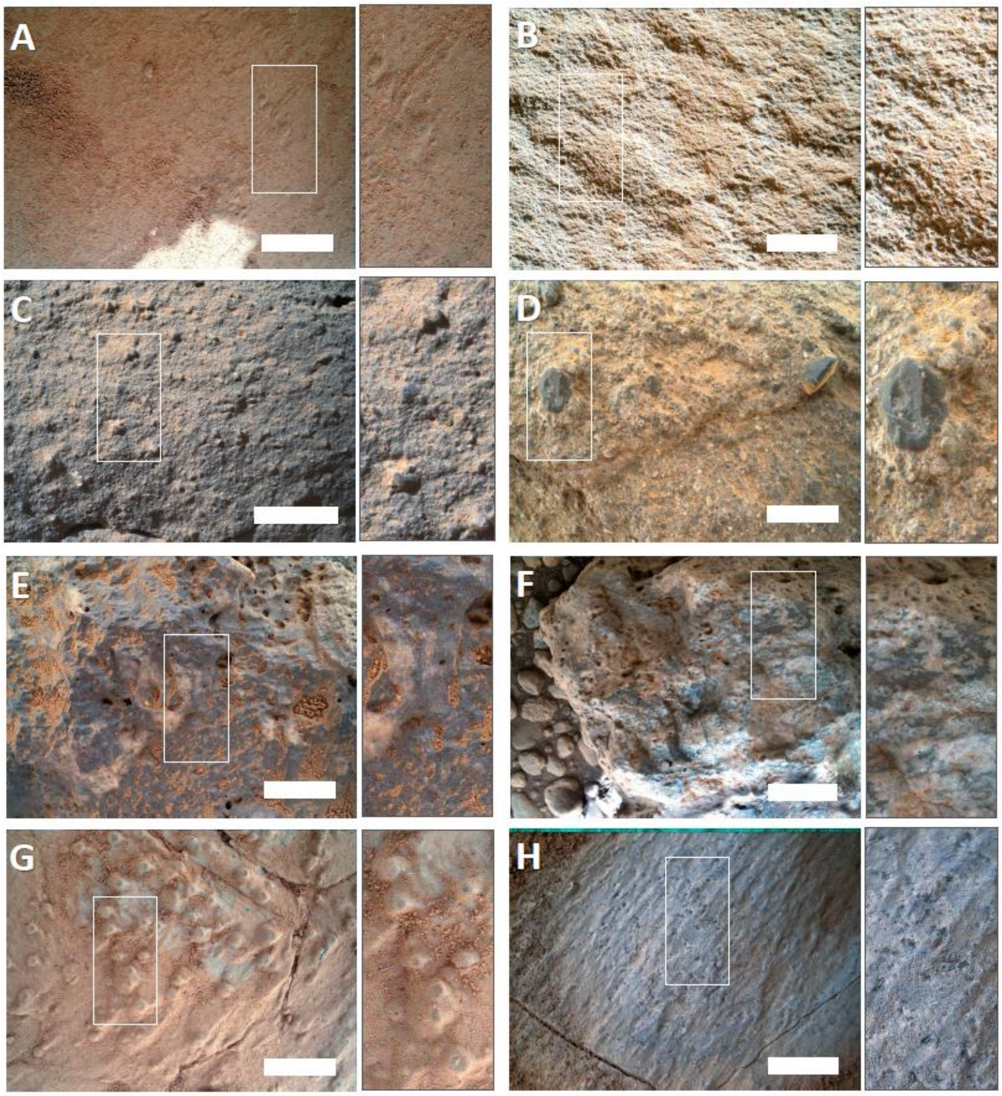

Figure 4.2 MAHLI Image Examples of Textural Classification Scheme
Examples of each of the textural classes of rocks in the Bradbury group (a-g) and the Murray mudstone in the Mount Sharp group (h). White scale bars are 1 cm across. Classes were divided on the basis of grain size and/or surface texture and coloring, and include: (a) Sheepbed mudstone (n=10), exposed in Yellowknife Bay with grains finer than the limit of resolution, (b) Fine Sandstone (n=15), well-sorted siltstones to sandstones, (c) Sandstone (n=24), medium to pebbly sandstones, (d) Conglomerate (n=15), primary grain sizes >1 mm, rounded grains, clasts up to 6 cm, (e) Uncertain (n=15), float rocks with poorly-defined grain boundaries, sometimes weather like conglomerates (f) Possible Igneous (n=4), small group of float rocks and one clast in a conglomerate with porphyritic textures like igneous diorites (g) Diagenetic (n=39), rocks with clearly diagenetic textures including preferential cementation and fracture fills, and (h) Murray Mudstone (n=27), mudstone observed at Pahrump Hills in Mount Sharp group, fine-grained with potential secondary crystal structures.

of resolution. These are all well-sorted siltstones to fine sandstones and do not have visible grains larger than ~200 µm.

Sandstone (n = 24, Figure 4.2c) The sandstone category includes observations of medium grained, sometimes pebbly, sandstones that are primarily composed of <0.5 mm grains. These grains (exclusive of sparse pebbles) range from well-sorted to poorly-sorted. Void space mapping in these samples indicated that apparent primary porosity is quite low, so these samples were well cemented, although some secondary porosity is apparent (potentially because of surface weathering). Where pebbly, clasts range up to a centimeter in diameter and are dispersed in the sandstone matrix.

Conglomerate (n = 15, Figure 4.2d) Conglomerate targets include those targets with primary grain sizes >1 mm. These are typically poorly sorted and show variable cementation, both within a given outcrop and across the traverse. Some of these targets have significant dust cover. Individual clasts, where identifiable and not dusty, range from light-toned to dark-toned, and from sub-angular to sub-round. The largest clasts are up to 6 cm across. Endmembers of this class range from variably-cemented rocks with clearly identifiable grains (e.g. Mount Bastion sol 399, Bardin Bluffs sol 394) to well-cemented conglomerates that are more homogeneous in color but have a vuggy surface texture from weathering that reveals clast boundaries (e.g. Oneida sol 506, Jum Jum sol 550).

Uncertain (n = 15, Figure 4.2e) The uncertain category contains a subset of float rocks whose dust cover and weathering textures make it difficult to define any grain boundaries, indicating that either the grains are below the resolution limit of the image or they are well-cemented and relatively homogeneous in color. A number of rocks in this category have some weathering textures or color changes that hint at the presence of larger grains, but these are not well-defined. Some of these rocks look very similar to the well-cemented conglomerates with homogeneous surface color, but they are assigned to this category because the grain boundaries are not defined and their context is uncertain because they are float rocks (e.g. Nedrow, sol 503; Kodak, sol 512; Monkey Yard, sol 564). Other rocks in this category show some variability in color, including several-mm light-toned patches that blend back into the dark grey rock, but the colors blend together instead of creating sharp grain boundaries (e.g. Morehouse, sol 503; Lowerre and Larrabee, sol 510).

Finally, a few rocks in this category do not show any clear evidence for visible grains, and may be quite fine-grained. These tend to weather with a vuggy texture that further obfuscates their origin. Some of these have been categorized by other authors in dramatically different ways, for example as fine-grained igneous rocks, or alternatively as iron-oxide-cemented fine grained sedimentary rocks (e.g. Jake Matijevic, sols 46 and 47; Et Then, sols 86 and 90; Secure, sol 560) [*Stolper et al.*, 2013; *Blaney et al.*, 2014] and accordingly, some caution is warranted in discussing these rocks.

Possible Igneous (n = 4, Figure 4.2f) A small subset of float rocks and a large clast within a conglomerate have relatively dust-free surfaces where we observe interfingered light and dark patches whose color does not relate to grain boundaries, but instead creates (in some examples) a porphyritic texture suggestive of igneous diorites (e.g. Clinton, sol 512; Ruker, sol 387; Reedy, sol 526). These rocks are categorized as possible igneous because we see some igneous texture, but we cannot exclude the possibility that the sample is sedimentary and composed of cemented igneous phenocrysts.

Diagenetic. (n = 38, Figure 4.2g) A variety of diagenetic features have been identified during the traverse, including nodular concretions [*Stack et al.*, 2014], raised ridges [*Siebach et al.*, 2014], light-toned veins [*Nachon et al.*, 2014], and dendritic concretions [*Grotzinger et al.*, 2015; *Kah et al.*, 2015]. Targets on these features that are clearly related to diagenetic fluids and preferential or replacement cementation are categorized as diagenetic targets. Diagenetic targets do not fit the assumption of only closed-system weathering, so these targets are not used to constrain source rock chemistry.

Murray Mudstone (n = 27, Figure 4.2h) On sol 750, *Curiosity* crossed the boundary between Bradbury group alluvial fan and delta deposits, derived from the northern rim of Gale, and the lacustrine mudstones of the Murray formation, the stratigraphically lowest unit of the Mount Sharp group [*Grotzinger et al.*, 2015]. As a lake deposit the mudstone may be derived from multiple sources, given that slopes transporting sediment dip from all directions toward the northern crater moat where the Murray mudstone accumulated. We include samples of the Murray formation exposed at Pahrump Hills (up to sol 860) for comparison to the Bradbury group rocks that compose the other 7 categories. The Murray formation at Pahrump Hills is interpreted to be a mudstone because of its fine grain size, below the limit of resolution. It is interpreted as a lake deposit due to its fine grain size, its laterally continuous millimeter-scale lamination, and its paleogeographic position downslope of delta deposits [*Grotzinger et al.*, 2015]. Locally, the laminated mudstones are overprinted by diagenetic concretions and secondary crystals interpreted as evaporite mineral molds [*Grotzinger et al.*, 2015; *Kah et al.*, 2015].

4.4.2 APXS Compositional Trends with Texture

In order to test whether sample composition varies systematically with grain size, the textural categories defined in the last section were arranged in order of increasing grain size as much as possible. The Murray mudstone (Mount Sharp group) and Sheepbed mudstone (Bradbury group) make up the finest grained endmembers, then the categories for which grain size is measureable follow in order of increasing grain size: fine sandstone, sandstone, and conglomerate. Diagenetic samples were excluded from this analysis. However, uncertain and possible igneous, were included as coarse grained endmembers because texturally, the uncertain category frequently looks most similar to the conglomerates category despite the lack of distinguishable grains, and the possible igneous category includes samples that represent large clasts within conglomerates, which by definition are the coarsest grains. This ordering also parallels and enhances the compositional trends, as shown in Figure 4.3, although the trends are visible even when these categories are excluded because of their lack of measureable grains.

Figure 4.3 shows that the elemental abundances measured by APXS vary systematically with the grain size, or textural category, of the Bradbury rocks. SiO_2 (Figure 4.3a), Al_2O_3 (Figure 4.3c), and Na_2O (Figure 4.3e) are most enriched in the coarsest grained textural categories, whereas FeO_T (Figure 4.3b), MgO (Figure 4.3d), and TiO_2 (Figure 4.3f) are most enriched in the finest grained textural categories. Likewise, Cr_2O_3, MnO, Ni, and (less clearly) Zn and Br are enriched in the finest grained textures, whereas P_2O_5, SO_3, CaO, Cl, and K_2O do not show a correlation with grain size. These trends are most clearly defined by the variation between the fine sandstone, sandstone, conglomerates, and uncertain/possible igneous categories. Although it is the finest grain size fraction, the Sheepbed mudstone (red in Figure 4.4) is not always the compositional endmember, which

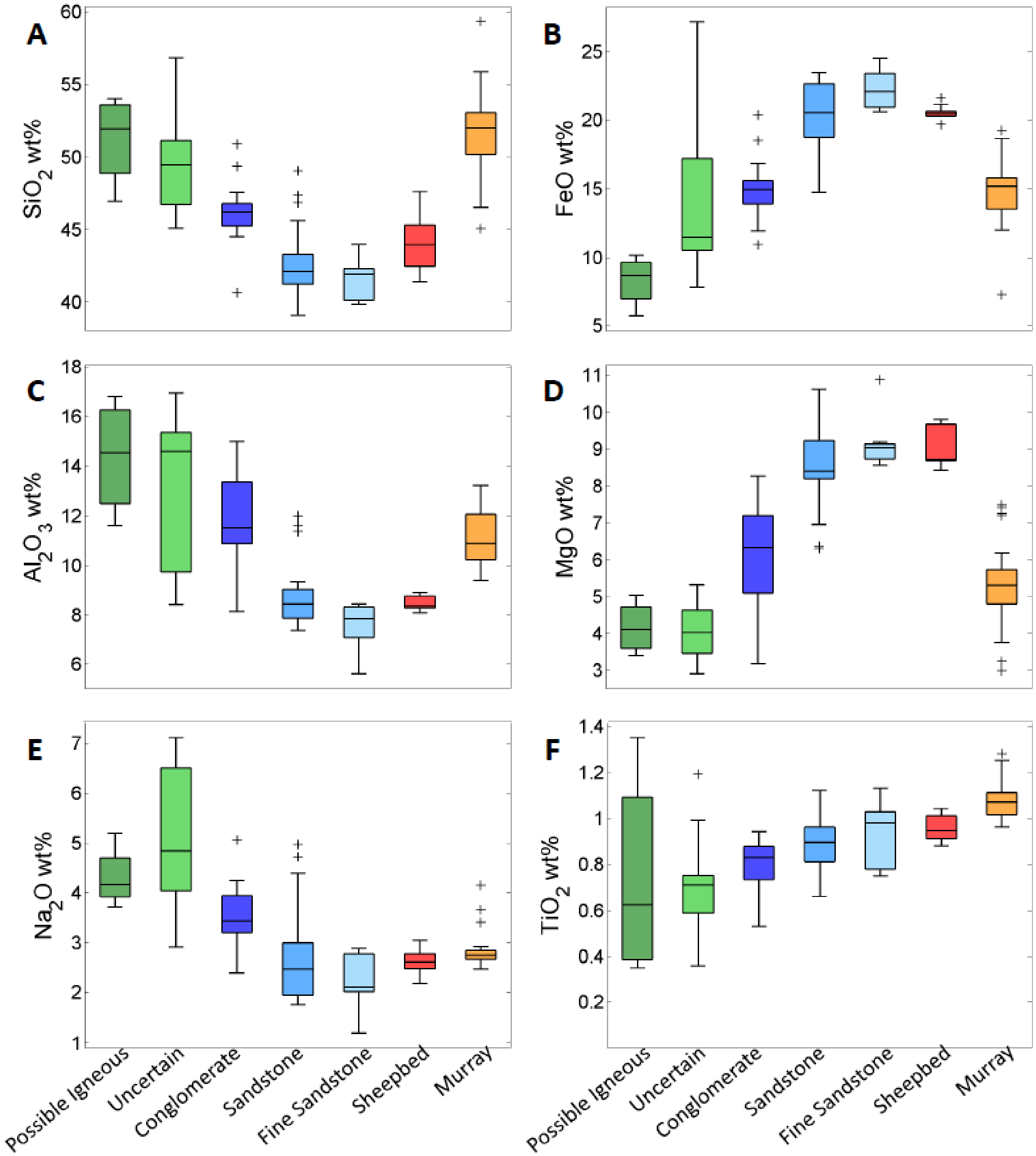

Figure 4.3 Boxplots showing Compositional Differences between Textural Classes

Boxplots showing the major elemental compositions of each of the textural classes of Bradbury group rocks ordered from coarsest grained on the left to finest grained on the right in red, and Murray mudstone samples in orange. For each textural group, dark central line represents median data point, colored box encompasses 25th and 75th percentiles, whiskers typically extend to minimum and maximum data points, but the maximum whisker length is 1.5 times the length of colored box, and crosses demarcate outlier points. Trends show higher concentrations of SiO_2, Al_2O_3, and Na_2O in coarser-grained textures and higher concentrations of FeO, MgO, and TiO_2 in finer-grained textures.

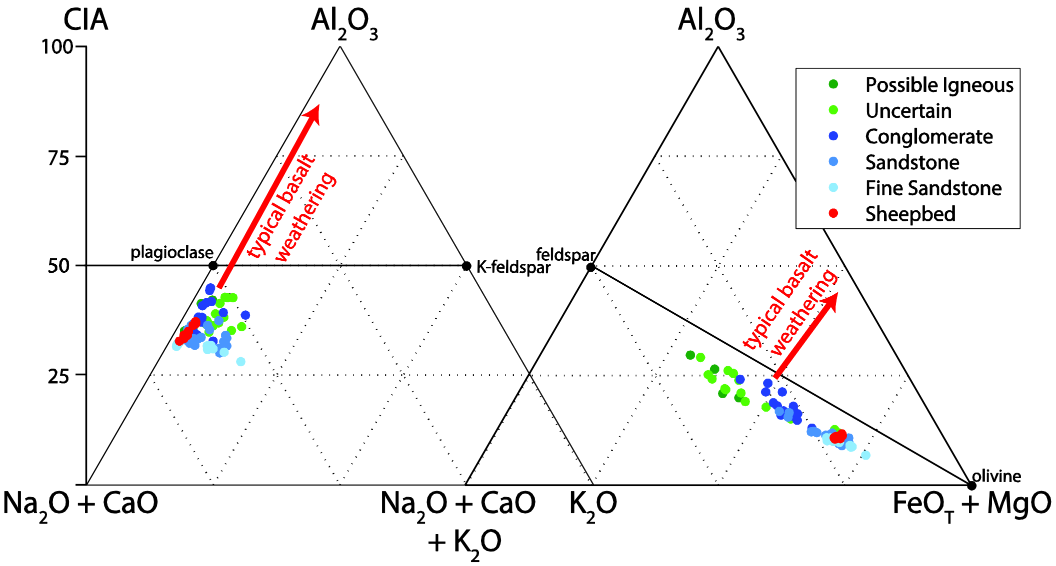

Figure 4.4 Ternary Diagrams for Bradbury Group Textural Classes
Al_2O_3-(CaO + Na_2O)-K_2O (left) and Al_2O_3-(CaO + Na_2O + K_2O)-(FeO_T + MgO) (right) ternary diagrams showing the elemental compositions of Bradbury group rocks based on mole fractions. Diagenetic and Murray mudstone textures excluded. Typical terrestrial basaltic weathering trends demarcated with red arrows. Chemical Index of Alteration (CIA) scale, on left, describes molar ratio of labile cations to Al_2O_3 content and is a measure of feldspar weathering.

is consistent with the mudstone being a lake sediment that is more likely to accumulate detrital inputs from multiple sources, instead of only the source region for the larger-grained fluvial sediments. The uncertain category frequently has a wider range of compositions than the other categories, as these incorporate float rocks that may not all be part of the Bradbury group depositional system.

To first order, for the Bradbury group, these results indicate that the chemical components of felsic minerals (Al_2O_3, SiO_2, and Na_2O) are concentrated in the coarsest-grained fraction of the sedimentary rocks, and the chemical components of mafic minerals (FeO_T, MgO, TiO_2, Cr_2O_3, MnO, Ni) are being concentrated in the finest grained fraction of the sedimentary rocks. These trends describe much of the compositional variability in the Bradbury group rocks, as shown in A-CN-K and A-CNK-FM ternary diagrams in Figure 4.4. Most of the compositional variability between samples is along the feldspar-FM join in the mafic ternary plot and correlated with the sample textures, indicating a distribution between mafic minerals and feldspars, but there is no evidence for significant cation-exchange weathering, which would drive the trends in the direction of the red arrows on Figure 4.4.

This result clearly indicates that composition is related to grain size in the Bradbury group. Assuming negligible chemical weathering, this result could be explained by physical breakdown and transport processes segregating mineral grains, two distinctive source rocks contributing different grain sizes, or a combination of the two. The next several sections describe a series of tests designed to investigate how well these different models explain the spread in the data by first considering why K_2O does not trend with texture, and then testing:

(1) Does the compositional data fit a basic geochemical mixing model for sorting of plagioclase grains from average Mars crustal composition?

(2) Does the compositional data follow igneous differentiation trends from the liquid line of descent of a similar alkali ocean island basalt sequence on Earth?

(3) Does a model that estimates reasonable mineral compositions from the APXS compositional datasets indicate that the rocks could all be consistent with an igneous provenance?

4.4.3 Potassium vs. Stratigraphic Elevation

Potassium is an incompatible element in igneous systems, and therefore makes a good tracer for distinctive igneous sources [*Gast*, 1968; *Engel et al.*, 1974], especially for sources that have experienced minimal degrees of weathering [e.g. *Nesbitt and Young*, 1984]. It is particularly interesting in the Bradbury group because it does not trend with texture like the other felsic mineral components (Al_2O_3, SiO_2, and Na_2O), and instead K_2O appears to be highly concentrated at up to 4% in a few stratigraphic intervals, whereas average Mars crust is 0.45% [*Taylor and McLennan*, 2009]. Across the 9 km traverse in Aeolus Palus, the sedimentary layers are extremely flat-lying, with measured dips of 0 to +/-3 degrees [*Grotzinger et al.*, 2015], so elevation is used as a simple proxy for stratigraphic layer in Figure 4.5. This shows that the K_2O/Na_2O ratio shifts from a steady average of 0.5 to up to 2.5 in samples measured around -4480 elevation, including the Kimberley outcrop. The high potassium (2+ wt%) is found in targets in all of the textural categories that were sampled near that elevation, including fine sandstone, sandstone, conglomerate, and uncertain, but there are no clear textural correlations with potassium within those elevations (such trends may exist, but in this case would likely be obscured by limited sampling, dust cover and/or sampling bias within the relevant elevations). The Windjana sample, a fine sandstone drilled at that outcrop, contains 21% potassium feldspar by weight based on CheMin x-ray diffraction data [*Treiman et al.*, 2015]. This work indicates that a distinctive source of potassium-rich sediments contributed to the Kimberley formation, located within the middle of the Bradbury group [*Treiman et al.*, 2015]. While the source of the potassium is worthy of discussion, the consistent K_2O/Na_2O ratio throughout the rest of the Bradbury group shows that whatever the source of potassium here, it does not explain the other major compositional trends.

4.4.4 Modeling trends as a two-component mixture

In order to test the hypothesis that the variability expressed in Bradbury group compositional data can be accurately described as the separation of coarser-grained plagioclase from the finer-grained mafic portion of a relatively typical martian basalt, we use a two-component mixing model [*Langmuir et al.*, 1978]. The model shows the

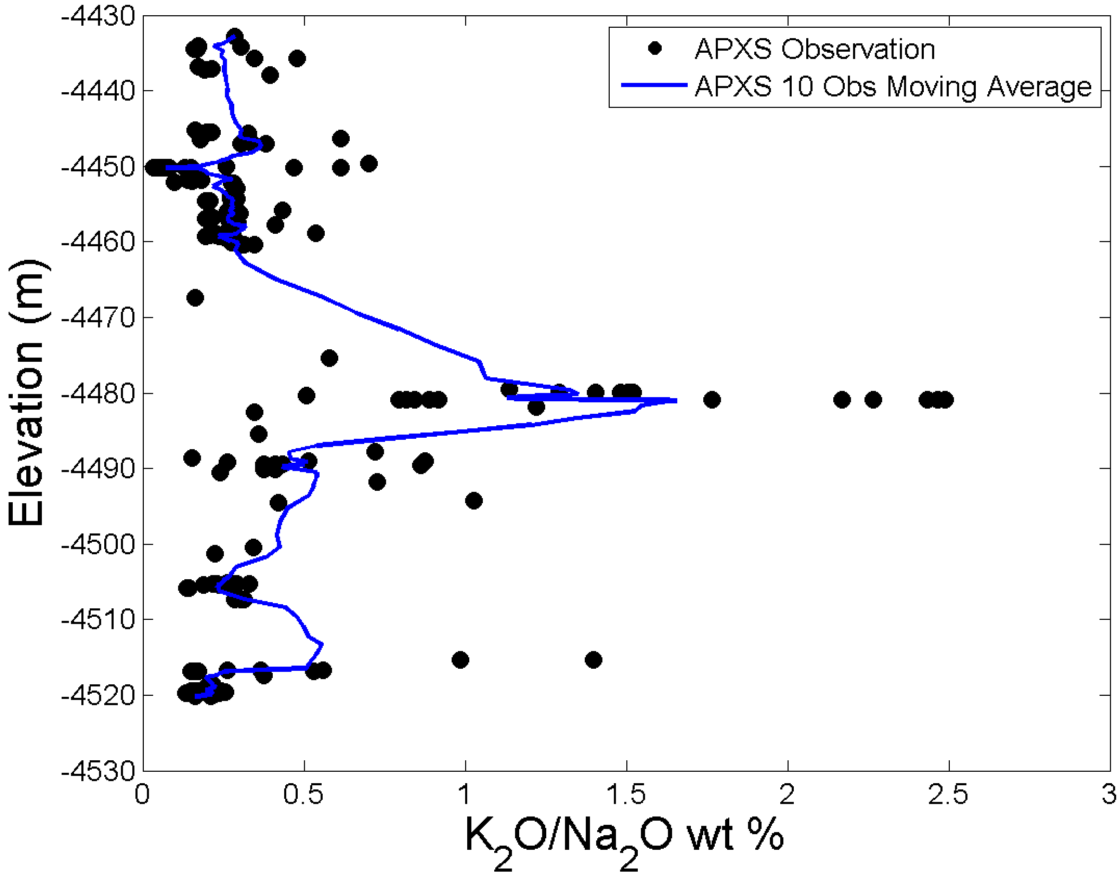

Figure 4.5 K_2O/Na_2O vs. Elevation in Samples to Sol 860
Plot of K_2O/Na_2O ratio vs. elevation for each APXS rock sample (excluding diagenetic, but including float rocks). Blue line is 10-point moving average with elevation.

expected trend of average Mars crust basalt plus-or-minus normative plagioclase, which can then be compared to the trend and spread of the APXS dataset. The advantage of using a two-component mixing model is that it is a hypothesis-driven approach to testing when the dataset does or does not fall along the model for each element-element plots. Deviations from the model can then be explained.

4.4.4.1 Methods

Average Mars crust was defined as the starting point for the two-component mixing model because it provides a comparison to other Martian datasets [*Taylor and McLennan*, 2009]. Although the measurements at Gale indicate that the local Noachian crust is more alkaline and mafic than average Mars crust [*Stolper et al.*, 2013; *McLennan et al.*, 2014; *Treiman et al.*, 2015], those compositional differences are relatively small and will be reflected as offsets from the model, which can be easily identified. The felsic endmember for the model is the CIPW normative plagioclase based on the average Mars crust composition, An40. This is quite close to the An36 measured by CheMin for the Sheepbed mudstone [*Morrison et al.*, 2015], so it provides a good starting plagioclase endmember value. Any deviation from this value would result in a change in the angle of the trend created by the measured sediments relative to the angle expected for an element-element plot based on the model. The overall two-component mixing model, shown for FeO vs SiO_2 in Figure 4.6a, therefore simply represents a line between the composition of plagioclase An40 and the mafic component of average Mars crust, or the composition of Average Mars crust minus the composition of An40 plagioclase.

The presence of variable dust cover on the observed APXS samples presents a complication for the two-component mixing model. The precise composition of the dust is unknown, and there are very few brushed samples to compare with unbrushed samples to obtain a robust estimate for dust composition. A common solution is to use the wt% of SO_3 + Cl as a proxy for dust and soil cover for each sample, and to divide those two components out and renormalize all other elements to 100 wt% [*Rieder et al.*, 1997]. This approach assumes that there is negligible SO_3 or Cl in the rocks themselves, and that the dust contains no other significant elements, which may be poor assumptions here. In order to use this

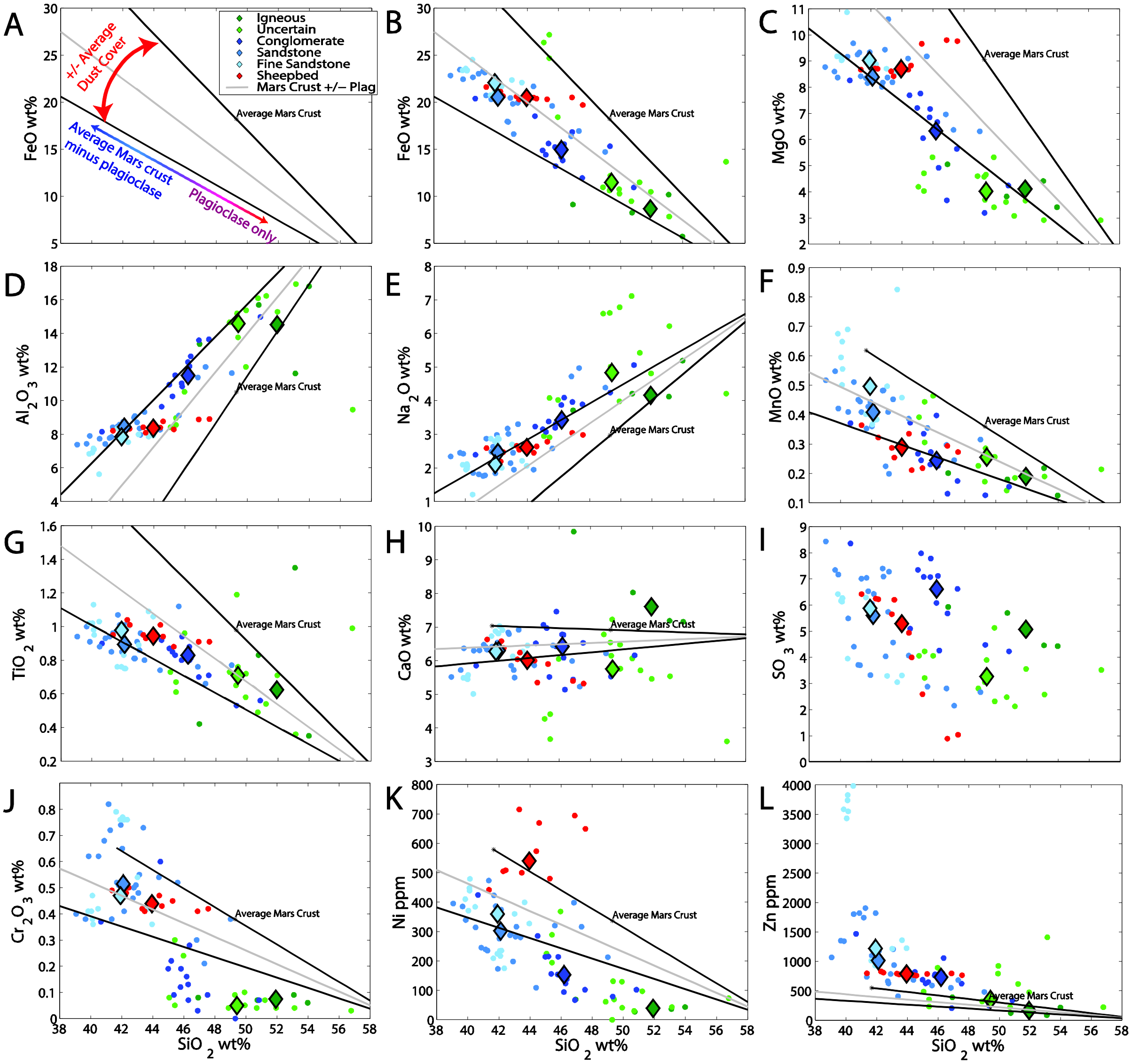

Figure 4.6 Two-Component Geochemical Model for Plagioclase Addition/Subtraction

Element-SiO_2 plots showing Bradbury group compositional data compared with two-component geochemical model for segregation of average Mars crust normative plagioclase (An40), high SiO_2, marked in red in part (a), from the mafic components of average Mars crust, low SiO_2, marked in blue in part (a). Grey line shows geochemical model for average dust cover, black lines represent envelope between no dust cover (marked with average Mars crust composition), and 2x average dust cover. Colored points represent APXS samples, excluding diagenetic samples. Diamonds are median values for each textural group.

approach but avoid assumptions about the dust composition, we use the average concentration of SO_3 + Cl for all included samples (6.1 wt%) as an acceptable error window around the predicted model composition. Since the reported average Mars crust values include no SO_3 or Cl, we dilute the average Mars crust model by 6.1% to obtain expected model values for analyses with average dust cover. We then present the model with an acceptable error window, bracketing the expected model values (with average dust cover, or a 6.1% dilution factor) with lines that represent average Mars crust (0% dust cover) and twice the average dust cover (a 12.2% dilution factor) (Figure 4.6a).

4.4.4.2 Results

Several of the element-element plots with modeled mixing lines and APXS data are shown in Figure 4.6. For most major elements in Bradbury group samples, compositional variation trends are consistent with the modeled trend of addition or subtraction of plagioclase. Furthermore, the variation along this plagioclase addition/subtraction trend parallels the differentiation between samples by grain size, suggesting again that this primary axis of compositional variation is coupled with sediment grain size.

The two-component model is a forward model with built-in assumptions, so minor differences between the model and the plotted samples are expected. Data variability within the black lines designed to show the range of 0-2x average dust cover is assumed to be primarily due to variations in dust cover. Further scatter may be due to minor or local secondary processes. Beyond scatter, there are three main types of differences between sample compositions and the model based on average Mars crust: (1) offsets related to differences between average Gale Crust and average Mars crust, (2) angular differences between the trend from the samples and the model prediction related to differences between samples that are not captured by An40 plagioclase addition/subtraction, and (3) data clouds instead of trends for elements whose distribution is unrelated to grain size or plagioclase variations. That is, only elements previously identified as having no compositional trend with grain size (Figure 4.3) fall into this category, including P_2O_5, SO_3 (Figure 4.6i), CaO (Figure 4.6h), Cl, and K_2O.

Offsets between the modeled composition based on average Mars crust and the typical Bradbury compositions occur for certain elements, indicating that the average basaltic crust composition around Gale Crater is different from the predicted average Mars Crust. For major elements, SiO_2 (Figure 4.6) and MgO (Figure 4.6c) in Gale are slightly lower than average Mars crust, and FeO_T is slightly elevated above crustal values (Figure 4.6b). K_2O and Zn (Figure 4.6l) are significantly elevated above Mars crustal values in nearly all Bradbury samples. This is consistent with observations made for the Yellowknife Bay formation [*McLennan et al.*, 2014] that indicate that the crust around Gale is more mafic than average crust.

Angular offsets between modeled plagioclase addition/subtraction and the dataset trends show where there are additional factors affecting the data that are not accounted for in the model. The largest angular offsets are in Cr_2O_3, Ni, and Zn (Figure 4.6j, k, and l), all of which are more strongly correlated with grain size than the model predicts. These three elements are highly concentrated in the finest grain sized samples such that their concentrations dramatically drop off with increasing grain size, and are especially low in rocks in the uncertain and possible igneous categories (Figure 4.6j, k, and l). In the other direction, TiO_2 and Al_2O_3 are slightly less strongly correlated with grain size than the model predicts, creating much smaller angular discordances (Figure 4.6d, g). These will need to be accounted for in an overall model of the system.

4.4.5 Comparison with Igneous Evolution Trends

One of the hypotheses for explaining compositional, and likely mineralogical, variation with grain size would be that the more felsic grains come from a different igneous flow than the more mafic grains, implying the presence of magmatic compositions equivalent to or more extreme than the observed endmember rock compositions. In this scenario we must assume that more felsic igneous rocks exist in the same watershed and in close spatial association with the more mafic rocks since both would need to contribute detritus to the same sedimentary rocks. While the two rock types are not required to be genetically linked, it is simplest to initially assume that the initial regional magmatic composition is the same and the different rock types represent different compositional states of that magma as it cools down a liquid line of descent. In this case, we would likely observe mixed detrital sediments from igneous rocks representing a series of intermediate compositions following the liquid line of descent of the magma. In order to test the similarity of the compositional trends measured in the Bradbury group to the trends produced during cooling of magma along the liquid line of descent, we plot the Bradbury trends (excluding Murray formation and diagenetic samples) against compositional data from igneous samples in the Tenerife alkaline ocean island basaltic sequence (Figure 4.7). Major elements are plotted against MgO content because the amount of MgO is related to the evolution of the basalt from the initial magma.

It is important to recognize that Figure 4.7 compares igneous rocks with sedimentary rocks inferred to be derived from igneous rocks, and is not designed to be a direct comparison of igneous evolution pathways. The goal here is rather to understand how the compositional trends in the Gale Crater dataset compare with igneous differentiation trends for similar bulk basaltic compositions. In that regard, Tenerife ocean island basalts were selected as a compositional analog because they have been previously compared to Gale rocks [*Stolper et al.*, 2013] , they have compositions similar to those rocks in the uncertain category, and because the compositions for ocean island basalts are less likely to be complicated by continental surface processes [*Sarbas and Nohl*, 2008]. Naturally, the magmatic composition on Mars is not exactly the same as the magma composition in Tenerife (e.g. Fe is higher in martian magmas, as shown in Figure 4.7b, and TiO_2 is lower in Martian magmas, shown in Figure 4.7g [*Stolper et al.*, 2013]), but the minerals formed during cooling and the shapes of the compositional curves would likely be similar if the compositional variation is directly related to magmatic evolution.

Observing the igneous evolution plots in Figure 4.7, it is apparent that the elemental trends in the Bradbury samples are quite linear in comparison with the igneous evolution trends. Linear trends are expected on element-element plots when two-component mixing is taking place, e.g. mixing two sources or physically adding/subtracting a mineral, but elemental trends during igneous evolution of a magma typically show multiple slopes because the ratios of elements being incorporated into solid minerals change during cooling

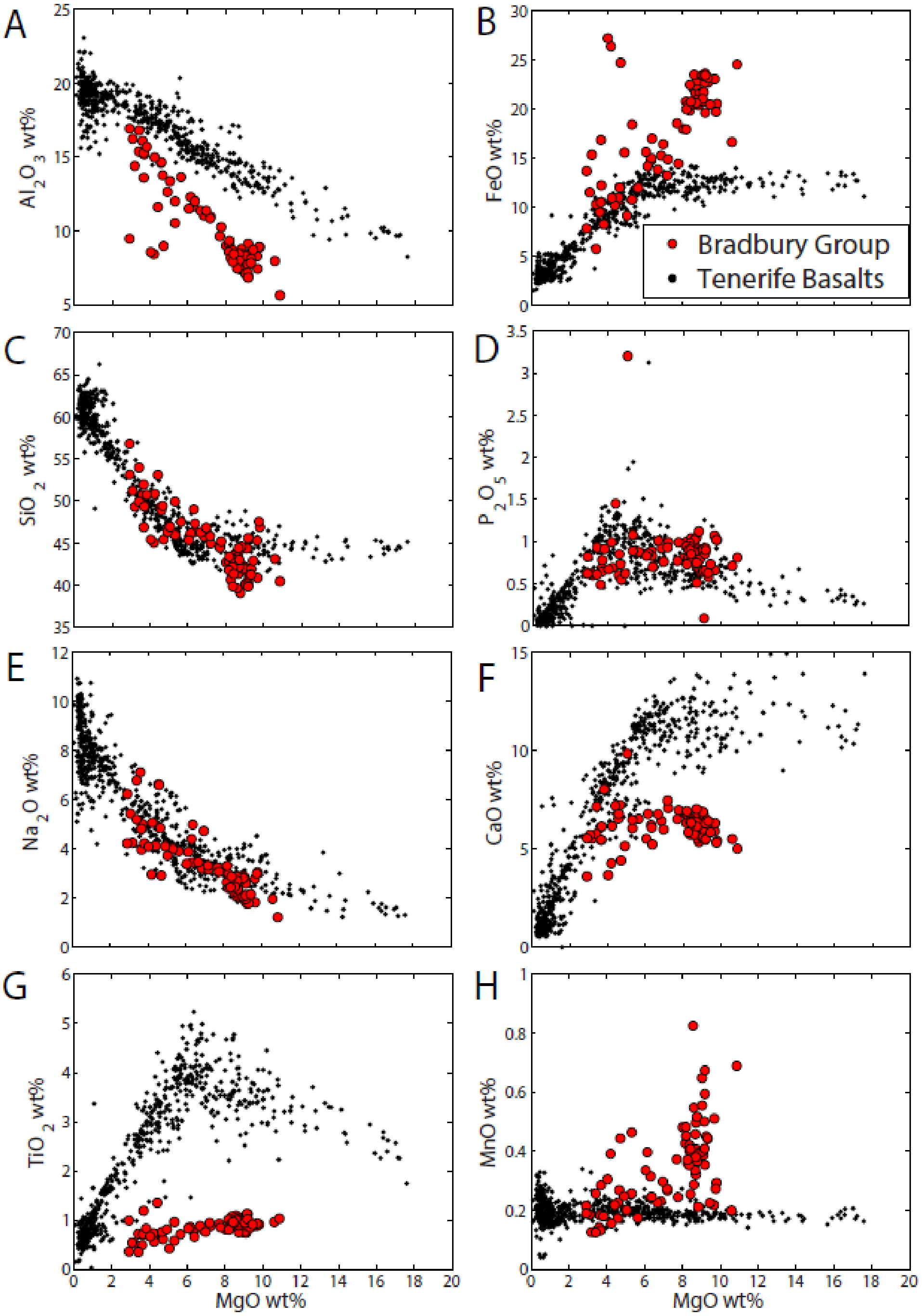

Figure 4.7 MgO Plots Comparing Bradbury Group and Tenerife Ocean Island Basalt Compositions

Element-MgO plots comparing Bradbury group compositional data in red (excludes diagenetic and Murray samples) with Tenerife Ocean Island Basalt compositional data in black. MgO wt% is proportional to magmatic evolution in igneous systems, so for Tenerife basalts, high-MgO samples are primitive and low MgO samples are from more evolved magmas.

as different minerals are formed. So linear trends would be unexpected from igneous evolution processes alone.

The Al_2O_3 vs MgO plot in Figure 4.7a is notable because the Tenerife data has the highest slope in Al_2O_3 vs MgO of any of the catalogued ocean island basalt complexes [*Sarbas and Nohl*, 2008] and the slope of the Bradbury trend is significantly steeper. This phenomenon is also present in the MnO vs MgO plot (Figure 4.7h); in magmatic systems, MnO is incorporated into minerals at a near-constant rate, but there is a significant slope between MnO and MgO in the Bradbury group samples, indicating that most of the variation is due to some other phenomenon. These unexpectedly steep slopes make it unlikely that the Bradbury elemental trends are defined by changes in the composition of igneous detritus due to magmatic evolution of the source rocks in the watershed. This does not rule out some igneous evolution for rocks in the watershed of the northern crater wall and rim, but these basaltic provenance shifts must fit within the observed elemental trends, and are unlikely to define them. This also cannot rule out the presence of non-genetically-related, cross-cutting, igneous associations.

4.4.6 Modeling APXS Mineralogy

Typically, terrestrial rock samples are characterized by a combination of their mineralogy and bulk chemistry, but due to sampling limitations with the rover (in Aeolus Palus, we have bulk compositions of 73 distinct in-situ rocks using APXS and the mineralogy of only 3 samples using the CheMin X-Ray Diffraction instrument), bulk chemistry is the only available information for the majority of these samples. Mineralogy can only be derived from chemistry if a number of assumptions are made, both with respect to the number of minerals included and the specific mineral compositions, e.g. the Fo number for olivine. The most typical of these would be to assume the rock is igneous, and that all minerals in the rock were formed in thermodynamic equilibrium, which would allow a normative mineralogy calculation of the mineral components. The Aeolus Palus rocks are sedimentary, and therefore do not fit those assumptions— instead, they likely include detritus derived from a range of basaltic sources that is sorted during transport, and may include cement compositions precipitated under different aqueous geochemical regimes. However, as shown in Figure 4.3, the bulk chemistry of the Aeolus Palus samples appears consistent with only cation-conservative weathering of basalt, so if that is correct, the compositions could potentially be related to primary igneous minerals.

4.6.1 Methods

In order to estimate the mineralogy of the Bradbury rock compositions and test the assumption of minimal open-system chemical weathering for those samples that do not show visible evidence of diagenetic overprinting, we use a Monte-Carlo based mass-balance model to test whether the rock compositions as determined by APXS are consistent with a mixture of primary igneous minerals whose compositions are, in turn, constrained by the compositions of phases in martian meteorites [e.g. *Papike et al.*, 2009; *Gross et al.*, 2011; *Santos et al.*, 2015; *Wittmann et al.*, 2015] and by the analysis of CheMin data on three Gale Crater samples [*Vaniman et al.*, 2014; *Morrison et al.*, 2015; *Treiman et al.*, 2015]. The minerals included in the calculations are: olivine, high- and low-Ca pyroxene, plagioclase, K-feldspar, apatite, ilmenite, chromite, iron oxides, and silica and the mass balance calculation attempts to find the best set of phase proportions in a least-squares sense that minimizes deviations between the calculated bulk composition and the measured bulk composition for the following oxides: SiO_2, TiO_2, Al_2O_3, Cr_2O_3, FeO, MnO, MgO, CaO, Na_2O, K_2O, P_2O_5, and NiO. While mass balance calculations are widely used in petrology [e.g. *Bryan et al.*, 1969; *Reid et al.*, 1973; *Walter et al.*, 1995], their application to the mixing problem discussed here is complicated by the fact that we have very limited information on the compositions of the major phases [*Vaniman et al.*, 2014; *Morrison et al.*, 2015; *Treiman et al.*, 2015]. However, using the compositions of mineral phases in martian meteorites and mineral stoichiometric constraints [see *Baker and Beckett*, 1999], we can construct, using random numbers, a population of stoichiometric olivines, pyroxenes, plagioclases, etc., whose compositions are consistent with those of martian meteorites, and, pulling phase compositions from these populations, run a very large number of mass balance calculations for each sample. In constructing these phase compositions, cation abundances in the olivines (Cr, Mn, Ca, and Ni) and pyroxenes (Ti, Al, Cr, Mn, Ca, Na, and Ni) were related to Mg# [Mg/(Mg + Fe), molar] variations in each phase and the bounds on Mg# of olivine and pyroxene and on molar K/(K + Na) of the alkali feldspar (which defines its composition) were constrained by CheMin results; bounds on molar Ca/(Ca + Na) values in plagioclase were based on data from martian meteorites and CheMin. It is important to note that although each individual mass balance calculation is over-determined (i.e., there are more equations than unknowns), the Mg# bounds on the olivine and pyroxenes are relatively loose and bulk FeO and MgO exert the largest constraints on the calculated proportions of mafic phases; hence, the individual weight fractions of these three phases are not as well constrained as their sum. We also note that the alkaline nature of many of the rocks at Gale Crater [e.g. *Stolper et al.*, 2013; *Schmidt et al.*, 2014; *Sautter et al.*, 2015] suggests that the pyroxenes in these rocks may differ from those found in martian meteorites (pyroxenes in terrestrial alkaline rocks tend to be richer in Ti, Al, and Na compared to pyroxenes in tholeiites). However, as we show below, the majority of the mass balance calculations yielded extremely small residuals, indicating that martian meteorite phase compositions can successfully be used to mass balance the compositions of Gale Crater sedimentary rocks.

In the calculations presented here, 200,000 weighted mass-balance runs were done for each sample—the best-fit calculation for any sample was that run with the lowest χ^2 value. Each best-fit calculation for a given sample was only deemed statistically acceptable if the *Q*-value [e.g. *Press et al.*, 1992] for that run was ≥ 0.05 (i.e., acceptable at the 95% confidence level). Note that the low-Ca pyroxene in our calculations was pigeonite. Based on Rietveld refinements of CheMin data [*Vaniman et al.*, 2014; *Morrison et al.*, 2015; *Treiman et al.*, 2015], pigeonite appears to be substantially more abundant than orthopyroxene in Gale Crater rocks and including three pyroxenes in the mass balance calculations leads to a linear degeneracy. Nevertheless, even with only two pyroxenes, some mass balance calculations returned negative mass fractions of olivine and/or pyroxene; after every individual calculation in a set of 200,000, any negative coefficients were set to zero and the mass balance calculation was repeated using the same phase compositions. As noted above, bulk APXS compositions were renomalized on a S- and Cl-free basis. Although this may introduce a systematic bias (we discussed above why we think that such a bias, if it exists, would not be large), initial calculations that included anhydrite and halite resulted in best-fit plagioclase compositions that tended to be extremely albitic, i.e., with molar Ca/(Ca+Na) ratios of 0.1 to 0.2—substantially more sodic than plagioclase compositions estimated by CheMin [*Vaniman et al.*, 2014; *Morrison et al.*, 2015; *Treiman et al.*, 2015]. This suggests that although CaO and SO_3 are positively correlated in the APXS data, some fraction of the sulfur is incorporated in non-calcium bearing phases. The fact that we have only mass-balanced rocks that show no obvious diagenetic features (and have SO_3 contents rocks <8.4 wt%) limits the leverage that the renormalization exerts on the remaining oxides in these bulk compositions. Details of the mineral calculation schemes and the mass balance program will be presented in a subsequent paper.

Although a large majority of the APXS sedimentary rock compositions can be modeled using only the compositions of igneous minerals that are consistent with those found in martian samples, this does not mean that these sedimentary rocks are necessarily composed of just these phases. Indeed, based on the results of the small number of CheMin XRD analyses, there may well be clay minerals and one or more difficult-to-characterize amorphous phases in all of the Gale Crater sedimentary rocks [*Vaniman et al.*, 2014; *Treiman et al.*, 2015]. It does suggest, however, that the compositions of the materials that accumulated to produce these sedimentary rocks can be described as mixtures of igneous minerals and that a substantial loss of cations following deposition has probably not occurred. Calculations using bulk compositions of progressively more severely weathered basaltic rocks [*Chesworth et al.*, 1981; *Nesbitt and Wilson*, 1992; *Sheldon*, 2003] show that mass balance fits generally fail at the 95% confidence level once the Chemical Index of Alteration (discussed in section 4.5.1) exceeds ~50–55. Furthermore, if a significant number of the observed samples can be mass balanced using a relatively narrow range of olivine, pyroxene, and feldspar compositions, then that would suggest that the sources of these sedimentary rocks consisted of igneous rocks with a fairly limited range of compositions and that only physical weathering and sorting operated to produce the observed elemental trends. An important caveat on this last point is that the phase compositions used in the mass balance calculations should be thought of as average compositions, i.e., a relatively wide range of plagioclase compositions could actually be present in the sedimentary rock but the best-fit plagioclase from the mass balance calculation would be one that closely matched the average composition of all of the plagioclase grains.

4.6.2 Results

Seventy-four out of eighty-three non-diagenetic rock analyses, or about 90% of the non-diagenetic Bradbury group analyses, were successfully modeled as sums of primary igneous minerals with a χ^2 confidence interval of 95%. This is consistent with the assumption of cation-conservative weathering (Figure 4.3) [*McLennan et al.*, 2014], and further confirms those results by showing that all of the elements that are measured with APXS can be reasonably arranged in primary igneous compositions within most of these rocks, with no need for any cation loss to explain the compositions. This does not preclude the formation of secondary minerals—indeed, we know that secondary minerals are included—but the compositions are consistent with cation-conservative authigenesis rather than open-system weathering.

Of the nine Bradbury group analyses that could not be modeled at 95% confidence, four were consistent within the 80% confidence interval and had one element that could not quite be incorporated into the primary basaltic minerals, including Jake_Matijevic2 (sol 47, uncertain, excess Na_2O), Stirling (sol 707, sandstone, excess Na_2O), JumJum (sol 550, conglomerate, excess Na_2O), and Windjana DRT (sol 612, fine sandstone, excess MnO). The other five were all float rocks that were categorized in the "uncertain" category, and all five cases had excess Na_2O. These include two analyses on Jake_Matijevic1 (sols 46 and 47, excess SiO_2 and Na_2O), Oscar (sol 516, excess Na_2O and Al_2O_3), Morehouse (sol 503, excess Na_2O and SiO_2), and Secure (sol 560, excess Na_2O and Al_2O_3).

Only 26 of 38 of the diagenetic and 16 of 27 Murray mudstone samples had χ^2 values indicating fit at 95% confidence, indicating that the composition of these subgroups has been affected by chemical weathering, chemical addition, and/or chemical alteration. Diagenetic samples were categorized as such because they contain textural features showing preferential cementation, so it is interesting that ~70% of them can still be modeled with primary igneous components, however it is important to note that this model is done on a volatile-free basis, so, e.g., excess $CaSO_4$ cement or vein-fill may not be captured by this model. The Murray mudstone samples could only be modeled with a silica mineral component, and frequently had excess Al_2O_3, Na_2O, and/or P_2O_5 compared to the closest primary basaltic mineral composition. This is consistent with previously published reports showing that the Murray mudstone sediments have been more affected by some form of chemical weathering [*McLennan et al.*, 2015].

The mineralogical models for the Bradbury group APXS compositions allow mineral-based comparisons between the different textural classes. A bar chart showing the median modeled mineralogy of each textural class is show in Figure 4.8a. This chart is consistent with the geochemical models in Figure 4.6, indicating that the mineralogy, like elemental composition, varies with grain size in for the Bradbury group, and that one of the primary differences with grain size is the weight percent of plagioclase minerals (Figure 4.8b) compared with the weight percent of mafic minerals (Figure 4.8c). Plagioclase content is quite high in possible igneous and uncertain float rocks, intermediate in conglomerates, and lower in sandstone, fine sandstone, and Sheepbed mudstone targets. Mafic mineral content (olivine, high- and low-Ca pyroxene, chromite, ilmenite, and iron oxides) is higher in the three finest grained textural classes.

Other differences between textural classes are irregular. Based on the range of mineral compositions that led to acceptable fits for each composition, the relative amounts of olivine, high-Ca, and low-Ca pyroxene are not well constrained, but the sum of these three components is well constrained, so it may be more accurate to consider the sum of mafic components (Figure 4.8c) rather than the relative proportions of each as shown in Figure 4.8a. From Figure 4.6h, it is evident that calcium content does not trend with grain size and instead has a relatively consistent value in all samples (like sulfur, Figure 4.6i). Calcium sulfate veins are known to pervasively transect every unit *Curiosity* has explored, including the Bradbury group [*Nachon et al.*, 2014], the Murray formation [*Grotzinger et al.*, 2015; *Kah et al.*, 2015; *Kroynak et al.*, 2015] and Stimson formation [*Newsom et al.*, 2016], so it is evident that some calcium was transported in late-stage diagenetic fluids. If

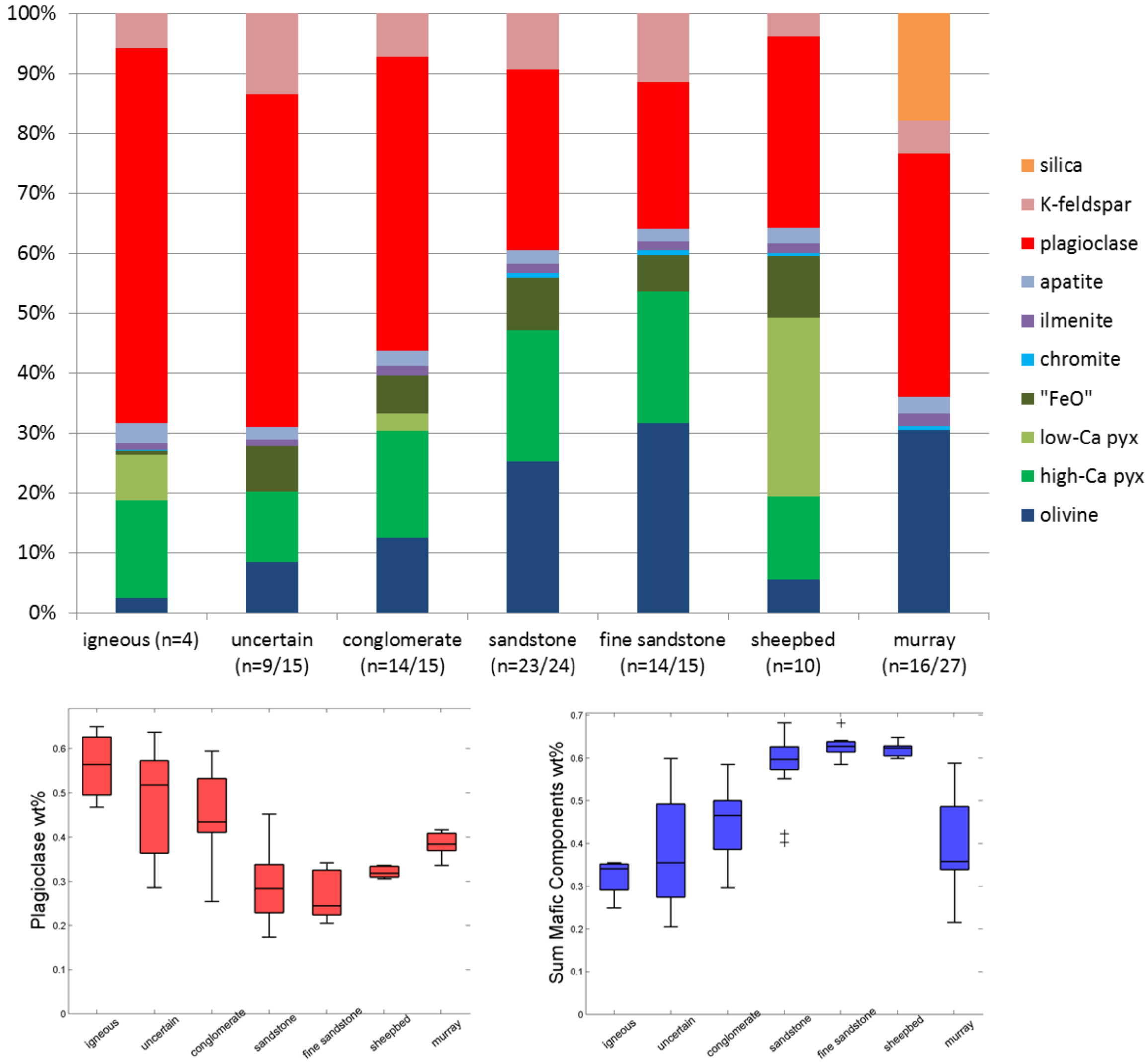

Figure 4.8 Modeled Mineralogy for Each Textural Class in Bradbury Group
Diagrams showing the modeled mineralogy for each of the Bradbury group textural categories and Murray mudstone. Part (a) shows median weight percent of each mineral for each textural class. Parts (b) and (c) are boxplots showing the range of plagioclase and mafic components within the textural classes. Part (c) sum of mafic components is the sum of olivine, pyroxenes, “FeO”, chromite, and ilmenite.

calcium has been redistributed by diagenetic fluids, then the relative proportioning of Ca between high and low calcium pyroxene could be further compromised.

4.5 Discussion

Any hypothesis for explaining observed APXS compositional variations between Bradbury Group samples must address variation from chemical weathering, source rock input, transport processes, and diagenetic cements. This study has shown that a meaningful hypothesis must also be constrained by these observations:

(1) Compositional variation between non-diagenetic Bradbury samples is nearly linear on element-element plots and is strongly correlated with grain size/texture of the sedimentary rock observed (Figures 4.6 and 4.7).

(2) This compositional variation is consistent with the enrichment (in coarser-grained samples and float rocks) or depletion (in fine-grained rocks) of plagioclase minerals (Figures 4.6 and 4.8).

(3) Bradbury rocks have extremely low Chemical Index of Alteration values (Figure 4.3) and 90% of the sample compositions can be modeled using only primary basaltic minerals (Figure 4.8).

(4) Potassium does not follow expected trends for plagioclase enrichment, and is instead strongly enriched in a specific stratigraphic position (Figure 4.5).

4.5.1 Chemical Weathering

Chemical weathering involves the decomposition of rocks by chemical reactions that break apart the constituent minerals, typically forming new secondary minerals. This process can occur in an open system or a closed system. In an open system, some chemical products from mineral and rock breakdown may be removed from the system, typically by dissolution and fluid migration, causing changes in the bulk chemistry of the rock sample. In a closed system, chemical breakdown of the rocks occurs but the chemical constituents remain, forming secondary minerals but not changing the bulk chemistry of the rock. The APXS instrument onboard *Curiosity* only measures bulk composition of rocks, and therefore is only sensitive to chemical weathering in an open system; the formation of secondary minerals in a closed system does not affect the bulk compositions and is not distinguishable with the APXS instrument alone.

In this study, three methods are used to assess the degree of open-system chemical weathering; Chemical Index of Alteration (CIA) values, trends on the mafic ternary diagram, and mineralogical modeling to see if sample compositions deviate from primary basaltic mineral components. All three methods, described below, indicate that open-system chemical weathering in the Bradbury Group rocks was negligible.

Open-system chemical weathering in ancient rocks on Earth and Mars is frequently quantified using the Chemical Index of Alteration (CIA), a molar ratio of Al_2O_3 over the sum of K_2O, CaO, Na_2O and Al_2O_3 that serves as a proxy for the weathering of feldspars and Ca-bearing pyroxene (Figure 4.3) [*Nesbitt and Young*, 1982; 1984; *Nesbitt*, 2003; *McLennan et al.*, 2014]. On Earth, CaO* is corrected to only include calcium in silicate minerals; since this is not well-constrained on Mars, we do not apply a correction here, so reported CIA values are lower than they would be if corrected. Fresh mafic basalts have CIA values of ~30-45; values above ~45 may indicate some exposure to weathering, and values above ~50-55 are evidence for some history of open-system chemical weathering [*McLennan et al.*, 2014]. Since the rocks in Aeolus Palus are basaltic, and the first components to chemically weather are likely olivine and any basaltic glass, it is important to also look for weathering trends on the mafic ternary diagram A-CNK-FM, which also incorporates FeO_T and MgO, so that trends from weathering of olivine would also appear along the direction of the red arrow in Figure 4.3.

The lack of open-system chemical weathering in the Yellowknife Bay formation, the lowest part of the Bradbury group, was first established by detailed measurements of the Sheepbed mudstone. Compositional data for this unit are very similar to average Mars crust [*Taylor and McLennan*, 2009] and have very low CIA values (up to 37.5), indicating that there was minimal or no open-system chemical weathering of detrital basalt [*McLennan et al.*, 2014]. However, CheMin x-ray diffraction data revealed that this unit is composed of 20-30% phyllosilicates, which are interpreted to be authigenic clays formed within the ancient lake that deposited the mudstone [*Grotzinger et al.*, 2014; *Vaniman et al.*, 2014]. These observations indicate that even where significant amounts of water were present, authigenesis occurred, and secondary minerals were formed, there is still a lack of evidence for open-system chemical weathering. The lack of evidence for chemical weathering was attributed to a cold climate by McLennan et al. [2014].

Observations of coarser-grained Bradbury sediments also show a lack of evidence for open-system chemical weathering. Of 113 rock targets, 10 have CIA values above 40, and all are below 45. No weathering trends appear on the mafic ternary diagram (Figure 4.3). Additionally, 90% of all of the non-diagenetic rock compositions observed, including float rocks, can be modeled as a mixture of primary basaltic mineral compositions with a 95% confidence interval (Figure 4.8). There is remarkably little evidence for any extensive chemical alteration or cation loss from these sediments. Note that this trend does not continue into Mount Sharp sediments, which show a more complex weathering history, resulting in CIA values of 37-53, with only 4 samples having CIA < 40, and 40% of the samples cannot be modeled by primary basaltic minerals + silica.

Overall, there is a lack of evidence for chemical weathering of Bradbury group sedimentary rocks, indicating that none of these samples has experienced a significant weathering history. We support the original interpretation of this trend by McLennan et al. [2014] who invoked a cold climate at the site of weathering along the crater rim. The climate was warm enough to allow liquid water to be stable and support overland flows [*Williams et al.*, 2013; *Grotzinger et al.*, 2014; *Szabo et al.*, 2015] and also pool as long lived lakes [*Grotzinger et al.*, 2014; *Grotzinger et al.*, 2015]; however, it was cool enough to severely limit the effects of chemical weathering.

4.5.2 Mechanisms for Potassium Variation

Perhaps the most distinctive elemental trend in the measured suite of Bradbury samples – potassium variation – is not correlated with grain size but is instead strongly correlated with bedrock and float measurements at a certain stratigraphic interval (Figure 4.5). As with other elements, potassium could be enriched by: contribution of a distinctive source region enriched in potassium (as suggested by [*Treiman et al.*, 2015]), hydrodynamic sorting of potassic minerals during transport, or post-depositional chemical alteration such as potassium metasomatism. Treiman et al. [2015] discuss the source of the potassium in detail; we summarize key relevant arguments here.

Increased potassium due to hydrodynamic sorting of potassium during transport or potassium metasomatism within the sediments in the Kimberley outcrop is inconsistent with the APXS and CheMin observations. Potassium does not trend with grain size, and the presence of easily-altered olivine, pyroxene, and other primary igneous minerals in the drilled ("Windjana") sample and the lack of any other evidence for open-system chemical alteration are inconsistent with significant chemical weathering. Furthermore, potassium metasomatism is unlikely due to the lack of accompanying metamorphic or hydrothermal alteration minerals [*Fedo et al.*, 1995; *Treiman et al.*, 2015], so the potassium must be concentrated by another mechanism.

The trend in potassium with stratigraphic position (Figure 4.5) makes it clear that potassium is highly concentrated in a specific sedimentary interval, which is likely correlated with detrital input from a high-potassium source rock. There was a drilled sample at the site of the high potassium, "Windjana", so the CheMin X-Ray Diffraction (XRD) data allows a more detailed analysis of the potassium source [*Treiman et al.*, 2015]. To first order, Windjana XRD results showed that the sample contains significant amounts of pigeonite (11%) and sanidine (21%), which cannot form in the same igneous protolith, so based on mineralogy alone, multiple igneous protoliths must have contributed to this sample.

Investigation of the crystal chemistry of the mineral components based on the XRD analysis reveals further evidence that the potassium source is a distinctive detrital component. Treiman et al. [2015] show that the sanidine is ~Or95, with extremely high K_2O/Na_2O. This is a surprising finding in Aeolus Palus, where the rest of the plagioclase is andesine (~An30-50) [*Vaniman et al.*, 2014; *Morrison et al.*, 2015]. Treiman et al. also analyze the crystal chemistry of the major basaltic components, and show that the olivine, augite, and pigeonite are consistent with formation in the same basaltic protolith (within error)—although this cannot be the same protolith as the sanidine. The implication is that the majority of the components in the sample are correlated, and from a basaltic source that is likely related to the rest of Aeolus Palus, and Or95 sanidine is the only significant tracer mineral contributed by a distinctive igneous provenance, which Treiman et al. [2015] interpret to be a trachyte with >40% sanidine. For further details and petrologic implications, we refer the reader to the Treiman et al. [2015] study.

The protolith with the sanidine mineral component was only contributing significant sediment at certain times during the filling of the Gale basin, which caused certain stratigraphic intervals, such as the Kimberley formation, to be strongly enriched in sediment from that source region, whereas other intervals were not affected (Figure 4.5). Without sufficiently high resolution chemostratigraphic data collected across this part of the Bradbury group, it is not clear whether or not hydrodynamic sorting had any effect on potassium distribution within the Kimberley formation.

4.5.3 Major Influences on Composition of Bradbury Group

4.5.3.1 Influence of Source Rocks

The provenance of sedimentary rocks describes the collection of all rock types that are weathered and eroded to produce sediment that is transported and deposited in a sedimentary basin. Sedimentary provenance studies use the chemical and mineralogical properties of sedimentary rocks to determine the original source rock composition and the effects of weathering processes that caused the source rock to break down into sediment [*McLennan et al.*, 2003; *Weltje and von Eynatten*, 2004]. For fluvial sediments, source rocks are typically the local rock units upstream in the watershed that are exposed to surface weathering [*Nesbitt et al.*, 1996]. Eolian, volcaniclastic, and lacustrine sediment sources are frequently more widespread because they can integrate rock fragments transported longer distances by wind and sediments from all catchments around the basin. In terrestrial cases, the majority of sediment is derived from pre-existing sediment (i.e. sediment recycling), which obscures identification of original igneous/metamorphic sources. The role of sediment recycling is not well constrained for Mars, but it is not believed to play as significant a role [*McLennan and Grotzinger*, 2008a].

Provenance studies that correlate sedimentary rocks to their original source rocks typically depend on bulk composition and petrology of the rocks [*Russell*, 1937; *Young and Nesbitt*, 1999; *Vezzoli et al.*, 2004], detrital heavy minerals [*Frihy*, 1994; *Cawood et* *al.*, 2003; *Fedo et al.*, 2003], or radiogenic isotope fractionations within minerals [*Vervott et al.*, 1999; *Kuhlmann et al.*, 2004; *Hodges*, 2005] to describe the sediment provenance. The history and background for each of these approaches is summarized in [*Weltje and von Eynatten*, 2004]. While provenance effects can be obscured by sorting of grains during transport and later diagenetic processes, the initial relative sizes of different mineral grains are defined by the source rocks, so the direction of sorting trends depends heavily on provenance [*Ohta*, 2004; *Fedo et al.*, 2015].

The sedimentary materials of the Bradbury group were likely sourced from the Noachian terrain above the northern rim of the crater based on sediment transport directions and local geomorphic and stratigraphic features [*Palucis et al.*, 2014; *Grotzinger et al.*, 2015; *Szabo et al.*, 2015]. Rocks within this region are known from orbital hyperspectral imagery to contain olivine [*Ehlmann and Buz*, 2015], but otherwise there are relatively few constraints on the petrology of the watershed, so we do not know *a-priori* what provenance signals may be expressed in the detritus which accumulated as the Bradbury group. However, from the perspective of the bulk Bradbury composition we gain some insight into the overall nature of the sediment source; the compositions tend to be similar to average Mars crustal basalt, but somewhat more alkaline, comparable to alkaline ocean island basalts on Earth [*Stolper et al.*, 2013].

Direct information about the Gale provenance can also be based on analysis of large grains of definitively igneous rocks. While *Curiosity* has observed several rocks with potentially igneous textures (and observed 4 of these with APXS), the most definitive igneous rock texture was observed with the Mastcam and ChemCam instruments at the Harrison target, in a large clast within a conglomerate (“Harrison” target), on sol 514 [*Sautter et al.*, 2015; *Mangold et al.*, 2016]. Harrison is composed of ~50% light-toned plagioclase phenocrysts set in a dark fine-grained matrix [*Sautter et al.*, 2015]; if Harrison is representative of the source rocks contributing to the Bradbury group, the sediment may also contain larger clasts of plagioclase and finer particles of mafic minerals. Texturally, several of the other clasts in conglomerates and possible igneous samples observed by APXS also appear to show large felsic grains intermingled with a dark mafic substrate. Compositionally, however, the clasts observed with APXS are not necessarily igneous compositions because they may have been affected by sedimentary processes, including effects from cementation and dust cover.

The Murray mudstone, part of the Mount Sharp group, has at least a partially different provenance than the Bradbury group—the mudstone sediments have a composition that is distinct from all grain size classes in the Bradbury group. As a mudstone, like the Sheepbed mudstone, the Murray mudstone may incorporate sediment from multiple watersheds and from authigenesis within the lake itself, so the Bradbury provenance could be one of multiple contributing sources for the Murray mudstone. The elevated CIA values of the Murray suggest input from some chemically weathered source regions, but the presence of unaffected olivine and pyroxene minerals in the Murray formation suggest that the lake environment was not itself conducive to extensive mineral alteration (Figures 4.4 and 4.8). Some Murray sediments could be modeled as mixtures of primary basaltic minerals if silica was included, indicating that silica authigenesis or nearly-pure silica input by some other mechanism could have played a role in creating the Murray compositions (Figure 4.8). Other Murray sediments showed excess Al_2O_3, Na_2O, and/or P_2O_5, which are likely components contributed by a chemically weathered source region. Further investigation of the Murray formation is required to untangle the more complex factors involved in mudstone formation, but it is sufficient for this study to recognize that the Murray unit has a distinct provenance from the Bradbury group, and should be treated independently.

4.5.3.2 Influence of Sorting during Transport

Sorting of sediment by density and grain size has long been recognized as an important process in the formation of sedimentary rocks, especially due to the economic importance of heavy mineral deposits [*Mackie*, 1923; citations in *Weltje and von Eynatten*, 2004]. Early researchers noticed that within a natural sand sample, heavy/dense minerals are concentrated in finer grain sizes and lighter minerals are found in coarser grain sizes [*Rubey*, 1933; *Slingerland*, 1977]. Rubey modeled this phenomenon using Stokes' law to describe the settling velocity (which defines particle retention in the suspended load in a flow) of particles with differing grain sizes and densities, and showed that, for example, a spherical magnetite grain that is 0.63 mm in diameter would be suspended in the same flow as a spherical quartz grain 1.0 mm in diameter, making those two grains "hydrodynamically equivalent" [*Rubey*, 1933; *Slingerland*, 1977]. While shape and erodibility of minerals can also play a role in mineral sorting by grain size, modern surveys of different sediments show that Stokes' law (and similar impact laws for different flow types) do quite well at describing the grain sizes of different minerals in a given mixed sediment sample based on this principle of hydrodynamic equivalence [*Whitmore et al.*, 2004; *Garzanti et al.*, 2008].

Stokes' law and the principle of hydrodynamic equivalence explain the grain size fractions of specific minerals within a sample, but these cannot explain overall compositional trends between samples; these trends must instead be defined by the availability of grains of a given hydrodynamic equivalence within the fluvial system. That is, the overall composition is ultimately provenance dependent; if a portion of the river is accreting sediment hydrodynamically physical equivalent to 1.0 mm diameter quartz grains or 0.63 mm magnetite grains, the relative abundance of magnetite and quartz depends on the availability of those two minerals in those specific size fractions. This is dependent on the sediment provenance, the combination of abrasion and chemical weathering of the source rock before and during transport, slope and distance of transport, local flow dynamics that tend to concentrate heavy minerals in fine-grained lag deposits, introduction of additional sources, etc, which act as a system to make downstream trends in composition frequently inconsistent between locations [*Johnsson and Basu*, 1993]. While each system is unique, some general trends may be understood for each of these factors.

The provenance of the Bradbury group is basaltic, and at least some of the source rocks appear to have plagioclase phenocrysts in a mafic groundmass. The evidence described in this study indicates that chemical weathering does not play a major role here. Based on an analysis of grain roundness, Szabó et al. [2015] showed that the Gale sediments (at least those in conglomerates) have likely traveled on the order of ~50 km from their source, so Bradbury group sediments have traveled short distances relative to many sandstones on Earth. Basaltic sediment that is fluvially and not chemically weathered is difficult to find on Earth, but a few partial analogs are relevant.

The nature of sediments from similar basaltic sediment provenances are described in Fedo et al. [2015] and Nesbitt and Young [1996]. Fedo et al. crushed unweathered basalts from Kilauea, HI (porphyritic) and Cima volcanic field, CA (aphanitic) with a rock crusher to imitate impact-induced rock breakdown. They found that olivine and associated trace elements (Cr, Zn, Ni) were concentrated in fine grained fractions, while plagioclase was enriched in coarser grain fractions, and that these compositional differences between sieved grain size classes were greater for porphyritic basalt. They point out that this compositional fractionation would be enhanced during transport sorting due to significant differences in grain size and some differences in specific gravity [*Fedo et al.*, 2015]. Nesbitt and Young [1996] studied the bulk compositions of different grain size sediments in a short (<5 km) glacio-fluvial system in Guys Bight Basin, where the bedrock is predominantly metamorphic gneiss composed of feldspars, quartz, biotite, and hornblende. The bedrock is comminuted by glacial processes and then sorted in a fluvial system, with low CIA values indicating minimal chemical weathering. Biotite and hornblende (and therefore FeO_T, TiO_2, and MgO) are concentrated in the muds and fine sands, whereas quartz and feldspar are relatively more abundant in medium and coarse sands, again following Bradbury group trends with mafic mineral enrichments in finer grains and felsic mineral enrichments in coarser grains [*Nesbitt and Young*, 1996].

The relative importance of the initial grain sizes of mineral grains (provenance) and the abrasion and breakdown of grains during transport in a fluvial system has been debated for Earth systems [e.g. *Ferguson et al.*, 1996], and if differential abrasion played a significant role in Bradbury sediment transport dynamics it might have modified or enhanced compositional grain size signals related to provenance. Indeed, analysis of the particle shapes in Bradbury conglomerates indicate ~10-20% mass loss by physical abrasion [*Szabo et al.*, 2015]. Physical stress tends to increase the number of monomineralic grains, thereby enhancing compositional variation with grain size if the original source rock were porphyritic [*Slatt and Eyles*, 1981]. So, to first-order, physical abrasion processes may have enhanced the compositional differences in Bradbury sediment grain populations.

4.5.3.3 Influence of Diagenesis

The Bradbury group sedimentary rocks have clearly been cemented and lithified. The Sheepbed mudstone seems to have been impermeable to sulfate-precipitating fluids that circulated through fractures, but not the fractured bedrock, during late stages of diagenesis [*McLennan et al.*, 2014; *Vaniman et al.*, 2014]. There is evidence for burial of the Bradbury and Mount Sharp groups [*Schieber et al.*, 2013; *Grotzinger et al.*, 2015], so compaction likely played a role in lithification, but further cementation is also required. The timing is constrained by late-stage calcium-sulfate-filled fractures, whose fluids did not penetrate into the surrounding rock, so the rocks must have been well-cemented prior to that fluid event [*Nachon et al.*, 2014].

The lack of open-system weathering makes it difficult to determine the composition of the cement, and it is possible that the cementing agent is distinct in different regions. There are a limited number of float rocks observed by ChemCam [*Blaney et al.*, 2014] and some observed by APXS, including float rocks Et Then and Secure [*Schmidt et al.*, 2014], that show persuasive evidence for iron oxide cements—each have >24 wt% FeO_T—but these are outliers compared to other targets. The majority of targets have compositions that are consistent with primary basaltic minerals that lack evidence for open-system chemical weathering. Despite this, CheMin XRD analyses has shown that ~30% of each drilled sample is amorphous [*Dehouck et al.*, 2014; *Vaniman et al.*, 2014; *Treiman et al.*, 2015]. The amorphous component and the presence of significant amounts of phyllosilicates in the Sheepbed member together indicate closed-system chemical weathering, which would allow formation of phyllosilicates, and possible authigenetic iron oxides or salts that formed without altering the bulk composition at the scale of APXS. Compaction of phyllosilicates would help drive lithification, and salts or unstable minerals could help cement the rocks, but also could become amorphous due to desiccation and thermal cycling in the harsh Mars climate, as described in [*Vaniman et al.*, 2004].

4.5.4 Mechanism for Plagioclase Variation

Based on the evidence presented in this study, the major elemental variations for Bradbury rocks parallel grain size fractions and are consistent with plagioclase enrichment in coarse grained rock units and plagioclase depletion, or mafic enrichment, in fine grained rock units (Figures 4.6 and 4.8). In the absence of evidence for open-system chemical weathering, this type of trend could relate to contributions from different source rocks and/or to mineral sorting during transport; here we investigate each of these options.

If contributions from multiple source rocks define these major trend lines, one of the source rocks must be felsic and coarse-grained, or more proximal, and another must be mafic and fine-grained, or more distal. If both petrologically-evolved felsic rocks and primitive basaltic rocks coexisted in the watershed, it would be most simple to assume that they were genetically related and both formed from the same basaltic source as magmas cooled along a liquid line of descent. If this were the case, then the endmembers of the compositional trends should correlate with magma compositions at the beginning and end of a liquid line of descent, and intermediate compositions from the liquid line of descent may be present as well. Instead, in Figure 4.7, the Bradbury group rocks show linear trends with MgO, a tracer for igneous evolution, instead of curved lines or any breaks in slope as are expected in an evolving magma, and in some cases (Figure 4.7a and 4.7h especially) the trends are steeper than would be expected from magmatic evolution alone. Furthermore, both the measured and modeled Mg#s for olivine and pyroxene minerals are consistent and do not trend with texture, so the variation between samples is related to the relative amounts of different minerals rather than the evolution of the compositions of the minerals themselves, as would be expected in an evolving magma. This implies that the compositional trends observed are not formed due to mixing of evolved and primitive magmas from the same liquid line of descent. Instead, these trends are consistent with mineral sorting from a relatively homogenous source region except for the influx of sanidine-rich material at the stratigraphic level of the Kimberley formation.

Linear trend lines showing preferential plagioclase enrichment in coarse grained materials and mafic enrichment in fine-grained materials are consistent with expected trends from communition and sorting during transport of a porphyritic basaltic source. Physical weathering of rocks breaks the rocks down into component mineral grains which, particularly in the case of porphyritic rocks, will concentrate olivine and heavy minerals in the finest grain size fraction, and retain lithic fragments and less dense felsic grains in the coarser grain size fraction. During transport, the finest grains remain in suspension and compositional sorting is enhanced because the feldspar grain sizes are so much larger than the mafic grain sizes that they are preferentially deposited upstream, in conglomerate facies, whereas the finer olivine and mafic grains remain in suspension until they are deposited downstream in fine-grained sandstones and lacustrine mudstones. This is consistent with the observation that the primary variations between samples are defined by their grain size and proportion of minerals, rather than the compositions of the minerals. Sorting of basaltic mineral grains during communition and transport is the most consistent explanation for the major compositional trend in Bradbury group compositional data.

Minor trends or deviations from the principal plagioclase enrichment trend in Bradbury rocks are within expected deviations for a natural environment. The scatter around the trend is likely related to dust cover, small-scale heterogeneities in the fluvial environment, and possibly some diagenetic cementation. For example, late-stage diagenetic calcium-sulfate veins are prevalent and cause the distribution of Ca and SO_3 to vary from expected trends, obscuring the original ratio of high-Ca and low-Ca pyroxene.

The Sheepbed member compositions do not form the end of the trendline, but tend to sit between the fine sandstone component of the Bradbury group and the Murray formation of the Mt. Sharp group. The Sheepbed member is also the only non-fluvial, lacustrine mudstone sampled in the Bradbury group, so it has a much higher chance of incorporating sediment input from eolian or distal volcanic sources, or other fluvial sources around the crater, in addition to capturing the finest particles in the suspended load, which frequently have a more mafic composition than deposited particles. Float rocks, especially those with obscured textural features, categorized here as uncertain, also cause some of the variations from the major compositional trends and make up all of the rocks that cannot be modeled using primary basaltic components. This is expected when incorporating float rocks; these clasts could have been transported unknown distances and were frequently selected along the traverse for analysis due to their unusual appearance. Indeed, it is more surprising how clearly the trends are visible even with float rocks and outliers incorporated.

Finally, the potassium content of Bradbury group rocks is not related to the mineral sorting trends, but is instead correlated to the presence of a distinctive minor source with a sanidine-rich composition. Mineralogical data at the Kimberley outcrop, with the highest concentration of potassium, show that the rock is still dominated by mafic minerals consistent with the main source for Bradbury group sediments, but the sanidine is separate and has an unusual characteristic high K_2O/Na_2O ratio, which is chemically inconsistent with the Bradbury provenance. The sanidine therefore is a mineralogic indicator of a distinctive protolith that contributes to at least one stratigraphic interval that is otherwise dominated by the main Bradbury group provenance.

4.6 Summary

The collection of compositional analyses on rocks of the Bradbury group in Gale Crater offers a unique dataset for sedimentary petrology because these rocks have experienced minimal cation-loss due to chemical weathering, the sedimentologic context as a fluvio-lacustrine system is generally understood, and a variety of textures and grain sizes were sampled. This dataset therefore enables us to back out information concerning the initial petrological and sedimentary processes that led to the deposition of these sediments. The principal geochemical trends for these samples reflect a concentration of plagioclase minerals in the coarsest grained samples, and a concentration of mafic minerals in the finer grained fraction. Investigation of the geochemical trends and Monte-Carlo modeling of the mineral compositions show that these trends are consistent with breakdown and segregation of plagioclase phenocrysts from a mafic groundmass during transport, and the geochemical diversity of the sediments does not require significant petrologic diversity in the sediment source region. The primary exception to this low petrologic diversity is a stratigraphic interval around the Kimberley outcrop, where high potassium sanidine must be contributed by a unique source rock that only periodically contributes sediment to the Gale Crater basin. The formation of the Bradbury group from a relatively homogeneous, unweathered basaltic provenance provides contrast and background for understanding of higher layers on Mount Sharp.

Chapter 5

Causes of Geochemical Diversity in Three Different Gale Crater Sedimentary Rock Formations

Key Points

- *Curiosity* obtained bulk composition and mineralogy for three rock formations
- Differences in geochemical variability are related to depositional environment
- Geochemical trends relate to transport, source rocks, authigenesis, and diagenesis

Abstract

Bulk compositions of sedimentary rocks are records of detrital grains from a source region, sorted by transport, and cemented. This study compiles and summarizes geochemical compositions, variability, and trends for samples in the fluvio-deltaic Bradbury group, lacustrine Murray formation, and eolian Stimson formation in Gale crater. The fluvio-deltaic Bradbury group has the most geochemical diversity due to significant mineral sorting during transport and the variety of grain sizes in measured samples, but the geochemical trends are centered around a typical basalt composition and the diversity is derived from transport rather than source. There is one distinctive source input for the Bradbury, which has high sanidine and a distinctive K_2O-rich chemical signature. The lacustrine Murray formation has intermediate geochemical diversity, which could be related to shifting between mafic and silicic volcanic source rocks the balance between clastic input and authigenic cement production in the lake water or pore fluids. The eolian Stimson formation has low geochemical diversity and a composition very similar to average Mars crust, reflecting the regional integration of compositions of source rocks by wind. Diagenetic processes in each of these formations serve to alter compositions relative to bedrock; fluid trends are identified and described. The geochemical characteristics of each of these Gale crater formations are strongly related to their depositional environments.

5.1 Introduction

Sedimentary rocks preserve the textural and geochemical record of ancient planetary surface processes. Understanding these records enables us to reconstruct the changing depositional environments and water chemistry over time, and allows better assessment of ancient habitable environments and climatic constraints. In Gale Crater, the *Curiosity* rover has observed three sedimentary rock formations deposited in distinct environments. From oldest to youngest, these are: the fluvio-deltaic Bradbury group; lacustrine Murray formation; and eolian Stimson formation. Based on depositional environment alone, each of these formations contains unique information about the origins and erosion of the rock units exposed on the walls of the crater and sediment transport processes that brought those rocks into the crater. We seek to understand the different source-to-sink processes that affect each of these three formations and apply these to better understand geochemical trends within each formation.

All sedimentary rocks experience diagenetic cementation, which may involve addition of cements from groundwater, and all rocks may experience chemical alteration after deposition. These post-depositional processes are known to occur on Mars and do affect the geochemistry of each of the formations being observed. These processes are considered relevant for all of the rocks observed and must be discussed, but the bulk geochemical composition of each formation is first related to the source rocks that contribute detrital material, and because these are distinct for each of the three units we first investigate these differences.

River systems integrate detrital sediment from all of the exposed rock types within a watershed. The diversity of rock types entering the river can be relatively homogeneous or quite variable, depending on the scale and diversity of the watershed, the consistency of spatial erosion patterns, and temporal changes as different rock units are exposed to erosion. Detrital signatures of distinctive rock units can cause the geochemistry of river sediments to change dramatically [*McLennan et al.*, 1990]. River sediments are also sorted by grain size and specific gravity during transport, differentiating the geochemistry of each sediment sample from its source rocks [*Nesbitt and Young*, 1996; *Nesbitt*, 2003; *Fedo et al.*, 2015]. These local erosion and transport processes can cause geochemistry of river sediments to be more variable, even in a simple watershed, than fine-grained mudstone counterparts [*Nesbitt*, 2003; *von Eynatten*, 2004; *Weltje*, 2004; *Weltje and von Eynatten*, 2004; *von Eynatten et al.*, 2012]. The Bradbury group fluvio-deltaic rocks in Gale crater show significant geochemical effects from sorting of mineral grains during transport, and a high-potassium stratigraphic interval that has been interpreted as input from a distinctive source rock within the watershed [*Treiman et al.*, 2015; *Siebach et al.*, in prep.].

Lacustrine sediments are the finest-grained fraction of all detrital sediments produced by rocks within all of the watersheds making up a sedimentary basin. These sediments are excellent regional compositional integrators; marine shales on Earth are commonly used to understand compositions at the scale of the continental crust [*Condie*, 1993; *Taylor and McLennan*, 1995; *McLennan*, 2001]. Due to the larger source area of exposed rock formations, and the ubiquitous fine grain size within lakes, lacustrine sediments are less likely to be affected by transport effects or distinctive source rocks within individual contributing watersheds [*McLennan et al.*, 1993]. However, the composition of a mudstone may be affected by direct eolian or volcanic inputs into the lake or mineral authigenesis from the lake water itself [*Schnurrenberger et al.*, 2003].

Eolian, or wind-blown, sediments are accumulated based on regional wind directions, and can integrate compositions over significant crustal regions. Loss of easily-eroded mineral components is common over large transport distances, so these may be under-represented in eolian deposits, while resistant minerals are over-represented (e.g., nearly pure quartz sand dunes on Earth). Eolian sediments may have minor mineral fractionation patterns across bedforms or based on distance from a source rock [*Mangold et al.*, 2011]. The base of eolian deposits may accumulate local bedrock during formation. However, these geochemical effects are relatively minor and the bulk composition of wind-blown sands is typically fairly homogeneous. Indeed, on Mars, eolian erosion and deposition over the last few billions of years is thought to be responsible for the consistent composition of the global dust layer as measured by different rovers at the surface [*Yen et al.*, 2005].

The Gale crater impact at ~3.8 Ga created a depositional basin for sediment collection and rock formation over several hundred million years [*Malin and Edgett*, 2000;

Anderson and Bell, 2010]. Investigation of the depositional environments of the sedimentary rocks exposed now in Gale crater provide a first-order constraint on the relative spatial area of sources integrated and types of geochemical trends that may emerge within each rock formation [*McLennan et al.*, 1993]. Fluvio-deltaic rocks, including the Bradbury group, are more closely linked with a local source area and may show more significant hydrodynamic transport effects. Lacustrine rocks, like the Murray formation, have a broader source region and are more likely to have consistent source input, but may affected by authigenesis or direct eolian or volcaniclastic input to the lake. Eolian sandstones integrate compositions from a large regional area and are more homogeneous, with potential loss of easily-eroded minerals. All of these sediments may then be affected by diagenetic cement addition and/or later chemical alteration. Here, we seek to understand the potential origins of geochemical trends in each formation.

5.2 Geologic Context

Gale crater is a 155-km diameter crater sitting across the large topographic dichotomy boundary on Mars. It contains a 5-km high central mound called Mount Sharp (formally Aeolus Mons), which is thought to surround the central peak of the crater, and shows exposed layered sediments on its northwest side. Based on observations of other similar craters [*Malin and Edgett*, 2000] and observed stratigraphy [*Grotzinger et al.*, 2015], the lower layers of Mount Sharp likely formed from sediments filling the crater basin and then were exposed by wind erosion of a moat around the mound. The Mars Science Laboratory *Curiosity* landed in the Gale crater moat (Aeolus Palus) in its northwest quadrant [*Grotzinger et al.*, 2014], and then drove ~9 km southwest across mostly fluvio-delatic Bradbury group sediments to the exposed layers at the base of Mount Sharp, where it is currently investigating the Murray and Stimson formations (Figure 5.1). Key waypoints from this traverse and a stratigraphic column based on elevation of observed deposits are shown in Figure 5.1. The Bradbury group sandstones and Murray mudstone are interfingered at the contact [*Grotzinger et al.*, 2015], whereas the Stimson sandstone sits atop an undulating unconformity above the Murray mudstone [*Watkins et al.*, 2016].

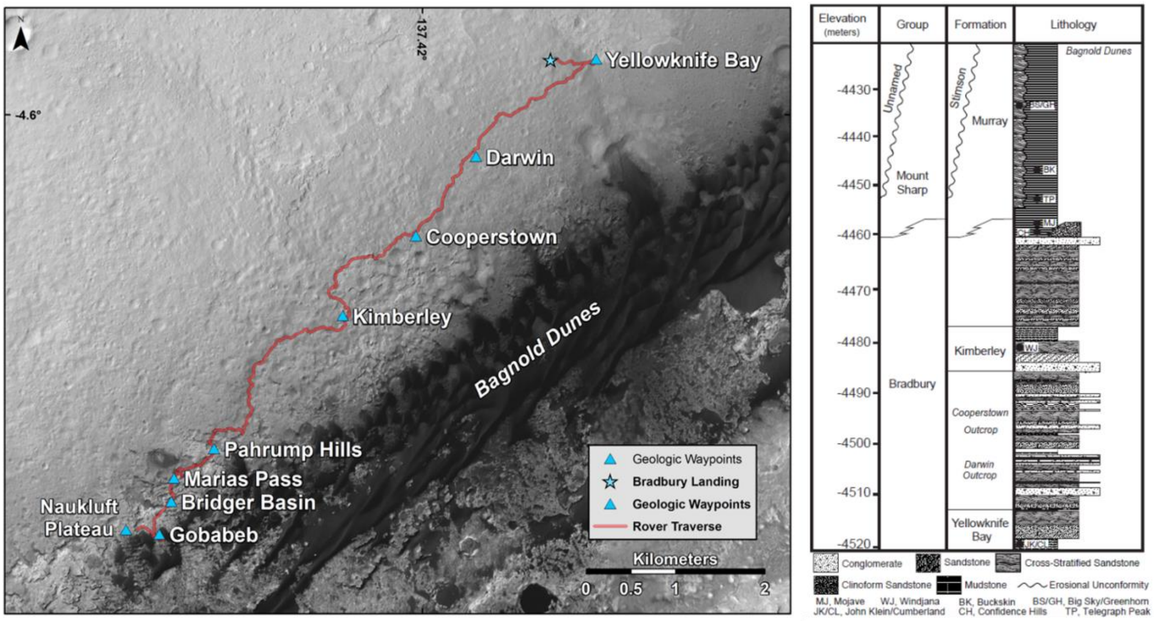

Figure 5.1 Overhead Map and Stratigraphic Column for *Curiosity* Traverse to Sol 1300 Overhead map of *Curiosity* traverse and major geological waypoints up to sol 1300, and stratigraphic column based on elevation showing the lithology of the exposed rocks and the drill targets [modified from *Grotzinger et al.*, 2015].

5.2.1 Bradbury Group

The Bradbury group encompasses all of the rocks observed in Aeolus Palus, which include sedimentary rocks from mudstones to conglomerates. The lowest-elevation unit analyzed by the *Curiosity* rover is the Sheepbed mudstone [*Grotzinger et al.*, 2014], a basaltic mudstone with ~30% authigenic phyllosilicates and a composition near or slightly more alkaline than average Mars crust [*McLennan et al.*, 2014; *Vaniman et al.*, 2014]. Diagenetic features in this unit include early preferentially cemented ridges and nodules as well as late cross-cutting $CaSO_4$ veins [*Nachon et al.*, 2014; *Siebach et al.*, 2014; *Stack et al.*, 2014]. After the Sheepbed mudstone, the rover traversed over ~9 km of Bradbury group sedimentary rocks with an elevation and stratigraphic height gain of ~60 m. A few waypoints were selected for more detailed sampling campaigns; these are identified in Figure 5.1. Analysis of the geometry, textures, and grain sizes of the sandstones and conglomerates indicate that the Bradbury group is composed of fluvio-deltaic deposits sourced from the northern rim of Gale crater [*Grotzinger et al.*, 2015; *Szabo et al.*, 2015]. These rocks are well-lithified, with low porosity, and the main diagenetic features are cross-cutting $CaSO_4$ veins [*Nachon et al.*, 2014], and one high-MnO and Zn fracture fill in the Kimberley outcrop [*Lanza et al.*, submitted]. While the geochemical diversity of the Bradbury group is high, the geochemical trends are typically linear and well-correlated with grain size variations, which has been interpreted to indicate that the source rock is relatively homogeneous, likely a porphyritic basalt, and that the geochemical diversity results from mineral sorting during transport [*Siebach et al.*, in prep.]. There is, however, a unique source with high potassium in the form of sanidine that contributes detritus to the Bradbury group in some stratigraphic layers, forming a spike in K_2O content with elevation, especially around the Kimberley outcrop [*Treiman et al.*, 2015; *Siebach et al.*, in prep.].

For this study, the Sheepbed mudstone will be plotted separately from the rest of the Bradbury group because we are interested in splitting the units based on depositional environment. The Sheepbed mudstone is the lowest unit currently exposed in the floor of Gale Crater and was measured over 1.5 m of elevation. Extensive sampling of this mudstone provides good constraints on the chemistry and mineralogy at this site [*Bish et* *al.*, 2014; *McLennan et al.*, 2014; *Vaniman et al.*, 2014], and compositionally it is consistent with the rest of the Bradbury group sediments [*Siebach et al.*, in prep.]. However, the spatial extent and timing of this lake relative to the lake that formed the Murray mudstone is not well-constrained [*Grotzinger et al.*, 2015]. For this study, the Sheepbed mudstone will be plotted for a comparison of different mudstone chemistry, but the focus will be on the comparison between the Murray mudstone lake and the Bradbury group sandstones, which are interfingered and therefore time-correlative deposits [*Grotzinger et al.*, 2015], and provide a basis for comparing the geochemical differences between distinct depositional environments.

5.2.2 Murray mudstone

The Murray formation is the lowest exposed unit on Mount Sharp and was first encountered by the *Curiosity* rover on sol 750 after crossing over an orbitally-defined boundary between Aeolus Palus and Mount Sharp. Topographic relief at this boundary allowed observations of stratigraphy at repeating elevations, which showed that the Bradbury group sandstones are interfingered with the Murray formation mudstones [*Grotzinger et al.*, 2015].

The Murray formation is composed of flat-lying laminated mudstones through at least 40 m of exposed stratigraphy, so there was a lake for an extended period of time at this site in Gale crater. The sources for this lake would have been more laterally extensive than the sources for the Bradbury group (Figure 5.2). The laminations are parallel and continuous over several m, and there are suggestions of lateral transitions between thinly laminated mudstones and thickly laminated mudstones, consistent with the distal deposits of hyperpycnal or hypopycnal plumes discharging into a lake [*O'Brien*, 1996; *Grotzinger et al.*, 2015]. Most of the Murray bedrock analyzed by *Curiosity* is the thinly laminated bedrock, with the finest scale laminations occurring at Marias Pass. The lowest 12 m of elevation of exposed mudstone outcrop make up the Pahrump Hills, which were extensively studied by *Curiosity*, including three drill holes (Confidence Hills, Mojave, and Telegraph Peak) and numerous compositional measurements. The next drilling

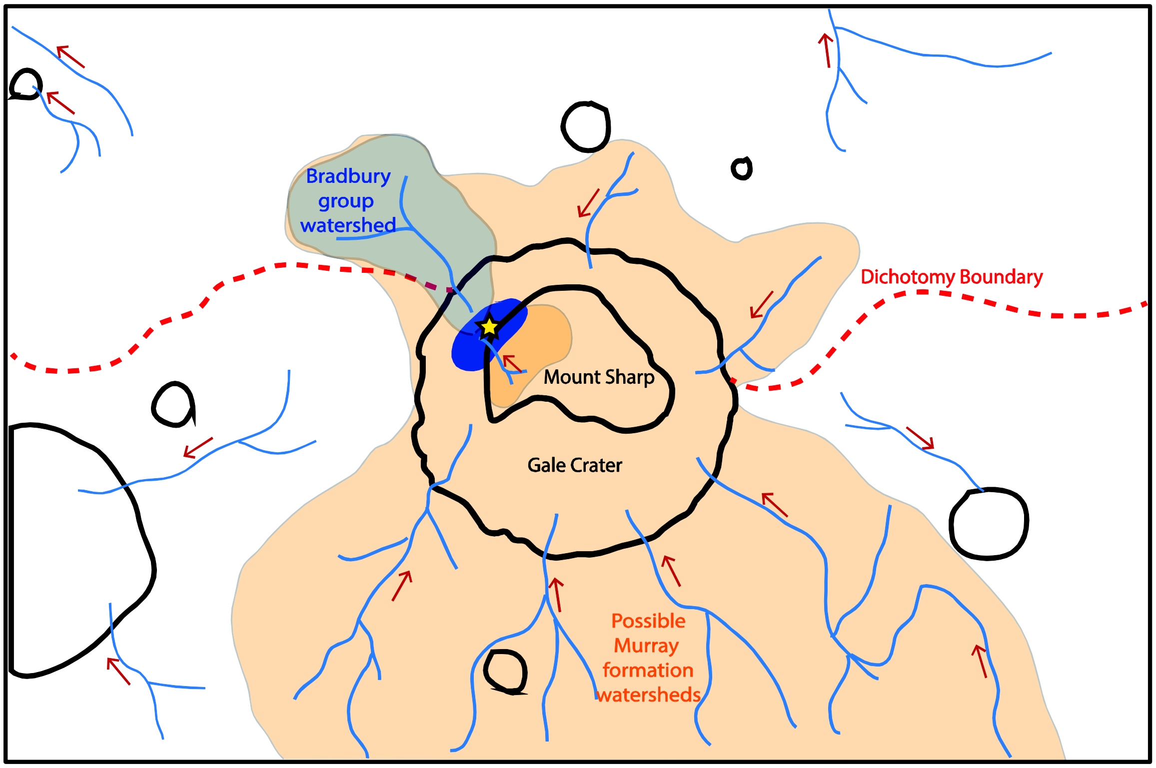

Figure 5.2 Schematic Overhead View of Sources of Rock Formations in Gale Crater
Schematic overhead view of Gale crater and surrounding area, showing schematic watersheds (actual watersheds at time of Murray formation are not known) and source areas sampled to provide detrital input to each of the rock formations considered here. Red arrows show direction of water flow. The watershed for the Bradbury group is highlighted in blue, the set of watersheds around Gale crater that feed the Murray lake system are marked as orange, and the Stimson formation sources (not shown) come from a larger regional area that may be incorporated into windblown sediment. Star is rover position. Gale crater is 154 km across for an approximate scale.

campaign was the Buckskin target in Marias Pass, and later waypoints for compositional analyses include Bridger Basin, Gobabeb, and Naukluft Plateau (Figure 5.1).

Although the Murray formation is consistently laminated mudstone, there are a variety of textural and chemical indicators of diagenetic activity. At the base of the Pahrump Hills outcrop, there are erosion-resistant dendritic structures up to a few cm across that show elevated MgO, SO_4, and Ni. At the Bridger Basin outcrop, there is a sharp diagenetic front between light-toned material near a fracture and typical bedrock that cross-cuts bedding, which is thought to be a diagenetic fracture halo (Cody target). At the Gobabeb and Naukluft Plateau outcrops, there are also nodular concretions in Murray bedrock. These three types of targets are removed when diagenetic targets are removed in plots, because they are visibly and chemically distinct from bedrock. The Murray formation also has a significant section of light-toned bedrock at the Marias Pass outcrop, but it is not well-understood if this bedrock is authigenic and primary, or secondary and diagenetic, so those samples are included in the bedrock compositions and not removed when diagenetic targets are excluded.

5.2.3 Stimson sandstone

The Stimson formation is an eolian crossbedded sandstone first encountered just above the Pahrump Hills outcrop. It is not time-correlative with the Murray formation or the Bradbury group, but instead sits above a climbing, undulating, draping unconformity above the Murray formation on Mount Sharp [*Watkins et al.*, 2016]. Interestingly, despite having been deposited after the Mount Sharp groups, based on the draping unconformity, this sandstone is well-lithified and contains fractures with light-toned diagenetic halos and small $CaSO_4$ filled fractures, indicating that the sandstone was buried, lithified, affected by later fluid flows, and later exposed again. Targets on the light-toned fracture halos in the Stimson unit are considered diagenetic and excluded when diagenetic targets are excluded. While the Stimson is not time-correlative with the Bradbury group and Murray formations, it likely includes some of the same source rocks and provides a distinct depositional environment for comparison.

5.2.4 Outliers

Two sets of targets encountered near the Mount Sharp boundary do not clearly fit into the main formations listed here, and do not have enough samples as of sol 1300 to investigate fully, so these targets will not be included in this study. These include four analyses of a cross-stratified interbedded sandstone channel called Whale Rock in the Murray formation in the upper part of the Pahrump Hills outcrop and four analyses of float rocks distributed between the upper Bradbury and within the Mount Sharp groups. The source for Whale Rock is unknown; it is interbedded in the Murray formation, and has lensoidal geometry, suggesting a fluvial or subaqueous channel cutting through the mudstone. However, it has a distinct depositional environment from the Murray mudstone and distinct chemistry from the Bradbury group, including very high CaO and low K_2O, so it is not included in either formation. Other outliers include Wildrose (sol 696), which is a high-K_2O float rock with an otherwise Murray-like composition sitting on top of Bradbury group rocks near the contact, Little Devil (sol 942), a high-K_2O float rock that appears to have rolled down from a thickly-laminated section of the Murray and may represent a mixture of Bradbury group and Murray formation compositions, and Ravalli (sol 1082) and Badlands (1102), both of which are float rocks in a rubbly deposit.

5.3 Methods

5.3.1 APXS

The Alpha-Particle X-ray Spectrometer (APXS) measures the bulk composition of a 1.7-cm diameter circle on in-situ targets. The instrument uses a ^{244}Cm source to produce alpha particles, which excite electrons in the sample, releasing characteristic x-rays for each element. The measurement penetration depth varies from 2 to 80 µm, increasing with elemental mass and allowing measurements of elements from Na to Fe [*Gellert et al.*, 2009; *Campbell et al.*, 2012; *Gellert and Clark*, 2015].

Up to sol 1300, the APXS instrument had acquired 303 total compositional analyses. For this study, we always exclude: soil samples (n=30); extreme diagenetic samples, including those with >30 wt% SO3 + CaO and the Stephen fracture fill with >3 wt% MnO (n=19); and multiple observations of the same target spot repeated for poor instrument performance (n=7). We also exclude the 8 outlier targets described earlier, including Whale Rock (n=4) and debris flow float rocks (n=4). The remaining analyses include 42 analyses on the Sheepbed mudstone, 73 on Bradbury sandstones, 86 on Murray formation mudstones, and 38 on Stimson sandstones. Characteristics of these are tabulated in Table 1.

For this study, drilled powder analyses are frequently excluded in order to better compare similar types of analyses and because there are up to eight drilled powder analyses for a given drill hole, so including all of the drilled analyses can bias the average composition of the entire rock formation towards the specific composition in one drilled hole. When drill powdered samples are included, they are marked with a * for identification. Float rocks only include rocks whose origin is not obvious; broken bedrock near its source is not considered float. 'Diagenetic' textures include samples with visible diagenetic features, such as minor $CaSO_4$ veins, nodules, hollow nodules, raised ridges, dendrites, and fracture halos; these types of samples are identified on plots in this study as hollow circles instead of filled circles (Figure 5.3). The high-SiO_2 samples in the Murray formation may be diagenetic or authigenic, so they are included with the bedrock. Brushed samples have had their surfaces cleaned with *Curiosity*'s Dust Removal Tool; this allows better analyses of the surface composition without dust cover, but there are not enough brushed analyses to use them exclusively, and dust cover varies enough between targets that in some cases a non-brushed sample may be as clean as a brushed sample. Furthermore, brushed and un-brushed surfaces were not found to have a consistent compositional change in the samples in this study, so both types of targets are included.

Unit	Total Analyses (no repeats)	Float Rocks	Drilled Powder Analyses (*)	Diagenetic Textures (o)	Brushed Samples
Sheepbed Mudstone	42	0	13	19	5
Bradbury group sandstones	73	22	4	0	3
Murray formation	86	0	17	15	48
Stimson formation	38	0	10	9	6

Table 5.1 Types of APXS Analyses for Each Gale Crater Formation

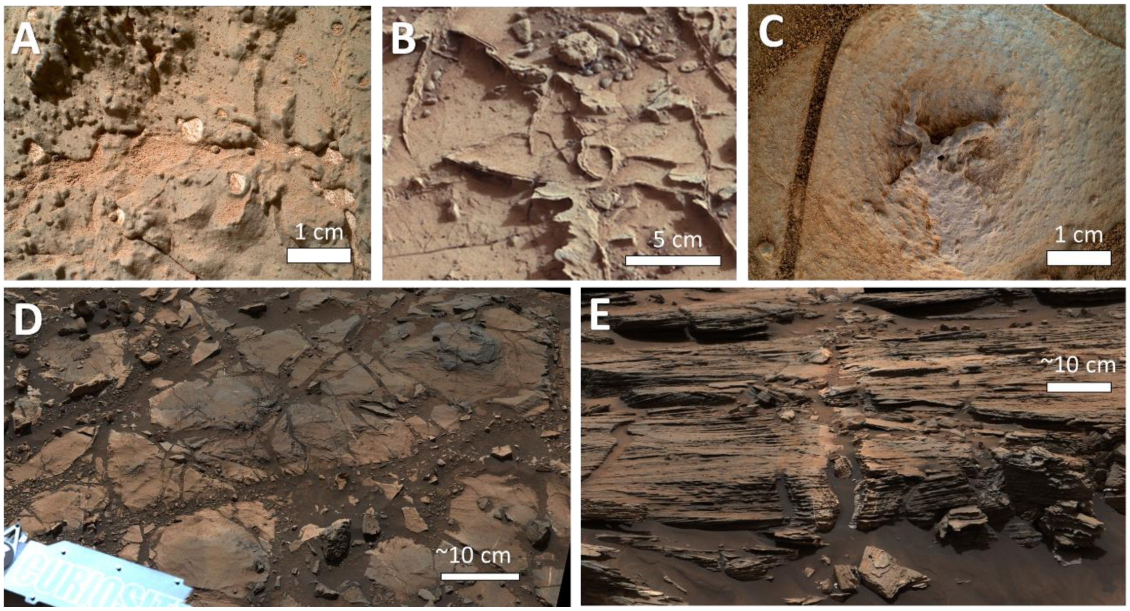

Figure 5.3 Panel Showing Diagenetic Features in Each Gale Crater Formation

Panel showing diagenetic features encountered in each of the formations considered here. Note different scales. (a) MAHLI image with nodules, hollow nodules, and CaSO4 veins in the Sheepbed mudstone (sol 154 0156MH0001810000101540R00_DRCX), (b) Mastcam-100 image showing raised ridges in the Sheepbed mudstone (sol 164), (c) MAHLI image of dendrite in Murray formation (sol 767 0767MH0001930000300172R00_DRCX), (d) Mastcam-100 workspace image of light-toned fracture-associated halo in the Murray formation, the Cody target is from the light-toned section here (sol 1108, mcam04927) (e) Mastcam-100 image of light-toned fracture-associated halo in the Stimson formation (sol 994, mcam04398).

5.3.2 CheMin

The Chemistry and Mineralogy (CheMin) instrument does powder X-Ray Diffraction (XRD) analyses on drilled rock powders, providing quantitative mineralogy in terms of unit-cell parameters and abundances of crystalline mineral components at the 2% level and above [*Blake et al.*, 2012; *Bish et al.*, 2014]. Crystal chemistry analysis using the unit-cell parameters allows estimation of the average crystalline mineral compositions for olivine, pyroxene, plagioclase, and other crystalline components [*Vaniman et al.*, 2014; *Morrison et al.*, 2015]. Amorphous components are then estimated in two ways: by curve-fitting the amorphous hump in the XRD-pattern, and by subtracting the compositions of the crystalline mineral components from the overall sample composition as determined by an APXS analysis on the drilled powder [*Dehouck et al.*, 2014; *Morris et al.*, 2014].

Curiosity has analyzed nine rock samples as of sol 1300 with the CheMin instrument. Two of these were in the Sheepbed mudstone (John Klein, Cumberland) [*Vaniman et al.*, 2014], one in the Bradbury group sandstones (Windjana) [*Morrison et al.*, 2015; *Treiman et al.*, 2015], four in the Murray formation (Confidence Hills, Mojave, Telegraph Peak, Buckskin), and two in the Stimson formation (Big Sky, Greenhorn).

5.4 Geochemistry of Gale Crater units

Geochemistry of sedimentary rocks depends on the source rocks for the detrital grains, sorting of those detrital grains during transport, chemical weathering or alteration processes, authigenesis (in-situ precipitation from surface water), and diagenesis (cement precipitation from groundwater). The relative importance of each of these effects varies depending on depositional environment and local climatic and aqueous conditions. Here, we seek to describe the geochemical variability and trends within distinct depositional environments observed by *Curiosity* in Gale crater in order to back out information concerning the source rocks and local climatic and aqueous environments.

5.4.1 Bulk Geochemical Differences between units

5.4.1.1 Ternary Diagrams

Curiosity has observed significant numbers of samples from four sedimentary rock formations representing three distinct depositional environments: the lacustrine Sheepbed formation, the fluvio-deltaic Bradbury group, the lacustrine Murray formation, and the eolian Stimson formation. In Figure 5.4, ternary diagrams are used to show multi-element compositional variability in each of these formations.

Figure 5.4a is an A-CN-K ternary, based on the molar abundances of Al_2O_3, CaO + Na_2O, and K_2O. This ternary diagram is designed to highlight feldspar compositions and weathering. The plagioclase-feldspar join, plotted across the middle of the ternary, segregates samples by relative proportions of (Na_2O- and CaO-bearing) plagioclase and (K_2O-rich) alkali feldspar. The Sheepbed and Stimson formations have the least total K_2O (i.e. more plagioclase relative to K-feldspar), the Murray formation has intermediate K_2O, and the Bradbury group shows the most variability in (K-feldspar)/(Na, Ca-plagioclase) ratio. This is further highlighted in Figure 5.5. Vertical sample segregation is related to the Chemical Index of Alteration (CIA) scale on the left, a measure of the molar ratio of Al_2O_3 to CaO + Na_2O + K_2O labile cations, which allows quantification of the degree of feldspar weathering and cation loss. Typically, CaO is corrected to CaO* and includes only the CaO in silicate minerals, but in this case (and for Mars samples in general), we do not have an analytical technique to segregate CaO from silicates from CaO from other minerals, so the CaO is uncorrected. This means that the values shown here are minimum CIA values, plotting lower on the ternary (and closer to the plagioclase join) than they would if, for example, $CaSO_4$ were removed. Primary igneous minerals plot on or below the plagioclase-feldspar join, whereas illite or kaolinite would plot at the Al_2O_3 tip of the ternary. Bradbury group, Sheepbed formation, and Stimson formation samples all plot below the plagioclase-feldspar join, with near-igneous CIA values. Some of these samples plot below CIA 35; these are likely offset due to significant CaO in non-silicate minerals. Murray samples show higher CIA values, up to 52.6 (Afton Canyon target, sol 813), indicating that there has been some chemical weathering, or feldspar cation loss relative to Al_2O_3, in the Murray formation or its source region

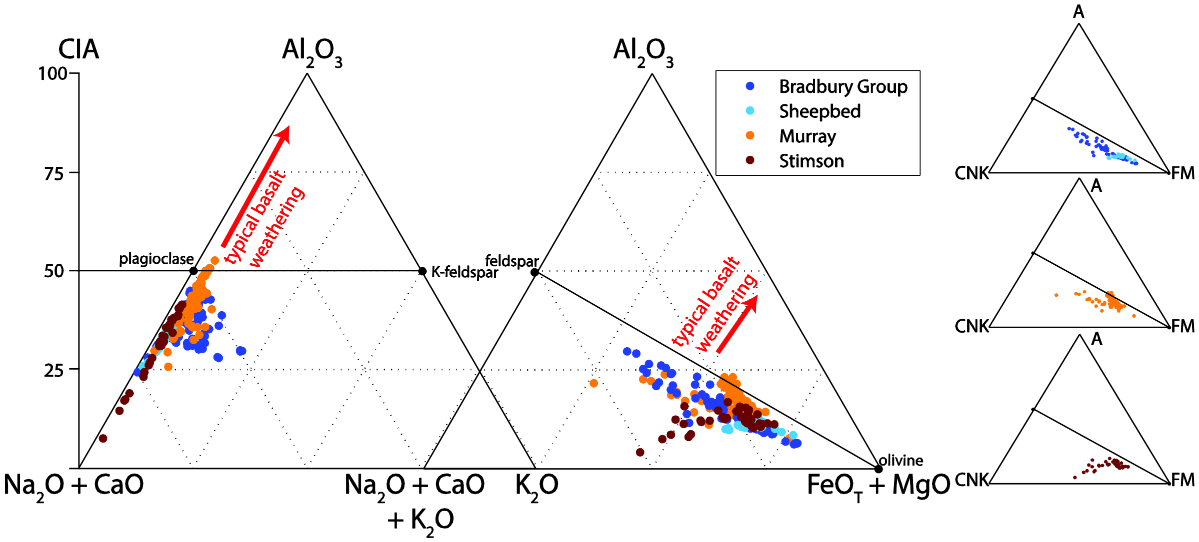

Figure 5.4 Ternary Diagrams for Gale Crater Formations

A-CN-K and A-CNK-FM ternary diagrams displaying the overall compositional variability of four rock formations; the Sheepbed mudstone, Bradbury group sandstones, Murray mudstone, and Stimson sandstone. All targets are included in this figure, including diagenetic features. Small ternary diagrams on the right display each formation separately for ease of seeing trends (Sheepbed mudstone superimposed on Bradbury group sandstones).

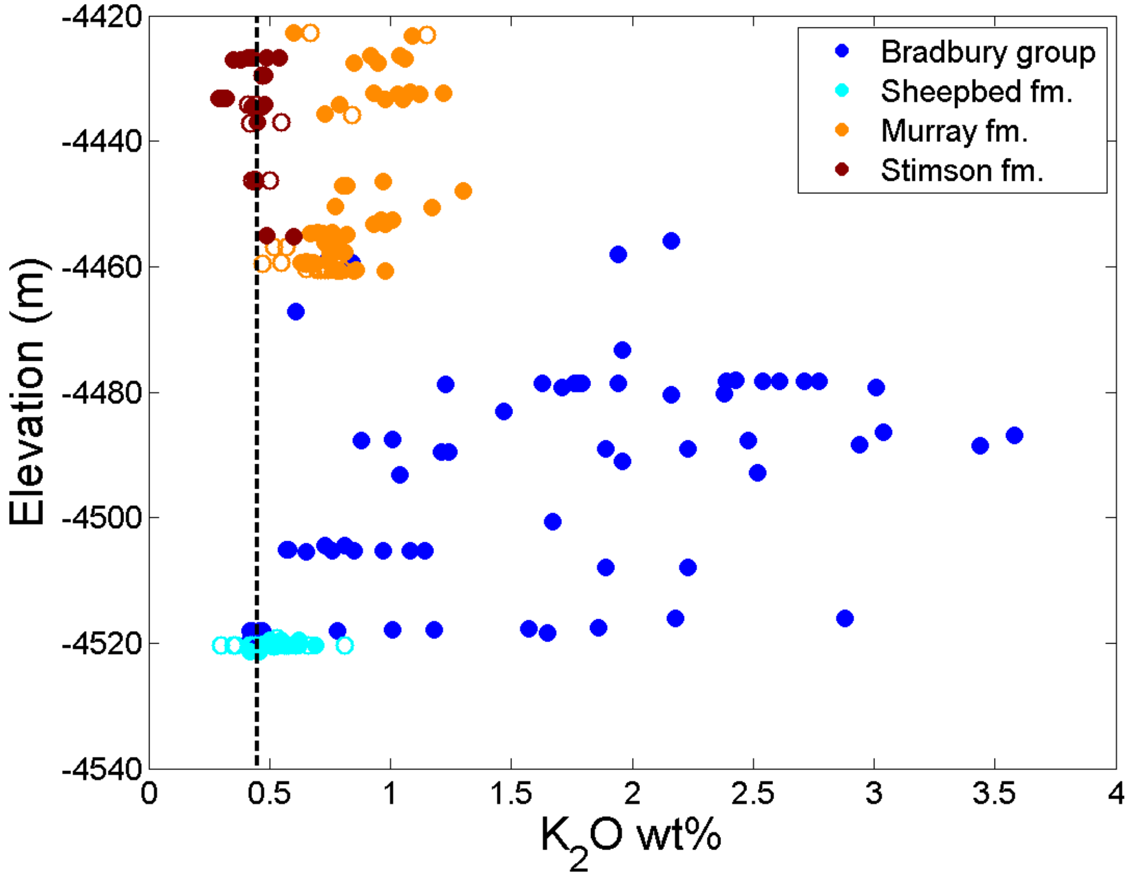

Figure 5.5 K_2O vs. Elevation for APXS Samples to Sol 1300
Variation in K_2O content with elevation for the Sheepbed, Bradbury, Murray, and Stimson formation targets. Bedrock targets shown as filled circles, diagenetic targets as hollow circles. Dashed vertical line represents the K_2O content of average Mars crust [*Taylor and McLennan*, 2009].

Figure 5.4b and c show mafic ternary diagrams, which incorporate molar ratios of FeO_T + MgO to better show elemental distributions for mafic components. Samples plot closer to the FM apex when they have more mafic components, like olivine and pyroxene, and trend towards the feldspar apex when there is an increase in plagioclase and feldspar relative to mafic components. Chemical weathering of igneous components pulls the compositions above the feldspar-FM join. The Bradbury group shows significant spread parallel to the feldspar-FM join, interpreted by Siebach et al. [in prep.] as separation of plagioclase from mafic minerals during transport [e.g. *Nesbitt and Young*, 1984; *Fedo et al.*, 2015]. The Murray formation has a tighter cluster of compositions, indicating less overall compositional variability for these elements, but these compositions go over the feldspar-FM join, indicating some chemical weathering or cation loss. The Murray also has samples that parallel the feldspar-FM join, like Bradbury samples, indicating depletion of mafic minerals relative to the majority of the bedrock. The Stimson formation forms an even tighter cluster of compositions, with a few samples shifted towards the CNK apex, likely due to uncorrected non-silicate CaO from $CaSO_4$ enrichment.

5.4.1.2 Elevation

Bedding is essentially horizontal for the rocks explored so for by *Curiosity*, and so elevation provides a convenient surrogate for stratigraphic position [*Grotzinger et al.*, 2014; *Grotzinger et al.*, 2015]. In terms of bulk geochemistry, one of the best ways to distinguish between the major sedimentary formations is the potassium content. Figure 5.5 highlights the variation in potassium with elevation, in bedrock and ‘diagenetic’ targets, for the four rock formations considered in this study. The comparison in potassium content between rock formations is also striking; the differences in absolute K_2O and the range of K_2O wt% in different samples distinguish each rock formation with little overlap, even when ‘diagenetic’ samples are included (shown in hollow circles in Figure 5.5). The Stimson formation has the lowest potassium, 0.29 to 0.6 wt%, with an average of 0.44 wt%, which closely matches the average Mars crust value of 0.45 wt% [*Taylor and McLennan*, 2009]. The Sheepbed formation also has low potassium, 0.3 to 0.81 wt%, with an average of 0.53 wt%. The Murray formation has higher potassium but still muted variability; the potassium content ranges from 0.47 wt% in 'diagenetic' samples, or a minimum of 0.6 wt% in non-diagenetic samples, to 1.3 wt%. The Bradbury group has a much wider range in potassium content, from 0.42 wt% to 3.58 wt%. Potassium content with elevation has been discussed for the Bradbury group because the K_2O content, and especially the K_2O/Na_2O content, spike in the Kimberley formation (at about -4480 m elevation), interpreted as a flux of sediment from a sanidine-rich source region in [*Treiman et al.*, 2015; *Siebach et al.*, in prep.]. The elevated values and high variability of K_2O in the Bradbury group compared to the elevated values but low-variability K_2O in the Murray and the average crustal values of the Stimson may be accounted for based on the different depositional environments of each rock formation.

5.4.1.3 Bulk Compositional Differences in Bedrock

In order to compare the effect of the different depositional environments and related source rock variability for each of the three major units, it would be ideal to only compare samples not affected by later diagenetic processes. Of course some diagenetic process, including cementation and lithification, affect all of the rocks and cannot be avoided, but rocks that are more clearly affected by diagenetic fluid flows, including $CaSO_4$ veins, nodules, preferentially cemented raised ridges, dendritic features, light-toned fracture-associated halos, and concretions (Figure 5.3) are all removed from the bedrock comparison shown in figure 5.6. These boxplots allow comparison of the median value and level of variation in the compositions of the bedrock portion of the different rock formations and depositional environments, and comparison of these formations to average Mars crustal compositions.

Excluding outliers, the Bradbury group shows the overall highest compositional variability in most elements, except that P_2O_5, Ni, and Zn have higher variability in the Murray (Figure 5.6f, l, and m) and SO_3 has higher variability in the Stimson formation (Figure 5.6n). The Murray formation has compositional outliers in the Marias Pass region with extreme values in SiO_2, FeO, TiO_2, and P_2O_5 that cause higher than expected variability (Figure 5.6a, c, e, f). Sulfur has similar variability in all groups, and it is known to have moved, at least through fractures, in late-stage fluids due to pervasive $CaSO_4$ veins

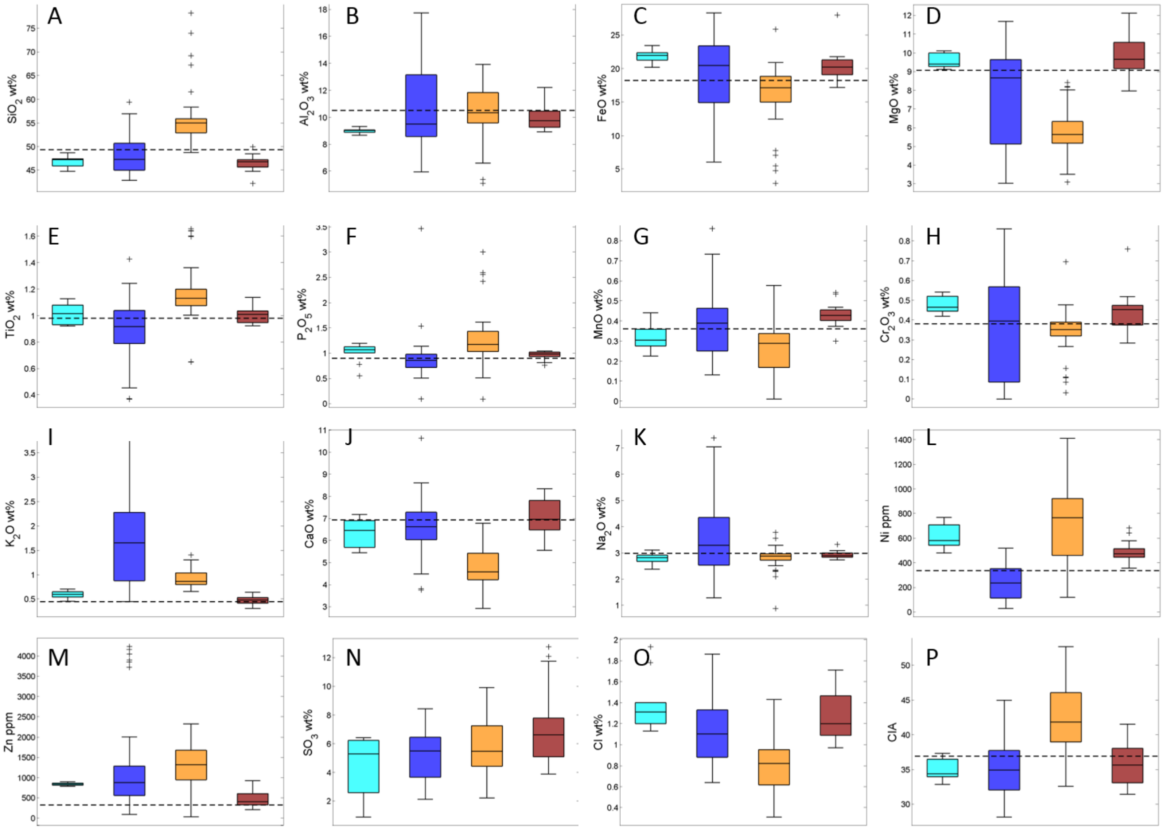

Figure 5.6 Boxplots of Median Compositions for Gale Crater Formations

Boxplots showing the compositions of each of the four rock formations: Sheepbed formation in cyan, Bradbury group in blue, Murray formation in yellow, and Stimson formation in dark red. Diagenetic samples excluded. Dashed line represents average Mars crust composition. Plots A-M are calculated SO3- and Cl- free compositions for accurate comparison with average Mars crust. Plot P shows calculated CIA values for each unit. The central line of the boxplot is the median composition, the upper and lower bounds of the colored box are the 25th and 75th quartiles of the data. The upper and lower whiskers extend to the minimum and maximum compositions excluding outliers. Outliers, represented by + symbols, are plotted when whisker length is more than 1.5x the length of the colored box.

in all observed units [*Nachon et al.*, 2014], but is most concentrated in the Stimson formation (Figure 5.6n).

The Sheepbed mudstone formation has low variability, which may be expected since it is measured over only 1.5 m of stratigraphy, and its composition is slightly more mafic than average Mars crust. It is enriched in FeO_T, MgO, Cr_2O_3, K_2O, Ni, and Zn relative to average Mars crust (Figure 5.6c, d, h, i, l, m) and depleted in SiO_2 and Al_2O_3 (Figure 5.6a, b). It shows consistently low CIA values, reflecting minimal chemical alteration of basaltic source rocks (Figure 5.6p).

The Bradbury group sandstones show significant variability, but the median elemental compositions are relatively similar to average Mars crust. Offsets from average Mars crust are expected due to the heterogeneity in grain sizes and compositions within this group and non-random sampling of different units. However, K_2O stands out because every sample analyzed in the Bradbury group had more K_2O than average Mars crust (Figure 5.6i). Bradbury group was also fairly consistently enriched in Zn and depleted in Ni (Figure 5.6l, m).

The Murray formation mudstones show intermediate sample variability and some of the most offset compositions from average Mars crust. Murray mudstones are enriched in SiO_2, TiO_2, P_2O_5, K_2O, Ni, and Zn (Figure 5.6a, e, f, i, l, m); they are depleted in FeO_T, MnO, Cr_2O_3 (Figure 5.6c, g, h); and they are extremely depleted in MgO and CaO (Figure 5.6d, j). The extreme depletion in CaO is related to the high CIA values in the Murray formation, indicative of cation loss (Figure 5.6j, p).

The Stimson formation has low variability and a composition very similar to average Mars crust. In fact, despite having extremely low variability, the range of volatile-free Stimson bedrock compositions includes average Mars crust for all elements except for Ni, which is enriched above crustal levels (Figure 5.6l). Median Stimson samples are slightly elevated in FeO_T and MgO, and slightly depleted in SiO2 and Al_2O_3, reflecting a slightly more mafic composition than average Mars crust (Figure 5.6a, b, c, d). The Stimson formation does, however, show elevated values and high variability in the volatile elements SO_3 and Cl. These elements are typically used as a proxy for Martian dust, and so elevated values may indicate more extensive dust cover for the Stimson unit, or they may reflect cements or components in the rock itself.

5.4.2 Bulk Element-Element Trends

Element-element trends help reveal the characteristics of minerals or fluids that change one sample relative to another (Figure 5.7). Element-element trends in the Bradbury group are mostly linear and are dominated by physical mixing of plagioclase with mafic minerals, so these trends are defined by the amount of plagioclase in the sample and the mineral composition of the plagioclase, which is ~An40 (Figure 5.7, Figure 5.8) [*Siebach et al.*, in prep.]. Sheepbed and Stimson bedrock samples are tightly constrained and do not show element-element trends, but ‘diagenetic’ samples show trends, revealing information about the groundwater fluids that altered the rock. Murray samples have significant trends, with different causes.

Figure 5.7 shows elemental trends for all rock formations with SiO_2 and Al_2O_3. Opposing trend directions in Murray and Bradbury group samples demonstrate that the element-element trends in the Murray formation must have different causes than the element-element trends in the Bradbury group. Titanium content in the Bradbury group is associated with igneous minerals and anti-correlated with SiO_2, but in the Murray formation TiO_2 increases with SiO_2, especially in a few extremely high-SiO_2 samples (Figure 5.7a). Al_2O_3, on the other hand, is depleted in the high SiO_2 Murray samples (Figure 5.7c). In the Bradbury group, Na_2O is an indicator of plagioclase, and trends consistently with SiO_2 and Al_2O_3, but in the Murray group Na_2O is quite constant regardless of Al_2O_3 or SiO_2 (Figure 5.7b). Unlike the Bradbury group, Al_2O_3 in the Murray formation trends with minor mafic components like Cr_2O_3, MnO, and MgO (Figure 5.7d, e, f), which may be related to detrital input vs authigenesis and/or a diagenetic fluid. The Sheepbed and Stimson formations tend to plot near average Mars crust and near the intersection of the Bradbury and Murray trends. High-SiO_2 ‘diagenetic’ Stimson samples plot near high-SiO_2 Murray samples, potentially indicating a genetic link between ‘diagenetic’ Stimson and high-SiO_2 Murray (Figure 5.7).

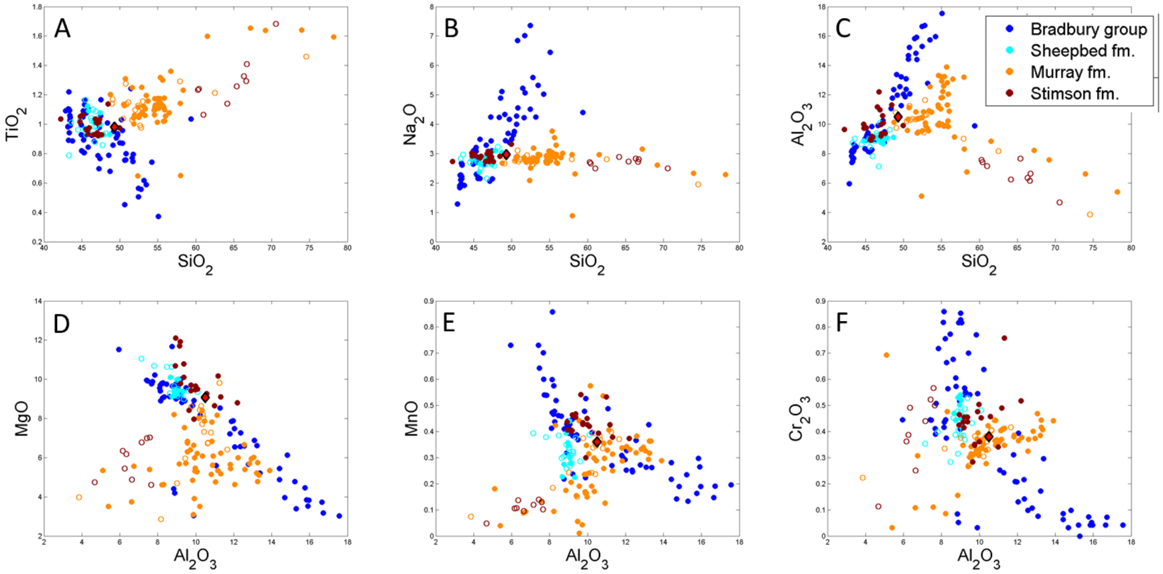

Figure 5.7 Element-Element Plots Comparing Gale Crater Formations

Element-element plots comparing the four rock formations. Compositions are SO3- and Cl- free for comparison to average Mars crust, plotted as a red diamond. Filled circles are bedrock targets, hollow circles are diagenetic features.

5.4.3 Dominant Geochemical Trends within Bedrock/Formations

5.4.3.1 Bradbury Group

The Bradbury group is composed of a heterogeneous mixture of fine sandstones to conglomerates and some float rocks with uncertain textures. Geochemical trends for all of these units tend to be linear, indicating that they fall along two-component mixing lines [*Langmuir et al.*, 1978]. When divided into classes based on grain size, the grain size variations correlate closely with the geochemical trends, such that SiO_2, Al_2O_3, and Na_2O are most concentrated in the coarsest grain sizes, and mafic components are most concentrated in the finest grained rock fraction. These trends were modeled in Siebach et al. [in prep.] and interpreted as mixing trends separating coarse-grained plagioclase from fine-grained basaltic groundmass, implying that most of the geochemical heterogeneity in the Bradbury group is not related to fluids or mixing of distinctive source rocks, but is dominated by physical sorting of mineral components from a basaltic source (Figure 5.8). The exception to this dominant trend is K_2O, which was interpreted to come from a chemically distinctive source that contributed variably to the Bradbury group during deposition [*Treiman et al.*, 2015; *Siebach et al.*, in prep.].

5.4.3.2 Murray Formation

The Murray formation is all laminated mudstone, but there are several distinctive elemental trends indicating changes in the regional source, changes in the lake chemistry/authigenesis, or diagenetic alteration of sediment compositions. These elemental trends fall into three broad categories: trends with elevation (Figure 5.9), trends surrounding the high-SiO2 region in Marias Pass (Figure 5.10), and trends throughout the bedrock (Figure 5.11).

Trends with elevation are typically related to shifting of the provenance composition or in-situ fluid movement within the sediments, whether authigenic or diagenetic. The lower 20 m of stratigraphy in the exposed Murray formation show approximately linear trends in Ni, Zn, MnO, and Al_2O_3 from an enriched zone at the base of the Pahrump Hills, to depleted compositions at Marias Pass (elevation -4443) (Figure 5.9). These trends do not continue in measurements above Marias Pass.

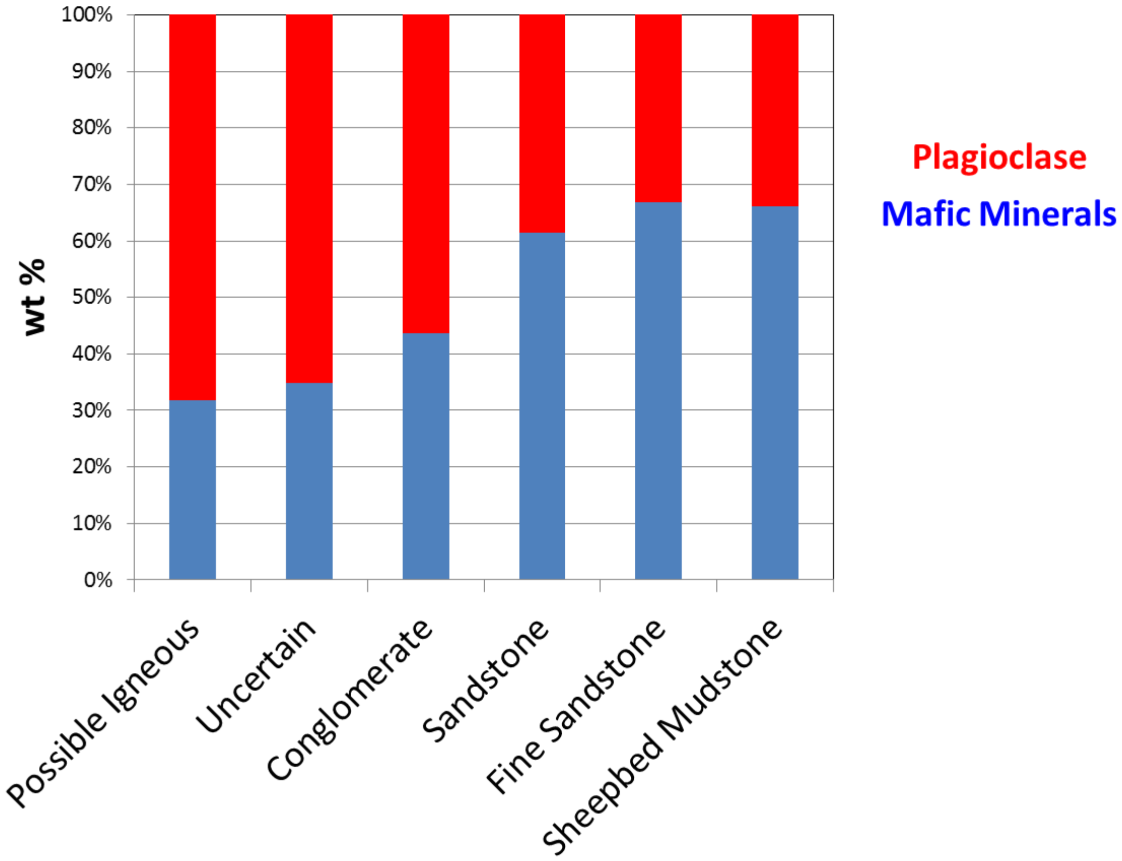

Figure 5.8 Bradbury Group Compositional Trends
This is a simplified version of Figure 4.8, showing the compositions of Bradbury group samples in terms of median modeled plagioclase and median modeled mafic mineral compositions of Bradbury grain size classes, from coarse grain sizes (left) to fine grain sizes (right). [*Siebach et al.*, in prep.]

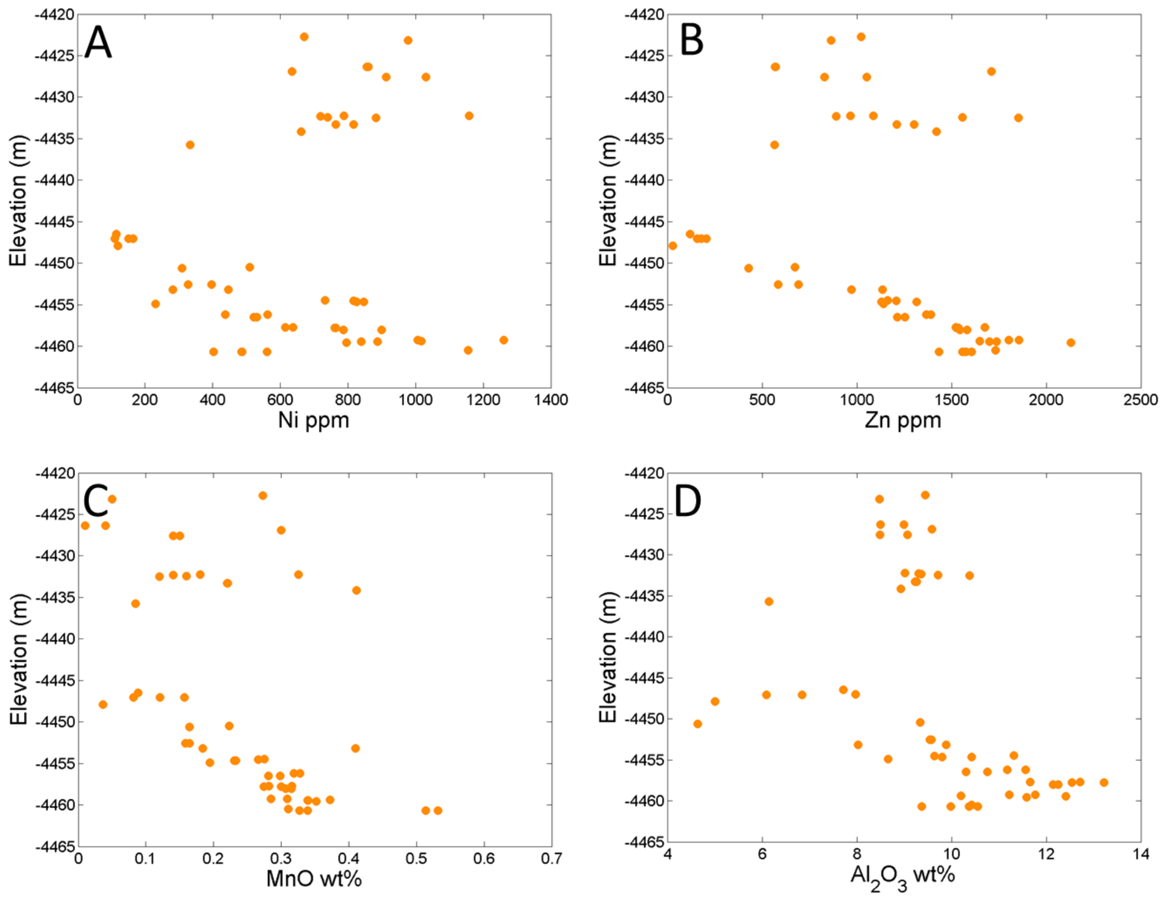

Figure 5.9 Murray Formation Trends with Elevation

Trends in composition with elevation in the Murray formation. Diagenetic samples excluded.

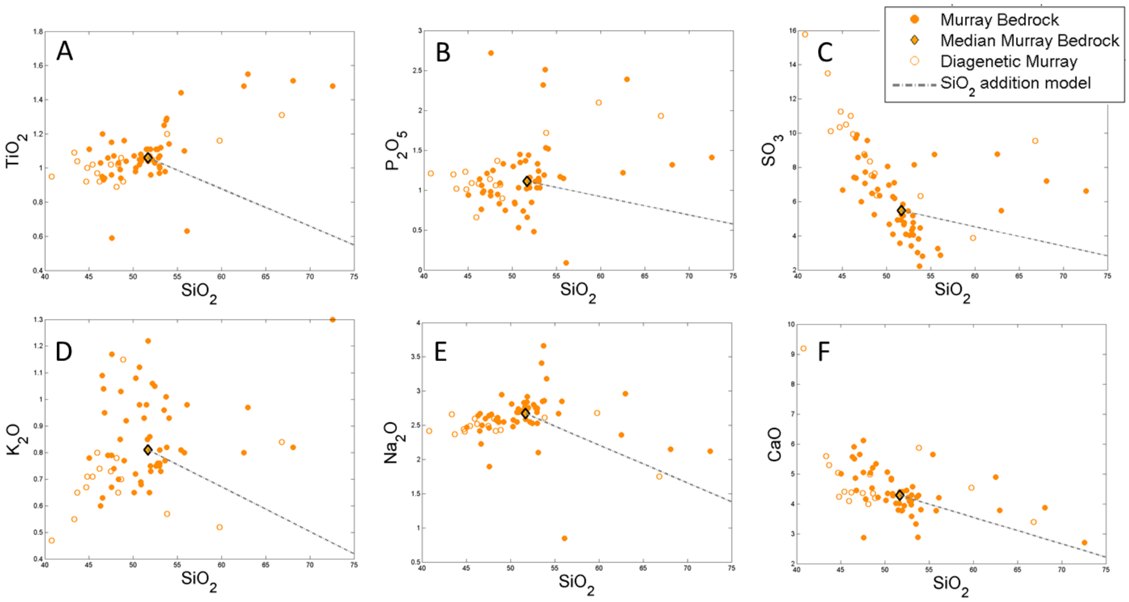

Figure 5.10 Silica-Addition Trends in the Murray Formation

Silica-addition trends in the Murray formation. Bedrock samples in filled circles, diagenetic samples are hollow circles. Diamond represents median Murray bedrock composition. Dashed line is a model for SiO2 addition (and dilution of other elements) from median Murray bedrock. Samples with >55wt% SiO2 are considered high-silica, elements that plot above dashed line are enriched or not diluted as expected with silica addition.

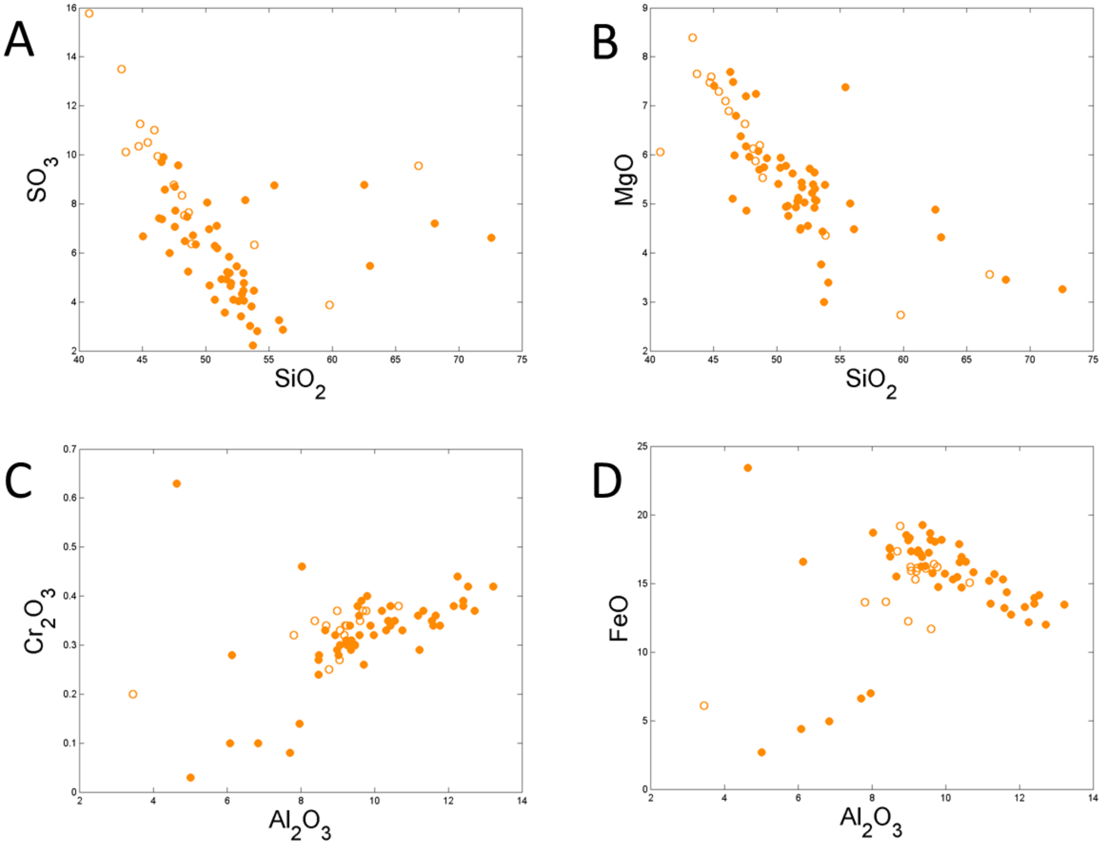

Figure 5.11 Compositional Trends in the Murray Formation

Compositional trends in the Murray formation. Bedrock samples are filled circles, diagenetic samples are hollow circles.

At Marias Pass, the Murray bedrock is light-toned and extremely SiO_2 enriched. Plots shown in Figure 5.10 show all of the Murray targets, where targets with $SiO_2 > 55$ wt% are considered silica-enriched. Median Murray bedrock is calculated from all non-diagenetic bedrock samples, and a simple two-component model for silica-enrichment and associated depletion of other elements of the median bedrock is plotted in grey. If the high-SiO_2 Murray samples had median Murray composition and were only enriched in silica, other components would fall at or below the model line, but instead TiO_2, P_2O_5, SO_3, and K_2O plot above the silica enrichment line, indicating that these elements are enriched together with the silica (Figure 5.10a, b, c, d). Plots of Na_2O and CaO also fall above the modeled silica-enrichment trend, but are still slightly depleted at extremely high silica content, so they may or may not be associated with the silica enrichment (Figure 5.10e, f).

In general, Murray bedrock shows relatively low elemental variability. Variations between elements are scattered, but there are a few trends in the bedrock components, shown in Figure 11. MgO and SO_3 are anti-correlated with SiO_2 (Figure 5.11a, b), and are correlated together, particularly in the dendritic concretions at the base of the Pahrump Hills (Figure 5.3c), represented by low-SiO_2 hollow circles in Figure 5.11. Figure 9 showed that Al_2O_3 is correlated with Zn, Ni, and MnO, and here we see it may also be correlated with Cr_2O_3 (Figure 5.11c), but is anti-correlated with FeO (Figure 5.11d). This is unlike the observations from the Bradbury group, where mafic mineral components were correlated with FeO and anti-correlated with Al_2O_3 and other feldspar components, implying that authigenic or diagenetic processes are dominating elemental trends in the Murray rather than igneous mineral components.

5.4.3.3 Stimson Formation

The Stimson formation is characterized by extremely low variability and near-average Mars crustal composition in the bedrock, with light-toned diagenetic fracture-associated haloes that sharply transect primary eolian cross-stratified bedding and have a distinct and also well-characterized composition. Figure 5.12 shows the bimodal distribution of Stimson unit compositions based on the light-toned fracture-associated halos (hollow circles in Figure 5.12). Analyses of powders from drilled targets Big Sky

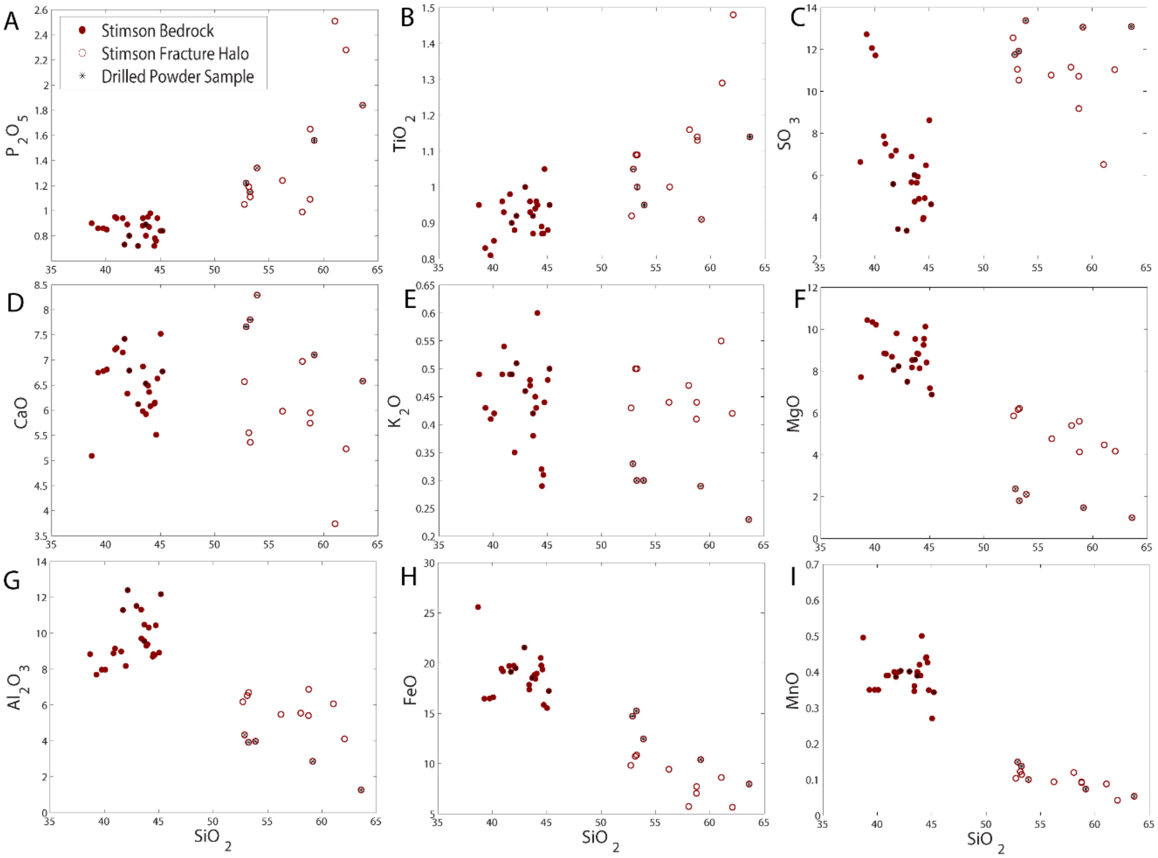

Figure 5.12 Compositional Trends in the Stimson Formation
Compositional trends in the Stimson formation. Bedrock samples are filled circles, diagenetic samples are hollow circles, drilled powder samples are marked with a ‘*’.

(unaltered) and Greenhorn (fracture-associated halo) are included in Figure 5.12 and marked with a * for distinction. The fracture-associated halos show elevated SiO_2, P_2O_5, TiO_2, and SO_3 relative to typical Stimson bedrock, and elevated CaO and K_2O relative to expected dilution of these elements (Figure 5.12), similar to the silica-enriched zones in the Murray bedrock. Elevated SO_3 and CaO are likely at least partially related to small $CaSO_4$ fractures that frequently align with light-toned fracture-associated halo zones (Figure 5.3e).

5.5 Discussion

Geochemical diversity and trends in sedimentary rocks can originate from source heterogeneities, transport processes, authigenic alteration or precipitation, or diagenetic processes. The range in expected trends in a system can be constrained based on the depositional environment. In Gale Crater, we constrain the causes of diverse geochemical trends in fluvial, lacustrine, and eolian bedrock systems.

5.5.1 Fluvio-deltaic

Fluvio-deltaic sedimentary rocks are known to have diverse compositions when the watershed is heterogeneous [*McLennan et al.*, 1990; *Carrapa et al.*, 2004], when different grain size classes are sampled [*Whitmore et al.*, 2004; *Fedo et al.*, 2015], or when diagenetic effects alter rock compositions. The Bradbury group of fluvio-deltaic sedimentary rocks in Gale crater is the most geochemically diverse rock formation studied by *Curiosity*. The observed geochemical diversity, however, can be explained to first-order by one dominant geochemical trend and one minor geochemical trend.

The major axis of compositional diversity in the Bradbury group can be summarized as the addition or subtraction of plagioclase minerals from typical Mars basalt, and this trend parallels the grain size variations in the observed samples, with the coarsest grains most enriched in felsic elements (Figure 5.8). This indicates that plagioclase minerals were likely present as phenocrysts in the basaltic source region, and were sorted during transport into coarser clasts [*Siebach et al.*, in prep.]. This trend does not require geochemical or even petrological diversity in the source region, only mineral size variations in the source basalt [*Fedo et al.*, 2015].

A second axis of compositional variability in the Bradbury group is shown in the trend in potassium, which, unlike other major elements, relates more strongly to elevation, or stratigraphic position, than to grain size (Figure 5.5). This elemental trend is best explained by an influx of sediment from a potassium-rich source region. Alternatively, potassium metasomatism could be invoked, but in this case there is no evidence for significant alteration of any type in either the elemental compositions or the XRD mineralogy, and abundant amorphous glassy material is also preserved, so the contribution of a potassium-rich source region is more consistent with the observations [*Treiman et al.*, 2015; *Siebach et al.*, in prep.]. This variable influx from distinctive sources with elevation is reasonable in a fluvial system because the rock types exposed to erosion in the watershed vary spatially and temporally, and this can cause dramatic compositional changes in the fluvial sediment (Figure 5.2) [*Vezzoli et al.*, 2004].

5.5.2 Lacustrine

The geochemistry of lacustrine rocks on Earth is a combination of the geochemistry of clastic, chemical, and biogenic inputs [*Schnurrenberger et al.*, 2003]. For Mars, we can ignore biogenic inputs and focus on clastic and chemical inputs. Clastic sediments can include erosional detritus, volcanic ash, or eolian fallout. There is likely regular clastic input in the Murray formation to make the consistent mm-scale laminations in the mudstone. This clastic input could change over time, especially if eolian fallout or volcanic ash play a significant role, but also simply due to changing watershed dynamics and units exposed to erosion around the lake. Chemical input can occur at different stages; cements or minerals that form from components in the lake water are authigenic, whereas cements that form in pore fluids in the groundwater during and after burial are diagenetic. Late-stage diagenetic cements may also occur after much of the rock has been lithified and porosity partially reduced. Chemical weathering or leaching may also occur, dissolving primary minerals or cements and altering input compositions, but this typically disrupts original depositional structures and may create secondary porosity.

5.5.2.1 Sheepbed formation

The Sheepbed mudstone, measured at the base of the Bradbury group, has a composition dominated by clastic input, with minimal evidence for chemical alteration. Indeed, modeling by Siebach et al. [in prep.] showed that the compositions of Bradbury group samples can be completely modeled as combinations of primary igneous minerals. CheMin XRD measurements of Sheepbed samples showed ~20 wt% phyllosilicates and ~30 wt% amorphous material [*Vaniman et al.*, 2014], both of which may have formed authigenically during closed-system in-situ chemical weathering of igneous components without cation-loss or significant fluid migration. Even diagenetic features within the Sheepbed, including raised ridges of erosion-resistant crack fill and nodules [*Siebach et al.*, 2014; *Stack et al.*, 2014], only show slight chemical differences from the average Sheepbed bedrock composition [*Léveillé et al.*, 2014; *Siebach et al.*, in prep.]. $CaSO_4$-filled veins reveal a distinct fluid composition, but these clearly cross-cut bedrock and earlier diagenetic features and, based on ChemCam rasters, do not seem to have impacted bedrock compositions outside the filled fracture zone [*Nachon et al.*, 2014]. The extent and duration of the lake that produced the Sheepbed mudstone is uncertain due to limited stratigraphic exposure of this unit, but the lake was dominated by fine-grained clastic input from typical Mars basaltic sources similar to the Bradbury group sandstones.

5.5.2.2 Murray formation overview

The Murray mudstone is more complex than the Sheepbed mudstone. Consistent mm-scale laminations throughout the mudstone are indicative of regular clastic input by suspension settling of injected clastic plumes and flows into the lake [*O'Brien*, 1996; *Grotzinger et al.*, 2015]. The preservation of these laminae implies that diagenetic leaching and alteration was somewhat limited. The chemical compositions here, specifically an excess of SiO_2 and alternating hematite and magnetite concentrations, indicate that authigenic precipitation is significant as well as clastic input [e.g. *Ramseyer et al.*, 2013]. Indeed, all of the CheMin XRD results in this section include significant volumes of high-SiO_2 amorphous material (20+ wt%) in addition to other amorphous material and crystalline material (Figure 5.13) [*Rampe et al.*, in prep.]. Furthermore, there is evidence for localized diagenetic activity that formed features with distinct chemistries, including MgO, SO_4, and Ni-enriched dendrites, a SiO_2, P_2O_5, TiO_2, and K_2O-enriched fracture halo, and $CaSO_4$-filled fractures. This combination of clastic inputs, chemical inputs, and diagenetic features can make it difficult to interpret the chemical signature of each component, but some patterns emerge when both mineralogical and chemical data are considered. It is important to keep in mind that, while the Murray formation and the upper Bradbury group are time-equivalent, the lake that formed the Murray mudstone integrated multiple watersheds and could have very different sources from the Bradbury group (e.g. Figures 5.2 and 5.7) and that, although we discuss geochemical trends and variability in detail, the overall geochemical diversity of the Murray formation is still less than that of the Bradbury group (Figure 5.6).

5.5.2.3 Clastic inputs to the Murray formation

The section between the base of Pahrump Hills and Marias Pass includes four drilled samples in the Murray, so we can begin to constrain the clastic component of each sample using the mineralogy. We begin by focusing on the most variable and distinctive clearly clastic inputs. At the base of the Pahrump Hills, 15 wt% of the Confidence Hills drill sample is primary detrital olivine and pyroxene and an additional 7.6% is Fe, Mg-phyllosilicates that likely form from chemical breakdown of primary igneous components. At the other end of the section at Marias Pass, the Buckskin sample is composed of 20% crystalline silica, mostly in the form of tridymite (See Figure 5.1 for locations). This unusual form of silica is not known to form outside of high-temperature, low-pressure conditions, so it is interpreted as evidence for silicic volcanism in the source region [*Morris et al.*, submitted]. The tridymite is thought to be detrital clastic input rather than volcanic ash fallout because there is no change in the laminations in the Buckskin region, so there is no sedimentological evidence for volcanic ash. Furthermore, larger proportions of plagioclase would be expected with ash fallout but the Al_2O_3 in the Marias Pass region is a limiting factor [*Morris et al.*, submitted]. The two drilled samples between Confidence Hills and Marias Pass have intermediate compositions for these detrital components; mafic

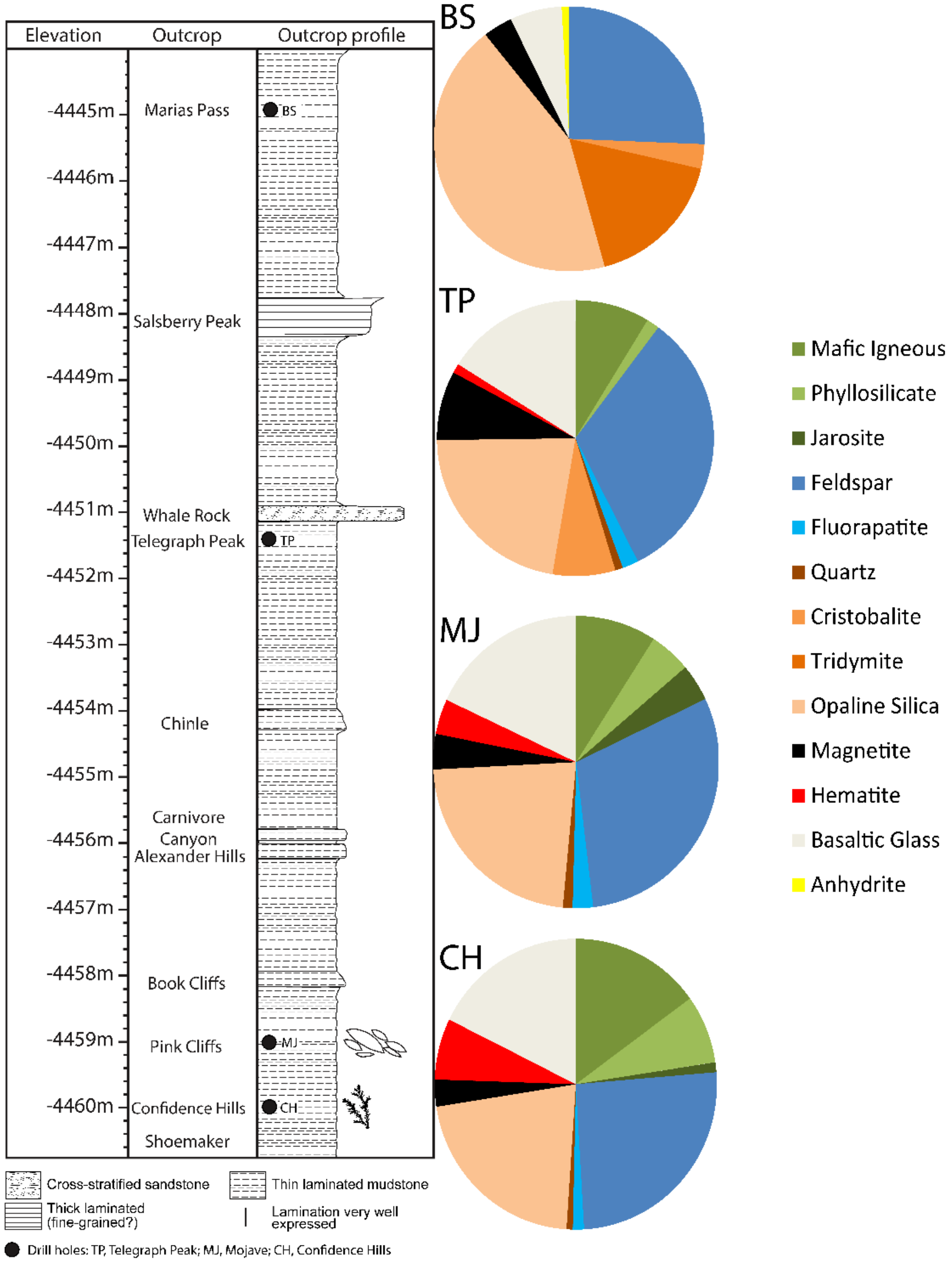

Figure 5.13 Mineralogy of Murray Formation Drilled Samples
Pie charts showing CheMin data for each of the four drill holes in the Murray formation next to a strat column showing sample locations. ‘Mafic Igneous’ category includes olivine and pyroxene components. ‘Feldspar’ category includes plagioclase and sanidine components. Green colors are related to mafic source clastic input, orange colors are related to silica source clastic input. Blue feldspar is clastic from both sources. Light-colored amorphous material and black/red iron oxides are chemical inputs [modified from *Rampe et al.*, in prep.].

igneous minerals and phyllosilicates decrease upsection from 22.6 wt% to 13.8 wt% to 8.7 wt% to 0 wt %, while quartz + cristobalite + tridymite increase from 0.7 wt% to 1.1 wt% to 8.2 wt% to 20.1 wt% (Figure 5.13) [*Rampe et al.*, in prep.].

Other igneous components do not trend as clearly. Feldspar does not show a clear trend with elevation and makes up 25-32 wt% of each sample, but it would be expected to be a major component in both mafic igneous and silicic igneous sources. Fluorapatite is present at 1.3-2.3 wt% levels in the lower three drill holes but absent (or below detection limit) at Buckskin. Hematite decreases upsection while magnetite increases, but while some iron oxides are likely in detrital mafic igneous minerals, these may be masked by authigenic iron oxide production. Jarosite is not a detrital igneous component, but could form from minor amounts of oxidizing fluids reacting with detrital pyrite or pyrrhotite [*Fischer*, 2016]. Jarosite is present at the lower three drill holes at the 1-4 wt% level. There is also a significant amount (~5-15 wt%) of amorphous material at each drill site, in addition to the high-SiO_2 amorphous material, which could be detrital or authigenic, is present at every drill site sampled by *Curiosity*, and is not well-understood [*Dehouck et al.*, 2014].

Based on the mineralogy of the major detrital igneous components, there must be a change in the source for the Murray formation in the 20 meters of elevation between the base of the Pahrump Hills, where primary mafic igneous components dominate the clastic input, and Marias Pass, where products of silicic volcanism, including tridymite and plagioclase, dominate the clastic input (Figure 5.13). Geochemical data for the same 20 m section show steadily decreasing trends upsection in Zn, Ni, MnO, and Al_2O_3 (Figure 5.10). Other elements do not trend with elevation, although most elements are depleted at Buckskin/Marias Pass, except that SiO_2, TiO_2, P_2O_5, SO_3, and K_2O are enriched (Figure 5.11). The steady depletion of Zn, Ni, MnO, and Al_2O_3 parallels the decreasing influence of the source that contributes primary mafic igneous components to the lower portion of the Pahrump Hills, so it is possible that these elements are primarily controlled by clastic input. An alternative hypothesis, proposed by [*Rampe et al.*, in prep.], is that these elements are concentrated by acid-sulfate groundwater diagenesis. Some key points highlighted by those authors are that: Ni is known to move in diagenetic fluids, it is highly concentrated in the $MgSO_4$ dendrites at the base of the Pahrump Hills, the concentrations of Ni and Zn at the base of Pahrump Hills are up to 6 times higher than average crustal compositions, and the presence of jarosite implies fluids with pH < 4. High concentrations of trace elements in mudstones are possible or even common because these elements are typically in extremely fine-grained minerals and can be transported in suspension [*Russell*, 1937; *Whitmore et al.*, 2004]. We agree that Ni must be mobilized in diagenetic fluids and Zn could be, but argue that the fluids that move Ni may be local and are unlikely to extend through 20 m of stratigraphy without disrupting the mm-scale laminations. It would be particularly challenging to dissolve and transport Al_2O_3 without disturbing the fine-scale laminations or dissolving primary basaltic components such as olivine. While we recognize that Al_2O_3 is an odd tracer component for a mafic source rock because it is typically present in felsic minerals, the trend in Al_2O_3 and its coupling with Ni, Zn, MnO, and Cr_2O_3 (Figures 5.9, 5.10) imply that it is significantly more abundant in the mafic source rock, where it may also be in the phyllosilicate and amorphous components, than the silicic source rock. Indeed, Morris et al. [submitted] note that Al_2O_3 is the limiting component in the crystalline component for the Buckskin sample, which is only 40% crystalline. Overall, the undisturbed mm-scale laminations imply that the main geochemical controls are source area and authigenic sediment precipitation and/or early diagenetic cementation, and the geochemistry of Zn, Ni, MnO, and Al_2O_3 shift in parallel with a known shift in source area from one of mafic igneous rocks to silicic igneous rocks, so we argue it is simplest to assume these trends in geochemistry are related to the mafic igneous source area.

In the Murray formation above Marias Pass, the concentrations of geochemical components are scattered around the average from the trends below Marias Pass (Figure 5.9). This scatter likely reflects more variable mixing between sources from all around the Murray lake, such that the overall lake compositions reflect the average composition of the regional watershed area.

5.5.2.4 Chemical Inputs to the Murray Formation

There are a number of authigenic and/or diagenetic minerals in the Murray formation that reveal information about the water chemistry through time. From CheMin, these include phyllosilicates, magnetite, hematite, jarosite, opaline silica, other amorphous material, and anhydrite [*Rampe et al.*, in prep.; *Morris et al.*, submitted]. One additional mineral based on APXS correlations over the dendrites is $MgSO_4$, correlated with Ni [*VanBommel et al.*, 2016]. Sources and implications for each of these minerals are considered here.

The presence of phyllosilicates in the lower two drill holes in the Pahrump formation is correlated with higher percentages of primary mafic igneous minerals olivine and pyroxene. These phyllosilicates likely form from those primary mafic minerals, and could be authigenic, like the phyllosilicates in the Sheepbed unit, which implies alkaline to neutral pH lake chemistry [*Grotzinger et al.*, 2014; *Vaniman et al.*, 2014], or they might be detrital, in which case they formed higher in the watershed and were carried into the lake with the primary igneous minerals. In either case, the phyllosilicates have been preserved along with the primary igneous minerals, so lake and groundwater chemistries must not have been too acidic or otherwise caustic to these minerals. Phyllosilicates are not present at Telegraph Peak, indicating that there may have been a shift in lake chemistry, less time for authigenesis, a shift in the detrital input, or diagenetic degradation of phyllosilicates, although the presence of olivine in this drill hole argues against significant alteration [*Golden et al.*, 2005].

Significant amounts of iron oxides in the lower three drill holes (7.8+ wt%), and the anti-correlation between FeO_T and Al_2O_3 (Figure 5.11d) when Al_2O_3 is correlated with mafic elements Zn, Ni, MnO, and Cr_2O_3 (Figures 5.9, 5.11c), imply that, chemically, iron is concentrated independently from igneous detrital minerals. Therefore, iron oxides are likely not only detrital but are perhaps better explained as a chemical precipitate in the lake or pore fluids. This is supported by orbital observations of a hematite-enriched stratigraphic layer at a few tens of meters higher elevation [*Fraeman et al.*, 2013]. The redox state of the iron oxides shifts from more oxidized hematite at the base of the section to more reduced magnetite at Buckskin in Marias Pass. This shifting iron chemistry could reflect changes or stratification in the redox state in the lake itself [*Hurowitz et al.*, 2016] and/or could be related to oxidation of magnetite by diagenetic fluids [*Hurowitz et al.*, 2010].

The 1-4 wt% jarosite detected in the lower three drill holes is most simply explained as the result of oxidation of detrital pyrite or pyrrhotite associated with the mafic igneous source [*Jambor et al.*, 2000]. The formation of jarosite requires pH < 4 [*Driscoll and Leinz*, 2005], but this low pH can be extremely localized around the sulfide grains [*Fischer*, 2016 pers. communication]. The presence of jarosite is used by [*Rampe et al.*, 2016; *Rampe et al.*, in prep.] as evidence for acid-sulfate groundwater diagenesis, but broad permeation and reaction with acidic fluids is inconsistent with the presence of fluorapatite, olivine, and pyroxene, and the enriched P_2O_5, so we prefer to assume localized acidic fluids on the grain-scale or micro-fracture scale [*Hurowitz et al.*, 2010; *Fischer*, 2016 pers. communication].

Significant amounts of high-SiO_2 amorphous material, modeled by CheMin as rhyolitic glass or opal-A, are present in all of the drilled samples in the Murray formation, and increase upsection. This could be detrital rhyolitic glass associated with the silicic volcanism [*Morris et al.*, submitted], an authigenic silica gel precipitate in the lake itself [*Ramseyer et al.*, 2013; *Hurowitz et al.*, 2016], a combination of these, or residual silica from acid weathering [*Rampe et al.*, 2016; *Rampe et al.*, in prep.]. We do not think acid-sulfate weathering is reasonable based on chemical and sedimentological evidence listed previously, but we cannot distinguish between rhyolitic glass and silica gel precipitate as the origin for the high-SiO_2 amorphous material. It is likely that the silicic volcanic unit that sourced the detrital tridymite has rhyolitic glass associated with it, and this glass could weather in place to produce silica-enriched water, or be carried directly into the lake as detritus, so these two options are not mutually exclusive. The increase in overall SiO_2 in the samples with the most SiO_2 amorphous gel (at Buckskin) is correlated with increasing TiO_2, P_2O_5, and K_2O. These elements are not known to typically travel together in weathering or diagenetic fluids [*Stumm and Morgan*, 2012], and their chemical form is not known within the amorphous component, but they are consistently elevated in the Murray formation and associated with the amorphous component (Figure 5.6, 5.10) [*Rampe et al.*, in prep.; *Morris et al.*, submitted], and they are all incompatible elements in magma and may be enriched in silicic volcanics as a result. Furthermore, these elements are enriched in the SiO_2-rich fracture-associated halo zones in the Stimson unit, which must form due to fluid movement through the fractures, and that fluid may originate in the Murray or also affect the Murray formation (Figure 5.12). Therefore, while the chemical form and mechanism for transporting these elements is not understood, it seems that in both the Murray and Stimson units, there is a high-SiO_2 amorphous material associated with elevated P_2O_5, TiO_2, and K_2O that can be transported in fluids.

The other amorphous material was modeled by CheMin as basaltic glass and ferrihydrite, and generally decreases in abundance upsection. Similar amorphous materials, making up 15-30 wt% of each sample, have been observed at all previous drill locations [*Bish et al.*, 2013; *Dehouck et al.*, 2014; *Vaniman et al.*, 2014]. This other amorphous material may be associated with the mafic igneous detritus, silicic detritus, eolian dust, and/or destabilization of other minerals in Martian climatic conditions [e.g. *Vaniman et al.*, 2004].

Anhydrite is present in the Buckskin sample, and is likely associated with the late-stage $CaSO_4$ veins found in every unit investigated by *Curiosity* [*Nachon et al.*, 2014]. It is interesting that anhydrite is detected in the Buckskin sample but not other drill holes in the Murray, and $CaSO_4$ veins are also associated with high-SiO_2 fracture halos in the Stimson unit; it is possible that the high SiO_2 amorphous material concentrated at these sites is mechanically weaker than other parts of the formation, and so more frequently exploited by late-stage fracturing.

Finally, possible $MgSO_4$ salts have been detected based on APXS rasters over dendritic diagenetic features at the base of Pahrump Hills (Figure 5.3c) [*VanBommel et al.*, 2016]. Lack of evidence for mudcracks, intraclasts, or ripples around these features has led multiple authors to conclude that these likely formed in the subsurface [*Rampe et al.*, 2016; *VanBommel et al.*, 2016; *Rampe et al.*, in prep.]. $MgSO_4$ salts are extremely soluble in water, and so must be deposited when water activity is very low [*Stumm and Morgan*, 2012]. This could happen due to evaporation or freezing of groundwater in late diagenesis [e.g. *Tosca et al.*, 2008]. The concentration of Mg and SO_3 in the Murray formation are anticorrelated with the concentration of SiO_2, which could simply relate to the porosity of the mudstone at the time of $MgSO_4$ deposition (Figure 5.11a, b).

Overall, chemical precipitates make up ~40-60 wt% of the Murray formation. These are dominated by high-SiO_2 amorphous material associated with elevated TiO_2, P_2O_5, and K_2O, that is likely related to other products of the silicic volcanism that produced tridymite and is remobilized in later fluids that affect Stimson. Phyllosilicates at the base of the Murray indicate that for some time the lake had circum-neutral pH, and that these minerals were preserved throughout diagenesis. Magnetite and hematite indicate Fe-rich pore fluids, and hematite and jarosite indicate some oxidizing and acidic diagenetic fluids. $MgSO_4$ dendritic features reveal where diagenetic water activity became very low, likely due to freezing or evaporation, and available pore space was filled.

5.5.3 Eolian

Eolian deposits integrate windblown particles eroded from regional or even global areas [*Yen et al.*, 2005]. The Stimson formation composition reflects this compositional averaging; the geochemistry is very consistent and matches estimates of average Mars crustal composition quite well (Figure 5.6) [*Taylor and McLennan*, 2009]. Variability between bedrock measurements is low and is not systematic (Figure 5.6, 5.12). SO_3 is slightly elevated in the Stimson compared to other units; this could relate to sulfate cements or dust trapped between particles on the surfaces used for compositional measurements. Notably compared to other units in Gale crater, the Stimson has average Mars crust values for K_2O. This could potentially indicate that the source of high K_2O was no longer available for surface erosion when the Stimson formed, or the Stimson could be averaging crust components over such a large area that the signature of the high-K_2O source is diluted out.

The only portions of the Stimson formation with distinctive compositions in APXS are the light-toned fracture halos (Figure 5.3e). Fracture halos form when fluid moving through a fracture in the rock permeates some distance into the rock itself on either side of the fracture and precipitates additional cements or dissolves or reacts with rock components. This requires that the rock is already lithified, but has some permeability. Fracture halos in the Stimson are characterized by elevated SiO_2, TiO_2, P_2O_5, and SO_3, constant K_2O and CaO, and associated dilution of all other chemical components. These fracture zones in the rock are frequently exploited as mechanically weaker zones by $CaSO_4$

veins, so elevated SO_3 and CaO are likely related to these late-stage fracture fills. The elevated SiO_2, TiO_2, P_2O_5, and K_2O is extremely similar to the signature of the high-SiO_2 amorphous material in the Murray formation. While, again, the mineral form of these elements and the mobilization of them together is not well understood, it is clear that they are deposited together by a fluid that passed through the Stimson. Alternative options would be for the fluid to dissolve all other chemical components in the Stimson (although the chemistry of a fluid that would leave P_2O_5 and K_2O behind while mobilizing Al_2O_3 and FeO is unclear) and/or there could be multiple fluids to deposit these chemicals separately, but the consistency of the compositional signature in the Bradbury group and in each measured fracture halo argues for co-deposition of these elements in some amorphous form.

5.6 Summary

The geochemical diversity of rock formations in Gale crater is strongly related to their depositional environments. The Bradbury group of fluvio-deltaic sandstones have the most geochemical variability of the formations measured so far in Gale crater, and this diversity is dictated by mineral sorting trends between different grain size fractions during river transport. The Murray mudstone formation has some geochemical variability due to shifting compositions of clastic sources between mafic and silicic igneous rocks, and some related to the balance between clastic input and chemical input into the lake. The Stimson eolian formation integrates source rocks over the largest area and as a result has a very well-constrained composition that is very similar to average Mars crust. Understanding of the depositional environment is critical to interpretation of geochemical trends.

Chapter 6

Summary and Implications

6.1 Introduction

Detailed study of rover-scale sedimentary geology and petrology allows us to constrain details about the igneous evolution of the source rocks outside Gale, early climate on Mars, and cementation of sedimentary rocks on Mars. Here we summarize key implications and future directions of this work for each of these areas of study.

6.2 Igneous Evolution

Mars lacks plate tectonics and does not have extensive continental crust, so the degree of igneous differentiation on Mars is expected to be much lower than on Earth. In line with this assumption, most of the rock samples observed by previous rover missions and in meteorites have been basaltic [*Team*, 1997; *Clark et al.*, 2005; *Gellert et al.*, 2006; *Papike et al.*, 2009], and the dust on Mars is basaltic and homogeneous on a global scale [*Yen et al.*, 2005]. However, spectroscopic observations from orbiters have shown that there is significant compositional variability in bedrocks exposed at the surface [*Ehlmann and Edwards*, 2014], and regions where more evolved igneous rocks may be present have been identified [*Christensen et al.*, 2005; *Wray et al.*, 2013]. It has also been hypothesized that melts from large impacts on Mars could be more differentiated [e.g. *Therriault et al.*, 2002]. Several recent papers have argued for the presence of granitic or very evolved magma flows in various regions on Mars, based on orbital spectroscopy and/or rover observations [*Stolper et al.*, 2013; *Wray et al.*, 2013; *Sautter et al.*, 2015; *Sautter et al.*, 2016].

The Gale crater sedimentary basin has collected rocks by fluvial and eolian processes from a significant area around the crater and likely a significant depth into the crust (~5 km). The bedrock around Gale crater is Noachian in age, and, since the crater is sitting on the dichotomy boundary, sources include rocks from both the Northern lowlands and the Southern highlands. Comparisons of Gale to other similar complex craters indicate that the original crater was deeper and had a smaller diameter, so slumping of the crater walls has likely contributed significant sediment to the filling of Gale [*Grotzinger et al.*, 2015], implying that units up to 5 km below the surface likely contributed as source rocks for the sedimentary rocks in Gale. This wide sampling of source rocks, integrated into the sedimentary rocks in Gale, allows some assessment of the degree of igneous diversity in the Gale crater region.

The work in this thesis shows that the geochemical diversity of the rocks sampled by the Alpha-Particle X-ray Spectrometer (APXS) on *Curiosity* can be accounted for with only a limited degree of igneous differentiation. The Bradbury group compositions are consistent with breakdown and sorting of a basalt or a basaltic andesite provenance with plagioclase phenocrysts. The localized high sanidine input could be sorted from another basaltic region, and only requires that alkali elements are not evenly distributed in Martian magmas (Chapter 4). The Stimson formation is consistent with average Mars crustal basaltic sources. The Murray formation is mostly distinctive because of authigenic mineral production in the lake and diagenetic minerals formed from the groundwater (Chapter 5). The Murray has some distinctive samples with particularly high silica, but with bulk chemistry alone these look similar to fracture-associated haloes in the Stimson, and can therefore be explained to some degree by fluids. Overall, based on bulk chemistry and textures, we have not seen compositions that require significant igneous differentiation processes on Mars. However, evidence from the CheMin instrument, specifically the identification of tridymite—a high-temperature, low pressure polymorph of silica—at the Buckskin sample, suggests that there could be felsic igneous rocks in the region contributing to Gale [*Morris et al.*, submitted], which will hopefully be better understood as we continue to investigate the Murray formation and formation mechanisms for tridymite.

6.3 Climate

There is ongoing debate about the climate of early Mars, particularly focused around the questions of whether or not the planet was warm enough to sustain surface water for geologically significant periods of time and whether the water was mostly liquid or ice. Early observations from the *Curiosity* rover at the Sheepbed mudstone in Yellowknife Bay indicated that there was water present for enough time to deposit and lithify 1.5 m of mudstone (Chapter 3) [*Grotzinger et al.*, 2014; *Siebach et al.*, 2014; *Stack et al.*, 2014] and that the lack of evidence for chemical weathering indicated that the climate was likely arid and potentially cold [*McLennan et al.*, 2014]. This work has shown that the absence of evidence for chemical weathering extends through at least 60 m of the Bradbury group stratigraphy, indicating that the climate remained cold and arid enough to prevent chemical weathering in the northern rim source for the Bradbury group throughout the observed section (Chapter 4). The mineral sorting trends within the Bradbury group are comparable to sorting trends in rocks that have been crushed in a lab [*Fedo et al.*, 2015], or comminuted glacially and sorted in glacial streams [*Nesbitt and Young*, 1996; *von Eynatten et al.*, 2012], so the rivers that fed the lakes in Gale may have also been glacial streams emerging from the northern rim of the crater, or rocks broken by impact processes and rounded by transport in cold floods. The Bradbury group observations alone do not require consistent water flow, and likely formed from episodic flows, similar to arid streams on Earth.

Curiosity's observations of the Bradbury group and Murray mudstone have been interpreted to show that individual lakes were stable on the surface of Mars for minimum durations of 100 to 10,000 years due to the thickness of the deposit, the laminations, and the lack of evidence for mudcracks or other indicators of evaporation or surface exposure throughout the observed Murray unit [*Grotzinger et al.*, 2015]. Work in Chapter 5 indicates that while the lake may be consistently filled with water, the fluvial sources of the water are likely more intermittent and may transition from one side of Gale crater to the other side. Additionally, the Murray lake has significant amounts of dissolved ions, causing authigenic mineral precipitation and indicating that chemical weathering has occurred in some region around Gale crater, perhaps either the central peak of the crater or the southern wall. These dissolved ions must be present in the lake at the same time as the Bradbury group contributes to the lake, but the Bradbury group shows no evidence for chemical weathering and so they must be derived from other sources entering the lake. This evidence for localized chemical weathering may indicate a localized (elevation-dependent?) warmer climate, weathering of rocks influenced by hydrothermal processes associated with impact melts, or distinctive mineralogy more susceptible to chemical weathering processes.

6.4 Cementation

While sediment production on Mars was established from early Mariner 9 imagery [*McCauley et al.*, 1972; *McCauley,* 1973], sedimentary rocks were not discovered until nearly thirty years later [*Malin and Edgett,* 2000]. Part of the reason for this lag is that the process of sedimentary rock lithification and exposure involves compaction, cementation, and uplift—processes related to plate tectonics, which does not occur on Mars, and liquid groundwater, which is not present on Mars today. The first sedimentary rocks observed by a rover on Mars were the eolian sandstones of the Burns formation, which were deposited by the wind, cemented by evaporation of acidic sulfate-rich groundwater, and exposed by impact processes [*Grotzinger et al.*, 2005; *McLennan et al.*, 2005]. Groundwater evaporation and salt deposition is one mechanism for lithifying sedimentary rocks near the surface, and since the effects of this process are visible on Mars even at orbital scales (e.g. Chapter 2), salt deposition was considered to be the most likely mechanism for cementing other sedimentary rocks on Mars as well. However, *Curiosity* data paints a very different picture of materials involved in cementation than expected based on orbital data.

Curiosity's observations of sandstones and conglomerates show that these are well-cemented sedimentary rocks with very low porosity, and it is frequently difficult to distinguish grains from cements (Chapter 4) [*Williams et al.*, 2013; *Siebach and Grotzinger,* 2014b]. In a few cases, erosion-resistant structures or fracture fills have allowed identification of the precipitated cement that filled them, but most of these were localized fracture fills that formed during diagenesis. These include: iron-oxide cements in a few float rocks near the landing site [*Blaney et al.*, 2014; *Schmidt et al.*, 2014], slightly

Mg-enriched typical Mars basalt composition isopachous cements in the Sheepbed raised ridges and nodules (Chapter 3) [*Léveillé et al.*, 2014; *Siebach et al.*, 2014; *Stack et al.*, 2014], MnO and Zn-enriched fracture fill at the Stephen target near Windjana [*Lasue et al.*, 2016; *Lanza et al.*, submitted], $MgSO_4$ dendritic concretions at the base of the Murray, and ubiquitous late-stage CaSO4 fracture fills [*Nachon et al.,* 2014; *Kroynak et al.*, 2015]. Each of these distinctive fracture filling cements results from an interesting fluid composition that precipitated the cement, but these cement compositions, and likely the fluids that created them, are all restricted to small local areas or late-stage fractures and are not widespread through the observed rock units. Instead, the observed sandstones and conglomerates in the Bradbury group and Stimson formation have compositions that are consistent with the compositions of the basaltic fragments that they are composed of, without any indication of chemical weathering or additional cements (Chapters 4, 5).

The cementation of the Stimson sandstone formation is particularly enigmatic. The sandstone is an eolian deposit sitting above an unconformity that appears to follow the modern shape of Mount Sharp (Figure 6.1)[*Watkins et al.*, 2016], implying that the Murray formation lake deposits had already been cemented and significantly eroded when this eolian sand was deposited. The rock is so well-cemented that there is almost no visible porosity, even on broken rock surfaces (Figure 6.2) [*Siebach and Grotzinger*, 2014b]. To achieve such low visible porosity, up to 10-20% of the rock volumetrically should be full of cement (based on an assumption of closest packing). Significant grain compaction is not observed and would be unlikely due to reduced gravity on Mars [*Grotzinger et al.*, 2015], so the cement must be deposited by fluids. Compositionally, however, the sandstone is very homogeneous and matches the composition of average Mars crust, which is expected for the sediment itself, which integrates eroded particles from regional surfaces, but does not explain the cementing component (Chapter 5). Mineralogy of the unit shows only primary basaltic minerals and amorphous material with a composition similar to basaltic glass. If the cementing fluids dissolved components of the rock and migrated, more soluble cations would be depleted. If, alternately, cementing fluids carried dissolved components from other sources, some cations would be enriched relative to average Mars crust. Based on the observed evidence, we are forced to conclude that the cement is an x-ray-amorphous

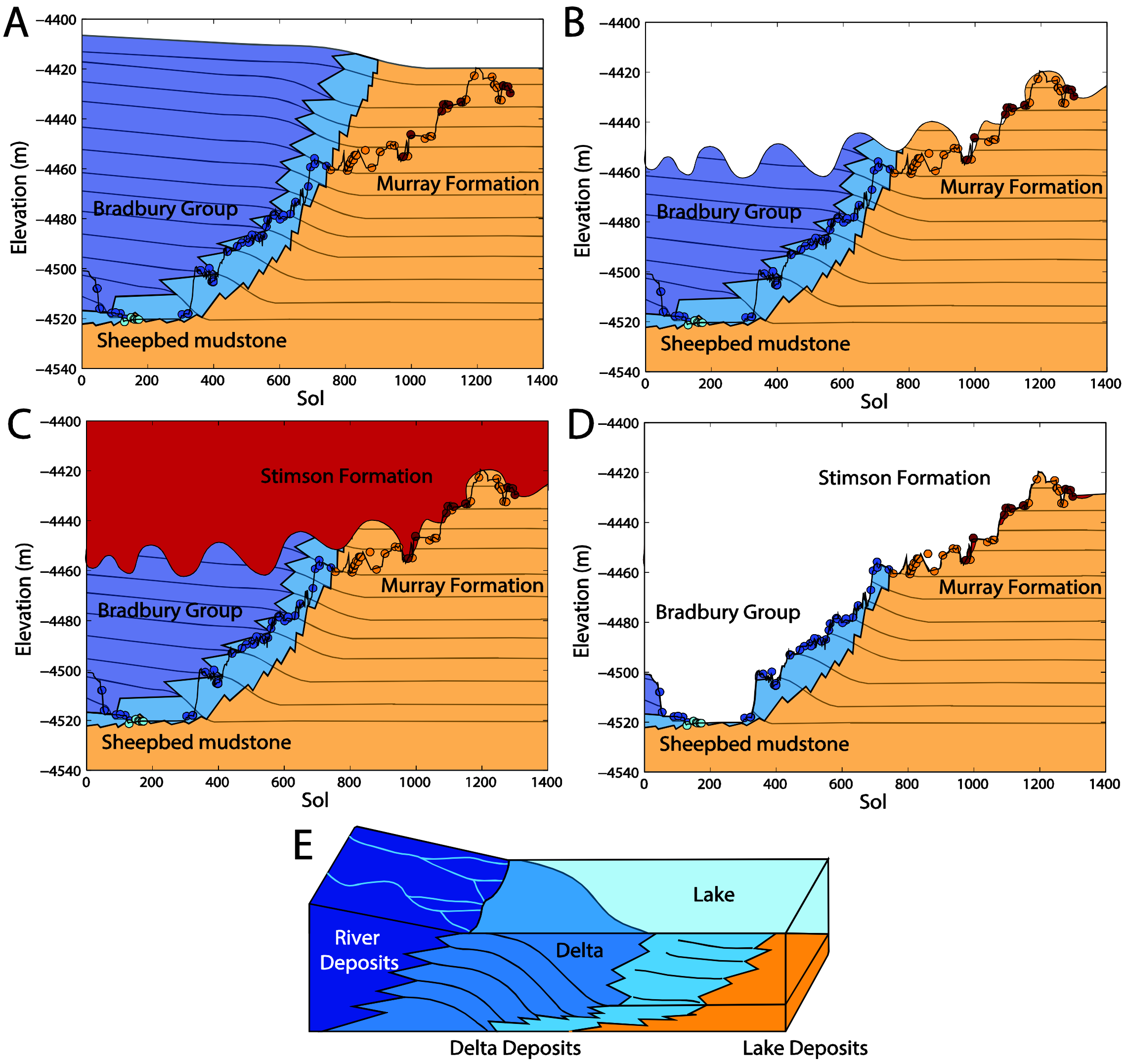

Figure 6.1 Schematic of Depositional Sequence in Gale Crater
Parts A-C shows the rover traverse in sol (i.e. distance traveled) vs. elevation (i.e. stratigraphic position) plots, with the APXS analyses plotted as circles and the key depositional units highlighted. Part E is a reference for the depositional facies in a delta system, modified from NASA/JPL. Part A shows the deposition of the Bradbury and Murray groups as a fluvio-deltaic system. Part B represents the initial erosion event that created the paleotopography that the Stimson sandstone formation (Part C) was unconformably deposited over. Part D represents the modern erosion, exposing all units along the rover traverse.

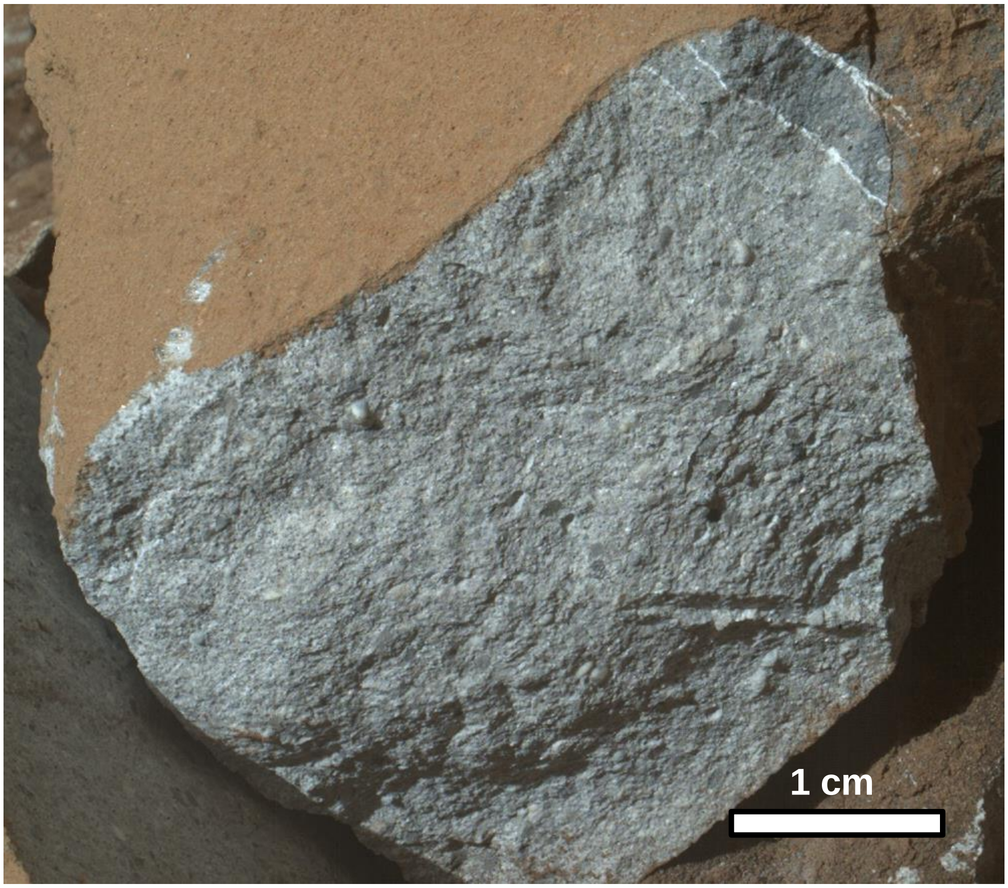

Figure 6.2 MAHLI Image of Stampriet Target in Stimson Formation
This is a 5 cm standoff image taken on sol 1344 of the Stampriet target, a broken rock in the Stimson sandstone that shows the lack of porosity in that formation.

precipitate formed in place from dissolved components of the sandstone. The cement may be x-ray amorphous because the nucleated crystals are too small for x-ray detection or because desiccation cycling under Mars climate conditions can cause some materials to become amorphous [*Vaniman et al.*, 2004]. This type of amorphous cement also explains why the Bradbury group sandstones and conglomerates also lack clear evidence for a distinctive cementing component. More detailed characterization of this amorphous cement depends on our ability to model the compositions of the amorphous components on Mars and better understand x-ray amorphous cements on Earth.

REFERENCES

Alvarez, L. W., W. Alvarez, F. Asaro, and H. V. Michel (1980), Extraterrestrial Cause for the Cretaceous-Tertiary Extinction, *Science*, *208*(4448), 1095-1108, doi: 10.1126/science.208.4448.1095.

Amieux, P., P. Bernier, R. Dalongeville, and V. Demedwecki (1989), Cathodoluminescence of Carbonate-Cemented Holocene Beachrock from the Togo Coastline (West-Africa) - an Approach to Early Diagenesis, *Sedimentary Geology*, *65*(3-4), 261-272, doi: 10.1016/0037-0738(89)90028-6.

Anderson, D. L., W. F. Miller, G. V. Latham, Y. Nakamura, M. N. Toksoz, A. M. Dainty, F. K. Duennebier, A. R. Lazarewicz, R. L. Kovach, and T. C. D. Knight (1977), Seismology on Mars, *Eos T Am Geophys Un*, *58*(8), 828-828.

Anderson, R. B., and J. F. Bell (2010), Geologic mapping and characterization of Gale Crater and implications for its potential as a Mars Science Laboratory landing site, *The Mars Journal*, *5*, 76-128, doi: 10.1555/mars.2010.0004.

Arvidson, R. E., et al. (2014), Ancient Aqueous Environments at Endeavour Crater, Mars, *Science*, *343*(6169), doi: 10.1126/science.1248097.

Bakalowicz, M. J., D. C. Ford, T. E. Miller, A. N. Palmer, and M. V. Palmer (1987), Thermal Genesis of Dissolution Caves in the Black Hills, South-Dakota, *Geological Society of America Bulletin*, *99*(6), 729-738, doi: 10.1130/0016-7606(1987)99<729:Tgodci>2.0.Co;2.

Baker, M. B., and J. R. Beckett (1999), The origin of abyssal peridotites: a reinterpretation of constraints based on primary bulk compositions, *Earth Planet Sc Lett*, *171*(1), 49-61, doi: 10.1016/S0012-821x(99)00130-2.

Baker, V. R., and D. J. Milton (1974), Erosion by Catastrophic Floods on Mars and Earth, *Icarus*, *23*(1), 27-41, doi: 10.1016/0019-1035(74)90101-8.

Banner, J. L., and G. N. Hanson (1990), Calculation of Simultaneous Isotopic and Trace-Element Variations during Water-Rock Interaction with Applications to Carbonate Diagenesis, *Geochim Cosmochim Ac*, *54*(11), 3123-3137, doi: 10.1016/0016-7037(90)90128-8.

Bauerman, H. (1885), Report on the geology of the country near the forty-ninth parallel of North latitude West of the Rocky Mountains. Report of Progress 1882-1884, Part B, Geological Survey of Canada (1885), pp. 1-42.

Belderson, R. H., N. H. Kenyon, and A. H. Stride (1978), Local Submarine Salt-Karst Formation on Hellenic Outer Ridge, Eastern Mediterranean, *Geology; Geology*, *6*(12), 716-720, doi: 10.1130/0091-7613(1978)6<716:Lssfot>2.0.Co;2.

Bell, J., A. Godber, M. Rice, A. Fraeman, B. Ehlmann, W. Goetz, C. Hardgrove, D. Harker, J. Johnson, and K. Kinch (2013), Initial Multispectral Imaging Results from the Mars Science Laboratory Mastcam Investigation at the Gale Crater Field Site, paper presented at 44th Lunar and Planetary Science Conference, LPI, Houston, TX, Abs. #1417.

Bethke, C. M. (1985), A Numerical-Model of Compaction-Driven Groundwater-Flow and Heat-Transfer and Its Application to the Paleohydrology of Intracratonic Sedimentary Basins, *J Geophys Res-Solid*, *90*(Nb8), 6817-6828, doi: 10.1029/JB090iB08p06817.

Bibring, J. P., et al. (2005), Mars surface diversity as revealed by the OMEGA/Mars Express observations, *Science*, *307*(5715), 1576-1581, doi: 10.1126/science.1108806.

Bibring, J. P., et al. (2006), Global mineralogical and aqueous mars history derived from OMEGA/Mars Express data, *Science, 312*(5772), 400-404, doi: 10.1126/science.1122659.

Bish, D., et al. (2014), The first X-ray diffraction measurements on Mars, *IUCrJ*, *1*(Pt 6), 514-522, doi: 10.1107/S2052252514021150.

Bish, D. L., et al. (2013), X-ray Diffraction Results from Mars Science Laboratory: Mineralogy of Rocknest at Gale Crater, *Science*, *341*(6153), doi: 10.1126/science.1238932.

Bishop, J. W., D. Y. Sumner, and N. J. Huerta (2006), Molar tooth structures of the Neoarchean Monteville Formation, Transvaal Supergroup, South Africa. II: A wave-induced fluid flow model, *Sedimentology*, *53*(5), 1069-1082, doi: 10.1111/j.1365-3091.2006.00802.x.

Blake, D., et al. (2012), Characterization and Calibration of the CheMin Mineralogical Instrument on Mars Science Laboratory, *Space Sci Rev*, *170*(1-4), 341-399, doi: 10.1007/s11214-012-9905-1.

Blaney, D. L., et al. (2014), Chemistry and texture of the rocks at Rocknest, Gale Crater: Evidence for sedimentary origin and diagenetic alteration, *J Geophys Res-Planet*, *119*(9), 2109-2131, doi: 10.1002/2013je004590.

Bryan, W. B., L. W. Finger, and F. Chayes (1969), Estimating proportions in petrographic mixing equations by least-squares approximation, *Science*, *163*(3870), 926-927, doi: 10.1126/science.163.3870.926.

Burr, D. M., P. A. Carling, and V. R. Baker (Eds.) (2009), *Megaflooding on Earth and Mars*, 319 pp., Cambridge University Press, New York.

Burst, J. F. (1965), Subaqueously Formed Shrinkage Cracks in Clay, *Journal of Sedimentary Petrology*, *35*(2), 348-353.

Calver, C. R., and P. W. Baillie (1990), Early Diagenetic Concretions Associated with Intrastratal Shrinkage Cracks in an Upper Proterozoic Dolomite, Tasmania, Australia, *Journal of Sedimentary Petrology*, *60*(2), 293-305.

Campbell, J. L., G. M. Perrett, R. Gellert, S. M. Andrushenko, N. I. Boyd, J. A. Maxwell, P. L. King, and C. D. M. Schofield (2012), Calibration of the Mars Science Laboratory Alpha Particle X-ray Spectrometer, *Space Sci Rev*, *170*(1-4), 319-340, doi: 10.1007/s11214-012-9873-5.

Canfield, D. E. (2005), THE EARLY HISTORY OF ATMOSPHERIC OXYGEN: Homage to Robert M. Garrels, *Annual Review of Earth and Planetary Sciences*, *33*(1), 1-36, doi: 10.1146/annurev.earth.33.092203.122711.

Carr, M. H. (1987), Water on Mars, *Nature*, *326*(6108), 30-35, doi: 10.1038/326030a0.

Carrapa, B., A. Di Giulio, and J. Wijbrans (2004), The early stages of the Alpine collision: an image derived from the upper Eocene–lower Oligocene record in the Alps–Apennines junction area, *Sedimentary Geology*, *171*(1-4), 181-203, doi: 10.1016/j.sedgeo.2004.05.015.

Cawood, P. A., A. A. Nemchin, M. Freeman, and K. Sircombe (2003), Linking source and sedimentary basin: Detrital zircon record of sediment flux along a modern river system and implications for provenance studies, *Earth Planet Sc Lett*, *210*(1-2), 259-268, doi: 10.1016/S0012-821x(03)00122-5.

Chesworth, W., J. Dejou, and P. Larroque (1981), The Weathering of Basalt and Relative Mobilities of the Major Elements at Belbex, France, *Geochim Cosmochim Ac*, *45*(7), 1235-1243, doi: 10.1016/0016-7037(81)90147-2.

Christensen, P. R., et al. (2005), Evidence for magmatic evolution and diversity on Mars from infrared observations, *Nature*, *436*(7050), 504-509, doi: 10.1038/nature03639.

Clark, B. C., et al. (2005), Chemistry and mineralogy of outcrops at Meridiani Planum, *Earth Planet Sc Lett*, *240*(1), 73-94, doi: 10.1016/j.epsl.2005.09.040.

Condie, K. C. (1993), Chemical Composition and Evolution of the Upper Continental-Crust: Contrasting Results from Surface Samples and Shales, *Chem.Geol.*, *104*(1-4), 1-37, doi: 10.1016/0009-2541(93)90140-E.

Cowan, C. A., and N. P. James (1992), Diastasis Cracks: mechanically generated synaeresis-like cracks in Upper Cambrian shallow water oolite and ribbon carbonates, *Sedimentology*, *39*(6), 1101-1118, doi: 10.1111/j.1365-3091.1992.tb01999.x.

Dehouck, E., S. M. McLennan, P. Y. Meslin, and A. Cousin (2014), Constraints on abundance, composition, and nature of X-ray amorphous components of soils and rocks at Gale crater, Mars, *Journal of Geophysical Research: Planets*, *119*(12), 2640-2657, doi: 10.1002/2014je004716.

Di Achille, G., and B. Hynek (2010), Ancient ocean on Mars supported by global distribution of deltas and valleys, *Nat Geosci*, *3*, 459-463, doi: 10.1038/ngeo89110.1038/NGEO891.

DiBiase, R. A., A. B. Limaye, J. S. Scheingross, W. W. Fischer, and M. P. Lamb (2013), Deltaic deposits at Aeolis Dorsa: Sedimentary evidence for a standing body of water on the northern plains of Mars, *Journal of Geophysical Research: Planets*, *118*(6), 1285-1302, doi: 10.1002/jgre.20100.

Dorobek, S. L. (1987), Petrography, geochemistry, and origin of burial diagenetic facies, Siluro-Devonian Helderberg Group (carbonate rocks), central Appalachians, *AAPG Bulletin*, *71*(5), 492-514.

Dreibus, G., and H. Wanke (1985), Mars, a Volatile-Rich Planet, *Meteoritics*, *20*(2), 367-381.

Driscoll, R., and R. Leinz (2005), Methods for synthesis of some jarosites. Techniques and Methods, pp. 9.

Duck, R. W. (1995), Subaqueous Shrinkage Cracks and Early Sediment Fabrics Preserved in Pleistocene Calcareous Concretions, *J Geol Soc London*, *152*, 151-156, doi: 10.1144/gsjgs.152.1.0151.

Edgett, K. S., et al. (2012), Curiosity’s Mars Hand Lens Imager (MAHLI) Investigation, *Space Sci Rev*, *170*(1-4), 259-317, doi: 10.1007/s11214-012-9910-4.

Ehlmann, B. L., and J. F. Mustard (2012), An in-situ record of major environmental transitions on early Mars at Northeast Syrtis Major, *Geophys Res Lett*, *39*(11), doi: 10.1029/2012gl051594.

Ehlmann, B. L., and C. S. Edwards (2014), Mineralogy of the Martian Surface, *Annu Rev Earth Pl Sc*, *42*(1), 291-315, doi: 10.1146/annurev-earth-060313-055024.

Ehlmann, B. L., and J. Buz (2015), Mineralogy and fluvial history of the watersheds of Gale, Knobel, and Sharp craters: A regional context for the Mars Science Laboratory Curiosity's exploration, *Geophys Res Lett*, *42*(2), 264-273, doi: 10.1002/2014gl062553.

Ehlmann, B. L., J. F. Mustard, S. L. Murchie, J. P. Bibring, A. Meunier, A. A. Fraeman, and Y. Langevin (2011), Subsurface water and clay mineral formation during the early history of Mars, *Nature*, *479*(7371), 53-60, doi: 10.1038/nature10582.

Ehlmann, B. L., J. F. Mustard, C. I. Fassett, S. C. Schon, J. W. Head Iii, D. J. Des Marais, J. A. Grant, and S. L. Murchie (2008a), Clay minerals in delta deposits and organic preservation potential on Mars, *Nat Geosci*, *1*(6), 355-358, doi: 10.1038/ngeo207.

Ehlmann, B. L., et al. (2008b), Orbital identification of carbonate-bearing rocks on Mars, *Science*, *322*(5909), 1828-1832, doi: 10.1126/science.1164759.

Engel, A. E., S. P. Itson, C. G. Engel, D. M. Stickney, and E. J. Cray (1974), Crustal Evolution and Global Tectonics: A Petrogenic View, *Geological Society of America Bulletin*, *85*, 842-858.

Evamy, B. (1969), The precipitational environment and correlation of some calcite cements deduced from artificial staining, *Journal of Sedimentary Research*, *39*(2), 787-793.

Fairchild, I. J., G. Einsele, and T. R. Song (1997), Possible seismic origin of molar tooth structures in Neoproterozoic carbonate ramp deposits, north China, *Sedimentology*, *44*(4), 611-636, doi: 10.1046/j.1365-3091.1997.d01-40.x.

Falkowski, P. G., and Y. Isozaki (2008), The Story of O2, *Science*, *322*(5901), 540-542, doi: 10.1126/science.1162641.

Farley, K. A., et al. (2014), In Situ Radiometric and Exposure Age Dating of the Martian Surface, *Science*, *343*(6169), doi: 10.1126/science.1247166.

Fassett, C. I., and J. W. Head (2005), Fluvial sedimentary deposits on Mars: Ancient deltas in a crater lake in the Nili Fossae region, *Geophys Res Lett*, *32*(14), doi: 10.1029/2005gl023456.

Fedo, C. M., H. W. Nesbitt, and G. M. Young (1995), Unraveling the Effects of Potassium Metasomatism in Sedimentary-Rocks and Paleosols, with Implications for Paleoweathering Conditions and Provenance, *Geology; Geology*, *23*(10), 921-924, doi: 10.1130/0091-7613(1995)023<0921:Uteopm>2.3.Co;2.

Fedo, C. M., G. M. Grant, and H. W. Nesbitt (1997), Paleoclimatic control on the composition of the Paleoproterozoic Serpent Formation, Huronian Supergroup, Canada: a greenhouse to icehouse transition, *Precambrian Res*, *86*(3-4), 201-223, doi: 10.1016/S0301-9268(97)00049-1.

Fedo, C. M., K. N. Sircombe, and R. H. Rainbird (2003), Detrital Zircon Analysis of the Sedimentary Record, *Reviews in Mineralogy and Geochemistry*, *53*(1), 277-303, doi: 10.2113/0530277.

Fedo, C. M., I. O. McGlynn, and H. Y. McSween (2015), Grain size and hydrodynamic sorting controls on the composition of basaltic sediments: Implications for interpreting martian soils, *Earth Planet Sc Lett*, *423*, 67-77, doi: 10.1016/j.epsl.2015.03.052.

Fergason, R. L., P. R. Christensen, M. P. Golombek, and T. J. Parker (2012), Surface Properties of the Mars Science Laboratory Candidate Landing Sites: Characterization from Orbit and Predictions, *Space Sci Rev*, *170*(1-4), 739-773, doi: 10.1007/s11214-012-9891-3.

Ferguson, R., T. Hoey, S. Wathen, and A. Werritty (1996), Field evidence for rapid downstream fining of river gravels through selective transport, *Geology; Geology*, *24*(2), 179-182, doi: 10.1130/0091-7613(1996)024<0179:Fefrdf>2.3.Co;2.

Filiberto, J., and A. H. Treiman (2009), Martian magmas contained abundant chlorine, but little water, *Geology; Geology*, *37*(12), 1087-1090, doi: 10.1130/g30488a.1.

Fischer, W. F. (2016), pers. communication., edited.

Fraeman, A. A., et al. (2013), A hematite-bearing layer in Gale Crater, Mars: Mapping and implications for past aqueous conditions, *Geology; Geology*, *41*(10), 1103-1106, doi: 10.1130/g34613.1.

Frank, T. D., and T. W. Lyons (1998), "Molar-tooth" structures: A geochemical perspective on a Proterozoic enigma, *Geology; Geology*, *26*(8), 683-686, doi: 10.1130/0091-7613(1998)026<0683:Mtsagp>2.3.Co;2.

Frihy, O. E. (1994), Discrimination of Accreted and Eroded Coasts Using Heavy Mineral Compositions of the Nile Delta Beach Sands, Egypt, *Sedimentology*, *41*(5), 905-912, doi: 10.1111/j.1365-3091.1994.tb01431.x.

Frihy, O. E., M. F. Lotfy, and P. D. Komar (1995), Spatial Variations in Heavy Minerals and Patterns of Sediment Sorting Along the Nile Delta, Egypt, *Sedimentary Geology*, *97*(1-2), 33-41, doi: 10.1016/0037-0738(94)00135-H.

Furniss, G., J. F. Rittel, and D. Winston (1998), Gas bubble and expansion crack origin of "molar-tooth" calcite structures in the Middle Proterozoic Belt Supergroup, western Montana, *Journal of Sedimentary Research*, *68*(1), 104-114.

Garzanti, E., S. Andò, and G. Vezzoli (2008), Settling equivalence of detrital minerals and grain-size dependence of sediment composition, *Earth Planet Sc Lett*, *273*(1-2), 138-151, doi: 10.1016/j.epsl.2008.06.020.

Gast, P. W. (1968), Trace Element Fractionation and the Origin of Tholeiitic and Alkaline Magma Types, *Geochim Cosmochim Ac*, *32*, 1057-1086.

Gellert, R., and B. C. Clark (2015), In Situ Compositional Measurements of Rocks and Soils with the Alpha Particle X-ray Spectrometer on Nasa's Mars Rovers, *Elements*, *11*(1), 39-44, doi: 10.2113/gselements.11.1.39.

Gellert, R., J. L. Campbell, K. P. L., L. A. Leshin, G. W. Lugmair, J. G. Spray, S. W. Squyres, and A. S. Yen (2009), The Alpha-Particle-X-ray-Spectrometer (APXS) for the Mars Science Laboratory (MSL) Rover Mission, paper presented at 40th Lunar and Planetary Science Conference, LPI, Houston, TX, Abs. #2364.

Gellert, R., et al. (2006), Alpha Particle X-Ray Spectrometer (APXS): Results from Gusev crater and calibration report, *J Geophys Res*, *111*(E2), doi: 10.1029/2005je002555.

Golden, D. C., D. W. Ming, R. V. Morris, and S. A. Mertzman (2005), Laboratory-simulated acid-sulfate weathering of basaltic materials: Implications for formation of sulfates at Meridiani Planum and Gusev crater, Mars, *J Geophys Res*, *110*(E12), doi: 10.1029/2005je002451.

Goldspiel, J. M., and S. W. Squyres (1991), Ancient Aqueous Sedimentation on Mars, *Icarus*, *89*(2), 392-410, doi: 10.1016/0019-1035(91)90186-W.

Golombek, M. P., W. B. Banerdt, K. L. Tanaka, and D. M. Tralli (1992), A prediction of Mars seismicity from surface faulting, *Science*, *258*(5084), 979-981, doi: 10.1126/science.258.5084.979.

Gross, J., A. H. Treiman, J. Filiberto, and C. D. K. Herd (2011), Primitive olivine-phyric shergottite NWA 5789: Petrography, mineral chemistry, and cooling history imply a magma similar to Yamato-980459, *Meteoritics & Planetary Science*, no-no, doi: 10.1111/j.1945-5100.2010.01152.x.

Grotzinger, J., and R. Milliken (2012), *The Sedimentary Rock Record of Mars: Distribution, Origins, and Global Stratigraphy*.

Grotzinger, J., et al. (2005), Stratigraphy and sedimentology of a dry to wet eolian depositional system, Burns formation, Meridiani Planum, Mars, *Earth Planet Sc Lett*, *240*(1), 11-72, doi: 10.1016/j.epsl.2005.09.039.

Grotzinger, J., et al. (2012), Mars Science Laboratory Mission and Science Investigation, *Space Sci Rev*, *170*(1-4), 5-56, doi: 10.1007/s11214-012-9892-2.

Grotzinger, J. P., et al. (2015), Deposition, exhumation, and paleoclimate of an ancient lake deposit, Gale crater, Mars, *Science*, *350*(6257), aac7575, doi: 10.1126/science.aac7575.

Grotzinger, J. P., et al. (2014), A habitable fluvio-lacustrine environment at Yellowknife Bay, Gale crater, Mars, *Science*, *343*(6169), 1242777, doi: 10.1126/science.1242777.

Grover, G., and J. F. Read (1983), Paleoaquifer and Deep Burial Related Cements Defined by Regional Cathodoluminescent Patterns, Middle Ordovician Carbonates, Virginia, *Aapg Bull*, *67*(8), 1275-1303.

Halley, R. B., and J. W. Schmoker (1983), High-Porosity Cenozoic Carbonate Rocks of South Florida - Progressive Loss of Porosity with Depth, *Aapg Bull*, *67*(2), 191-200.

Hartmann, W. K., and G. Neukum (2001), Cratering Chronology and the Evolution of Mars, *Space Sci Rev*, *96*(1-4), 165-194, doi: 10.1023/A:1011945222010.

Head, J. W., H. Hiesinger, M. A. Ivanov, M. A. Kreslavsky, S. Pratt, and B. J. Thomson (1999), Possible Ancient Oceans on Mars: Evidence from Mars Orbiter Laser Altimeter Data, *Science*, *286*(5447), 2134-2137, doi: 10.1126/science.286.5447.2134.

Hodges, K. V. (2005), 40Ar/39Ar Thermochronology of Detrital Minerals, *Reviews in Mineralogy and Geochemistry*, *58*(1), 239-257, doi: 10.2138/rmg.2005.58.9.

Hoek, J. D. (1991), A classification of dyke-fracture geometry with examples from Precambrian dyke swarms in the Vestfold Hills, Antarctica, *Geologische-Rundschau*, *80*(2), 233-248, doi: 10.1007/Bf01829363.

Horodyski, R. J. (1976), Stromatolites of the upper Siyeh limestone (middle proterozoic), belt supergroup, Glacier National Park, Montana, *Precambrian Res*, *3*(6), 517-536.

Hughes, M. G., J. B. Keene, and R. G. Joseph (2000), Hydraulic sorting of heavy-mineral grains by swash on a medium-sand beach, *Journal of Sedimentary Research*, *70*(5), 994-1004, doi: 10.1306/112599700994.

Hurowitz, J., et al. (2016), Dynamic Geochemical Conditions Recorded by Lakebed Mudstones in Gale Crater, Mars, paper presented at 47th Lunar and Planetary Science Conference, LPI, Houston, TX, Abs. #1751.

Hurowitz, J. A., W. W. Fischer, N. J. Tosca, and R. E. Milliken (2010), Origin of acidic surface waters and the evolution of atmospheric chemistry on early Mars, *Nat Geosci*, *3*(5), 323-326, doi: 10.1038/ngeo831.

Jakosky, B. M. (1991), Mars Volatile Evolution - Evidence from Stable Isotopes, *Icarus*, *94*(1), 14-31, doi: 10.1016/0019-1035(91)90138-J.

Jambor, J. L., D. K. Nordstrom, and C. N. Alpers (2000), Metal-sulfate Salts from Sulfide Mineral Oxidation, *Reviews in Mineralogy and Geochemistry*, *40*(1), 303-350, doi: 10.2138/rmg.2000.40.6.

James, N. P., G. M. Narbonne, and A. G. Sherman (1998), Molar-tooth carbonates: Shallow subtidal facies of the mid- to late Proterozoic, *Journal of Sedimentary Research*, *68*(5), 716-722.

Jerolmack, D. J., and D. Mohrig (2007), Conditions for branching in depositional rivers, *Geology; Geology*, *35*(5), 463-466, doi: 10.1130/G23308a.1.

Jerolmack, D. J., D. Mohrig, M. T. Zuber, and S. Byrne (2004), A minimum time for the formation of Holden Northeast fan, Mars, *Geophys Res Lett*, *31*(21), doi: 10.1029/2004gl021326.

Johnsson, M. J., and A. Basu (1993), *Processes controlling the composition of clastic sediments*, Geological Society of America.

Kah, L. C., R. E. Kroynak, D. W. Ming, J. P. Grotzinger, J. Schieber, D. Sumner, and K. Edgett (2015), Diagenetic Crystal Growth in the Murray Formation, Gale Crater, Mars, paper presented at Geological Society of America Baltimore, MD, 267.

Kaufman, J., H. S. Cander, L. D. Daniels, and W. J. Meyers (1988), Calcite Cement Stratigraphy and Cementation History of the Burlington-Keokuk Formation (Mississippian), Illinois and Missouri, *Journal of Sedimentary Petrology*, *58*(2), 312-326.

Kirk, R. L., et al. (2008), Ultrahigh resolution topographic mapping of Mars with MRO HiRISE stereo images: Meter-scale slopes of candidate Phoenix landing sites, *J Geophys Res*, *113*, doi: 10.1029/2007je003000.

Kite, E. S., K. W. Lewis, M. P. Lamb, C. E. Newman, and M. I. Richardson (2013), Growth and form of the mound in Gale Crater, Mars: Slope wind enhanced erosion and transport, *Geology; Geology*, *41*(5), 543-546, doi: 10.1130/G33909.1.

Knipe, R. (1992), Faulting processes and fault seal, *Structural and tectonic modelling and its application to petroleum geology: Norwegian Petroleum Society Special Publication*, *1*, 325-342.

Knoll, A. H., and J. Grotzinger (2006), Water on Mars and the prospect of Martian life, *Elements*, *2*(3), 169-173, doi: 10.2113/gselements.2.3.169.

Komar, P. D. (2007), The Entrainment, Transport, and Sorting of Heavy Minerals by Waves and Currents, in *Heavy Minerals in Use*, edited by M. T. Mange and D. T. Wright, pp. 3-48, Elsevier, Italy.

Kroynak, R. E., L. C. Kah, J. P. Grotzinger, M. Fisk, D. Sumner, M. Nachon, N. Mangold, D. Blaney, W. Rapin, and R. Wiens (2015), Garden City: A complex vein system observed by the Curiosity rover at Pahrump Hills, Gale Crater, Mars, paper presented at Geological Society of America, Baltimore, MD, 217.

Kuhlmann, G., P. L. de Boer, R. B. Pedersen, and T. E. Wong (2004), Provenance of Pliocene sediments and paleoenvironmental changes in the southern North Sea region using Samarium–Neodymium (Sm/Nd) provenance ages and clay mineralogy, *Sedimentary Geology*, *171*(1-4), 205-226, doi: 10.1016/j.sedgeo.2004.05.016.

Lachenbruch, A. H. (1962), Mechanics of thermal contraction cracks and ice-wedge polygons in permafrost, *Geological Society of America Special Papers*, *70*, 1-66.

Lachenbruch, A. H. (1963), Contraction Theory of Ice-Wedge Polygons: A Qualitative Discussion, in *Permafrost International Conference*, edited, pp. 63-70, National Academy of Sciences, Lafayette, Indiana.

Langmuir, C. H., R. D. Vocke, G. N. Hanson, and S. R. Hart (1978), A General Mixing Equation with Applications to Icelandic Basalts, *Earth Planet Sc Lett*, *37*, 380-392.

Lanza, N. L., et al. (submitted), Oxidation of Manganese in an Ancient Aquifer, Kimberley Formation, Gale Crater, Mars, *Nature*.

Lasue, J., et al. (2016), Observation of > 5 wt % zinc at the Kimberley outcrop, Gale crater, Mars, *Journal of Geophysical Research: Planets*, *121*(3), 338-352, doi: 10.1002/2015je004946.

Léveillé, R. J., et al. (2014), Chemistry of fracture-filling raised ridges in Yellowknife Bay, Gale Crater: Window into past aqueous activity and habitability on Mars, *J Geophys Res-Planet*, *119*(11), 2398-2415, doi: 10.1002/2014je004620.

Long, J. C. S., et al. (1996), *Rock Fractures and Fluid Flow: Contemporary Understanding and Applications*, 551 pp., National Academy Press, Washington, D. C.

Longman, M. W. (1980), Carbonate Diagenetic Textures from Nearsurface Diagenetic Environments, *Aapg Bull*, *64*(4), 461-487.

Mackie, W. (1923), The Principles that Regulate the Distribution of Particles of Heavy Minerals in Sedimentary Rocks, as illustrated by the Sandstones of the North-East of Scotland, *Trans. Edinburgh Geol. Soc.*, *11*, 138-164.

Maki, J., D. Thiessen, A. Pourangi, P. Kobzeff, T. Litwin, L. Scherr, S. Elliott, A. Dingizian, and M. Maimone (2012), The Mars Science Laboratory Engineering Cameras, *Space Sci Rev*, *170*(1-4), 77-93, doi: 10.1007/s11214-012-9882-4.

Malin, M., M. Caplinger, K. Edgett, F. Ghaemi, M. Ravine, J. Schaffner, J. Baker, J. Bardis, D. DiBiase, and J. Maki (2010), The Mars Science Laboratory (MSL) mast-mounted cameras (Mastcams) flight instruments, paper presented at 41st Lunar and Planetary Science Conference, LPI, Houston, TX, Abs. #1123.

Malin, M. C., and K. S. Edgett (2000), Sedimentary rocks of early Mars, *Science*, *290*(5498), 1927-1937, doi: 10.1126/science.290.5498.1927.

Malin, M. C., and K. S. Edgett (2003), Evidence for persistent flow and aqueous sedimentation on early Mars, *Science*, *302*(5652), 1931-1934, doi: 10.1126/science.1090544.

Manda, A. K., and M. R. Gross (2006), Estimating aquifer-scale porosity and the REV for karst limestones using GIS-based spatial analysis, *Geol S Am S, 404*, 177-189, doi: 10.1130/2006.2404(15).

Mangold, N., D. Baratoux, O. Arnalds, J. M. Bardintzeff, B. Platevoet, M. Grégoire, and P. Pinet (2011), Segregation of olivine grains in volcanic sands in Iceland and implications for Mars, *Earth Planet Sc Lett*, *310*(3-4), 233-243, doi: 10.1016/j.epsl.2011.07.025.

Mangold, N., et al. (2016), Composition of conglomerates analyzed by the Curiosity rover: Implications for Gale Crater crust and sediment sources, *J Geophys Res-Planet*, *121*(3), 353-387, doi: 10.1002/2015je004977.

Marshall, D., and C. D. Anglin (2004), CO2-clathrate destabilization: a new model of formation for molar tooth structures, *Precambrian Res*, *129*(3-4), 325-341, doi: 10.1016/j.precamres.2003.10.007.

Mattson, S., R. Kirk, R. Heyd, A. McEwen, E. Eliason, T. Hare, R. Beyer, E. Howington-Kraus, C. H. Okubo, and K. Herkenhoff (2011), Release of HiRISE Digital Terrain Models to the Planetary Data System, paper presented at 42nd Lunar and Planetary Science Conference, LPI, Houston, TX, Abs. #1558.

McCauley, J. F. (1973), Mariner 9 evidence for wind erosion in the equatorial and mid-latitude regions of Mars, *J Geophys Res*, *78*(20), 4123-4137, doi: 10.1029/JB078i020p04123.

McCauley, J. F., M. H. Carr, J. A. Cutts, W. K. Hartmann, H. Masursky, D. J. Milton, R. P. Sharp, and D. E. Wilhelms (1972), Preliminary Mariner 9 report on the geology of Mars, *Icarus*, *17*(2), 289-327.

McEwen, A. S., et al. (2007a), Mars Reconnaissance Orbiter's High Resolution Imaging Science Experiment (HiRISE), *J Geophys Res*, *112*(E5), doi: 10.1029/2005je002605.

McEwen, A. S., et al. (2007b), A closer look at water-related geologic activity on Mars, *Science*, *317*(5845), 1706-1709, doi: 10.1126/science.1143987.

McLennan, S., and J. Grotzinger (2008a), The sedimentary rock cycle of Mars, *The Martian Surface-Composition, Mineralogy, and Physical Properties*, *1*, 541.

McLennan, S. M. (2001), Relationships between the trace element composition of sedimentary rocks and upper continental crust, *Geochemistry Geophysics Geosystems*, *2*.

McLennan, S. M. (2012), Geochemistry of Sedimentary Processes on Mars, in *Sedimentary Geology of Mars*, edited by J. Grotzinger and R. Milliken, p. 270, SEPM, Tulsa, Oklahoma.

McLennan, S. M., and J. Grotzinger (2008b), The Sedimentary Rock Cycle of Mars, in *The Martian Surface: Composition, Mineralogy, and Physical Properties*, edited by J. F. Bell, pp. 541-577, Cambridge University Press.

McLennan, S. M., S. R. Taylor, M. T. McCulloch, and J. B. Maynard (1990), Geochemical and Nd-Sr Isotopic Composition of Deep-Sea Turbidites - Crustal Evolution and Plate Tectonic Associations, *Geochim Cosmochim Ac*, *54*(7), 2015-2050, doi: 10.1016/0016-7037(90)90269-Q.

McLennan, S. M., S. Hemming, D. K. McDaniel, and G. N. Hansen (1993), Geochemical approaches to sedimentation, provenance, and tectonics, *Geological Society of America Special Papers*, *284*, 21-40, doi: 10.1130/SPE284-p21.

McLennan, S. M., B. Bock, S. R. Hemming, J. A. Hurowitz, S. M. Lev, and D. K. McDaniel (2003), The roles of provenance and sedimentary processes in the geochemistry of sedimentary rocks, in *Geochemistry of Sediments and Sedimentary Rocks: Evolutionary Considerations to Mineral Deposit-Forming Environments*, edited by D. R. Lentz, pp. 7-38, Geological Association of Canada: GeoText.

McLennan, S. M., E. Dehouck, J. P. Grotzinger, J. A. Hurowitz, N. Mangold, and K. Siebach (2015), Geochemical Record of Open-System Chemical Weathering at Gale Crater and Implications for Paleoclimates on Mars, paper presented at 46th Lunar and Planetary Science Conference, LPI, Houston, TX, Abs. #2533.

McLennan, S. M., et al. (2005), Provenance and diagenesis of the evaporite-bearing Burns formation, Meridiani Planum, Mars, *Earth Planet Sc Lett*, *240*(1), 95-121, doi: 10.1016/j.epsl.2005.09.041.

McLennan, S. M., et al. (2014), Elemental Geochemistry of Sedimentary Rocks at Yellowknife Bay, Gale Crater, Mars, *Science*, *343*(6169), doi: 10.1126/science.1244734.

Meyers, W. J. (1974), Carbonate cement stratigraphy of the Lake Valley Formation (Mississippian) Sacramento Mountains, New Mexico, *Journal of Sedimentary Research*, *44*(3), 837-861.

Meyers, W. J. (1991), Calcite cement stratigraphy: an overview. SEPM Short Course, 25, pp. 133-148.

Meyers, W. J., and K. C. Lohmann (1985), Isotope geochemistry of regionally extensive calcite cement zones and marine components in Mississippian limestones, New Mexico, in *Carbonate Cements*, edited by N. Schneidermann and P. M. Harris, pp. 223-239, Soc. Econ. Pal. Min. Sp. Pub. 36.

Milliken, R. E., J. P. Grotzinger, and B. J. Thomson (2010), Paleoclimate of Mars as captured by the stratigraphic record in Gale Crater, *Geophys Res Lett*, *37*(4), doi: 10.1029/2009gl041870.

Ming, D. W., et al. (2014), Volatile and Organic Compositions of Sedimentary Rocks in Yellowknife Bay, Gale Crater, Mars, *Science, 343*(6169), doi: 10.1126/science.1245267.

Mitchener, H., and H. Torfs (1996), Erosion of mud/sand mixtures, *Coastal Engineering*, *29*(1–2), 1-25, doi: 10.1016/S0378-3839(96)00002-6.

Moratto, Z., M. Broxton, R. Beyer, M. Lundy, and K. Husmann (2010), Ames Stereo Pipeline, NASA's open source automated stereogrammetry software, paper presented at 41st Lunar and Planetary Science Conference, LPI, Houston, TX, Abs. #2364.

Morris, R., et al. (2014), The Amorphous Component in Martian Basaltic Soil in Global Perspective from MSL and MER Missions, paper presented at 45th Lunar and Planetary Science Conference, LPI, Houston, TX, Abs. #1319.

Morris, R. V., et al. (submitted), Silicic volcanism on Mars evidenced by tridymite in high-SiO2 sedimentary rock at Gale crater, *PNAS*.

Morrison, S. M., et al. (2015), Crystal-Chemical Analysis of Martian Minerals in Gale Crater, paper presented at 46th Lunar and Planetary Science Conference, LPI, Houston, Abs. #2506.

Murchie, S. L., et al. (2009), A synthesis of Martian aqueous mineralogy after 1 Mars year of observations from the Mars Reconnaissance Orbiter, *J Geophys Res*, *114,* doi: 10.1029/2009je003342.

Murray, B. C., L. A. Soderblom, J. A. Cutts, R. P. Sharp, D. J. Milton, and R. B. Leighton (1972), Geological Framework of the South Polar Region of Mars, *Icarus*, *17*(2), 328-345.

Mustard, J. F., F. Poulet, B. L. Ehlmann, R. Milliken, and A. Fraeman (2012), Sequestration of Volatiles in the Martian Crust through Hydrated Minerals: A Significant Planetary Reservoir of Water, paper presented at 43rd Lunar and Planetary Science Conference, LPI, Houston, TX, Abs. #1539.

Mustard, J. F., et al. (2008), Hydrated silicate minerals on Mars observed by the Mars Reconnaissance Orbiter CRISM instrument, *Nature*, *454*(7202), 305-309, doi: 10.1038/nature07097.

Nachon, M., et al. (2014), Calcium sulfate veins characterized by ChemCam/Curiosity at Gale crater, Mars, *J Geophys Res-Planet*, *119*(9), 1991-2016, doi: 10.1002/2013je004588.

NASA-JPL (2013), Mars Science Laboratory Project Software Interface Specification (SIS), Mast Camera (Mastcam), Mars Hand Lens Imager (MAHLI), and Mars Descent

Imager (MARDI) Experiment Data Record (EDR) and Reduced Data Record (RDR) PDS Data Products, edited.

Nelson, E. P., A. J. Kullman, M. H. Gardner, and M. Batzle (1999), Fault-Fracture Networks and Related Fluid Flow and Sealing, Brushy Canyon Formation, West Texas, in *Faults and Subsurface Fluid Flow in the Shallow Crust*, edited by W. C. Haneburg, P. S. Mozley, J. C. Moore and L. B. Goodwin, pp. 69-81, American Geophysical Union.

Nesbitt, H. W. (2003), Petrogenesis of siliciclastic sediments and sedimentary rocks, in *Geochemistry of Sediments and Sedimentary Rocks: Evolutionary Considerations to Mineral Deposit-Forming Environments*, edited by D. R. Lentz, pp. 39-51, Geological Association of Canada.

Nesbitt, H. W., and G. M. Young (1982), Early Proterozoic Climates and Plate Motions Inferred from Major Element Chemistry of Lutites, *Nature*, *299*(5885), 715-717, doi: 10.1038/299715a0.

Nesbitt, H. W., and G. M. Young (1984), Prediction of Some Weathering Trends of Plutonic and Volcanic-Rocks Based on Thermodynamic and Kinetic Considerations, *Geochim Cosmochim Ac*, *48*(7), 1523-1534, doi: 10.1016/0016-7037(84)90408-3.

Nesbitt, H. W., and R. E. Wilson (1992), Recent Chemical Weathering of Basalts, *American Journal of Science*, *292*(10), 740-777.

Nesbitt, H. W., and G. M. Young (1996), Petrogenesis of sediments in the absence of chemical weathering: Effects of abrasion and sorting on bulk composition and mineralogy, *Sedimentology*, *43*(2), 341-358, doi: 10.1046/j.1365-3091.1996.d01-12.x.

Nesbitt, H. W., G. M. Young, S. M. McLennan, and R. R. Keays (1996), Effects of Chemical Weathering and Sorting on the Petrogenesis of Siliciclastic Sediments, with Implications for Provenance Studies, *The Journal of Geology*, *104*(5), 525-542, doi: 10.1086/629850.

Newsom, H. E., et al. (2016), The Materials at an Unconformity between the Murray and Stimson Formations at Marias Pass, Gale Crater, Mars, paper presented at 47th Lunar and Planetary Science Conference LPI, Houston, TX, Abs. #2397.

O'Brien, N. R. (1996), Shale lamination and sedimentary processes, *Geological Society, London, Special Publications*, *116*(1), 23-26, doi: 10.1144/GSL.SP.1996.116.01.04.

O'Connor, M. P. (1972), Classification and Environmental Interpretation of the Cryptalgal Organosedimentary "MolarTooth" Structure from the Late Precambrian Belt-Purcell Supergroup, *The Journal of Geology*, *80*(5), 592-610.

Ohta, T. (2004), Geochemistry of Jurassic to earliest Cretaceous deposits in the Nagato Basin, SW Japan: implication of factor analysis to sorting effects and provenance signatures, *Sedimentary Geology*, *171*(1-4), 159-180, doi: 10.1016/j.sedgeo.2004.05.014.

Okubo, C. H., and A. S. McEwen (2007), Fracture-controlled paleo-fluid flow in Candor Chasma, Mars, *Science*, *315*(5814), 983-985, doi: 10.1126/science.1136855.

Olson, J. E., S. E. Laubach, and R. H. Lander (2009), Natural fracture characterization in tight gas sandstones: Integrating mechanics and diagenesis, *AAPG Bulletin*, *93*(11), 1535-1549, doi: 10.1306/08110909100.

Palmer, M. R., and J. M. Edmond (1989), The strontium isotope budget of the modern ocean, *Earth Planet Sc Lett*, *92*(1), 11-26, doi: 10.1016/0012-821x(89)90017-4.

Palucis, M. C., W. E. Dietrich, A. G. Hayes, R. M. E. Williams, S. Gupta, N. Mangold, H. Newsom, C. Hardgrove, F. Calef, and D. Y. Sumner (2014), The origin and evolution of the Peace Vallis fan system that drains to the Curiosity landing area, Gale Crater, Mars, *J Geophys Res-Planet*, *119*(4), 705-728, doi: 10.1002/2013je004583.

Papike, J. J., J. M. Karner, C. K. Shearer, and P. V. Burger (2009), Silicate mineralogy of martian meteorites, *Geochim Cosmochim Ac*, *73*(24), 7443-7485, doi: 10.1016/j.gca.2009.09.008.

Parker, T. J., M. C. Malin, F. J. Calef, R. G. Deen, H. E. Gengl, M. P. Golombek, J. R. Hall, O. Pariser, M. Powell, and R. S. Sletten (2013), Localization and 'Contextualization' of Curiosity in Gale Crater, and Other Landed Mars Missions, paper presented at 44th Lunar and Planetary Science Conference, LPI, Houston, TX, Abs. #2534.

Peck, D. L., and T. Minakami (1968), The formation of columnar joints in the upper part of Kilauean lava lakes, Hawaii, *GSA Bulletin*, *79*(9), 1151-1166.

Pettijohn, F. J., and P. E. Potter (1964), *Atlas and glossary of primary sedimentary structures*, 370 pp., Springer-Verlag New York, Germany.

Plaut, J. J., et al. (2007), Subsurface radar sounding of the south polar layered deposits of Mars, *Science*, *316*(5821), 92-95, doi: 10.1126/science.1139672.

Plummer, P. S., and V. A. Gostin (1981), Shrinkage Cracks - Desiccation or Synaeresis, *Journal of Sedimentary Petrology, 51*(4), 1147-1156.

Pollock, M. D., L. C. Kah, and J. K. Bartley (2006), Morphology of Molar-Tooth Structures in Precambrian Carbonates: Influence of Substrate Rheology and Implications for Genesis, *Journal of Sedimentary Research*, *76*(2), 310-323, doi: 10.2110/jsr.2006.021.

Poulet, F., et al. (2005), Phyllosilicates on Mars and implications for early martian climate, *Nature*, *438*(7068), 623-627, doi: 10.1038/nature04274.

Pratt, B. R. (1998a), Molar-tooth structure in Proterozoic carbonate rocks: Origin from synsedimentary earthquakes, and implications for the nature and evolution of basins and marine sediment, *Geological Society of America Bulletin*, *110*(8), 1028-1045, doi: 10.1130/0016-7606(1998)110<1028:Mtsipc>2.3.Co;2.

Pratt, B. R. (1998b), Syneresis cracks: subaqueous shrinkage in argillaceous sediments caused by earthquake-induced dewatering, *Sedimentary Geology*, *117*(1-2), 1-10, doi: 10.1016/S0037-0738(98)00023-2.

Press, W. H., S. A. Teukolsky, W. T. Vetterling, and B. P. Flannery (1992), *Numerical Recipes in FORTRAN: The Art of Scientific Computing*, 2nd ed., 963 pp., Cambridge University Press, Cambridge.

Rampe, E., et al. (2016), Diagenesis in the Murray Formation, Gale Crater, Mars, paper presented at 47th Lunar and Planetary Science Conference, LPI, Houston, TX, Abs. #2543.

Rampe, E. B., et al. (in prep.), Mineralogical trends in mudstones from the Murray formation, Gale crater, Mars.

Ramseyer, K., J. E. Amthor, A. Matter, T. Pettke, M. Wille, and A. E. Fallick (2013), Primary silica precipitate at the Precambrian/Cambrian boundary in the South Oman Salt Basin, Sultanate of Oman, *Marine and Petroleum Geology*, *39*(1), 187-197, doi: 10.1016/j.marpetgeo.2012.08.006.

Reid, M. J., A. J. Gancarz, and A. L. Albee (1973), Constrained Least-Squares Analysis of Petrologic Problems with an Application to Lunar Sample 12040, *Earth Planet Sc Lett*, *17*(2), 433-445, doi: 10.1016/0012-821x(73)90212-4.

Rieder, R., T. Economou, H. Wanke, A. Turkevich, J. Crisp, J. Bruckner, G. Dreibus, and H. Y. McSween (1997), The Chemical Composition of Martian Soil and Rocks Returned by the Mobile Alpha Particle X-ray Spectrometer: Preliminary Results from the X-ray Mode, *Science*, *278*, 1771.

Rodriguez-Navarro, C. (1998), Evidence of honeycomb weathering on Mars, *Geophys Res Lett*, *25*(17), 3249-3252, doi: 10.1029/98gl02569.

Rubey, W. W. (1933), The size-distribution of heavy minerals within a water-laid sandstone, *Journal of Sedimentary Petrology*, *3*(1), 3-29.

Russell, R. D. (1937), Mineral composition of Mississippi River sands, *Bulletin of the Geological Society of America*, *48*(9/12), 1307-1348.

Santos, A. R., C. B. Agee, F. M. McCubbin, C. K. Shearer, P. V. Burger, R. Tartèse, and M. Anand (2015), Petrology of igneous clasts in Northwest Africa 7034: Implications for the petrologic diversity of the martian crust, *Geochim Cosmochim Ac, 157*, 56-85, doi: 10.1016/j.gca.2015.02.023.

Sarbas, B., and U. Nohl (2008), The GEOROC database as part of a growing geoinformatics network, in *Geoinformatics 2008-Data to Knowledge, Proceedings: U.S. Geological Survey Scientific Investigations Report 2008*, edited by S. R. Brady, A. K. Sinha and L. C. Gundersen, pp. 42-43.

Sautter, V., et al. (2016), Magmatic complexity on early Mars as seen through a combination of orbital, in-situ and meteorite data, *Lithos*, *254-255*, 36-52, doi: 10.1016/j.lithos.2016.02.023.

Sautter, V., et al. (2015), In situ evidence for continental crust on early Mars, *Nat Geosci*, *8*(8), 605-609, doi: 10.1038/ngeo2474.

Schieber, J., S. Gupta, J. Grotzinger, and R. Suarez-Rivera (2013), Hydraulic Fracturing of Martian Mudstones, paper presented at Geological Society of America, Denver, CO, 39.

Schmidt, M. E., et al. (2014), Geochemical diversity in first rocks examined by the Curiosity Rover in Gale Crater: Evidence for and significance of an alkali and volatile-rich igneous source, *Journal of Geophysical Research: Planets*, *119*(1), 64-81, doi: 10.1002/2013je004481.

Schnurrenberger, D., J. Russell, and K. Kelts (2003), Classification of lacustrine sediments based on sedimentary components, *Journal of Paleolimnology*, *29*(2), 141-154, doi: 10.1023/A:1023270324800.

Sharp, R. P., and M. C. Malin (1975), Channels on Mars, *Geological Society of America Bulletin*, *86*(5), 593-609, doi: 10.1130/0016-7606(1975)86<593:Com>2.0.Co;2.

Sheldon, N. D. (2003), Pedogenesis and geochemical alteration of the Picture Gorge subgroup, Columbia River Basalt, Oregon, *Geological Society of America Bulletin*, *115*(11), 1377-1387, doi: 10.1130/B25223.1.

Shorlin, K. A., J. R. de Bruyn, M. Graham, and S. W. Morris (2000), Development and geometry of isotropic and directional shrinkage-crack patterns, *Physical Review E, 61*(6), 6950-6957.

Siebach, K. L., and J. P. Grotzinger (2014a), Volumetric estimates of ancient water on Mount Sharp based on boxwork deposits, Gale Crater, Mars, *Journal of Geophysical Research: Planets, 119*(1), 189-198, doi: 10.1002/2013je004508.

Siebach, K. L., and J. P. Grotzinger (2014b), Characterizing Sandstone Porosity along Curiosity's Traverse using MAHLI Imagery, paper presented at Eighth International Conference on Mars, Pasadena, CA, 1466.

Siebach, K. L., M. B. Baker, J. P. Grotzinger, S. M. McLennan, R. Gellert, and J. A. Hurowitz (in prep.), Sorting out Compositional Trends in Sedimentary Rocks of the Bradbury Group (Aeolus Palus), Gale Crater, Mars, *J Geophys Res*.

Siebach, K. L., J. P. Grotzinger, L. C. Kah, K. M. Stack, M. Malin, R. Leveille, and D. Y. Sumner (2014), Subaqueous shrinkage cracks in the Sheepbed mudstone: Implications for early fluid diagenesis, Gale crater, Mars, *J Geophys Res-Planet*, *119*(7), 1597-1613, doi: 10.1002/2014je004623.

Slatt, R. M., and N. Eyles (1981), Petrology of Glacial Sand - Implications for the Origin and Mechanical Durability of Lithic Fragments, *Sedimentology*, *28*(2), 171-183, doi: 10.1111/j.1365-3091.1981.tb01675.x.

Sletten, R. S., B. Hallet, and R. C. Fletcher (2003), Resurfacing time of terrestrial surfaces by the formation and maturation of polygonal patterned ground, *J Geophys Res*, *108*(E4), doi: 10.1029/2002je001914.

Slingerland, R. L. (1977), The Effects of Entrainment on the Hydraulic Equivalence Relationships of Light and Heavy Minerals, *Journal of Sedimentary Petrology*, *47*, 753-770.

Smith, A. G. (1968), The Origin and Deformation of Some "Molar-Tooth" Structures in the Precambrian BeltPurcell Supergroup, *The Journal of Geology*, *76*(4), 426-443.

Smith, D. E., G. A. Neumann, R. E. Arvidson, E. Guinness, and S. Slavney (2003), Mars Global Surveyor laser altimeter initial experiment gridded data record (MGS-M-MOLA), 5-MEGDR-L3-V1.0, edited, NASA Planetary Data System (PDS), Greenbelt, MD.

Soderblom, L. A., M. C. Malin, J. A. Cutts, and B. C. Murray (1973), Mariner 9 observations of the surface of Mars in the north polar region, *J Geophys Res*, *78*(20), 4197-4210, doi: 10.1029/JB078i020p04197.

Squyres, S. W., et al. (2004), In situ evidence for an ancient aqueous environment at Meridiani Planum, Mars, *Science*, *306*(5702), 1709-1714, doi: 10.1126/science.1104559.

Stack, K. M., et al. (2014), Diagenetic origin of nodules in the Sheepbed member, Yellowknife Bay formation, Gale crater, Mars, *J Geophys Res-Planet*, *119*(7), 1637-1664, doi: 10.1002/2014je004617.

Stolper, E. M., et al. (2013), The petrochemistry of Jake_M: a martian mugearite, *Science*, *341*(6153), 1239463, doi: 10.1126/science.1239463.

Stumm, W., and J. J. Morgan (2012), *Aquatic chemistry: chemical equilibria and rates in natural waters*, John Wiley & Sons.

Szabo, T., G. Domokos, J. P. Grotzinger, and D. J. Jerolmack (2015), Reconstructing the transport history of pebbles on Mars, *Nature communications*, *6*, 8366, doi: 10.1038/ncomms9366.

Tanaka, K. L., J. A. Skinner, J. M. Dohm, R. P. Irwin, E. J. Kolb, C. M. Fortezzo, T. Platz, G. G. Michael, and T. M. Hare (2014), Geologic map of Mars, doi: 10.3133/sim3292.

Taylor, S. M., and S. M. McLennan (2009), *Planetary Crusts: Their Composition, Origin, and Evolution*, Cambridge University Press.

Taylor, S. R., and S. M. McLennan (1995), The Geochemical Evolution of the Continental-Crust, *Rev Geophys*, *33*(2), 241-265, doi: 10.1029/95rg00262.

Team, R. (1997), Characterization of the Martian Surface Deposits by the Mars Pathfinder Rover, Sojourner, *Science*, *278*(5344), 1765-1768, doi: 10.1126/science.278.5344.1765.

Terzaghi, K. (1944), *Theoretical Soil Mechanics*, 510 pp., London.

Therriault, A. M., A. D. Fowler, and R. A. F. Grieve (2002), The Sudbury Igneous Complex: A Differentiated Impact Melt Sheet, *Economic Geology*, *97*(7), 1521-1540, doi: 10.2113/gsecongeo.97.7.1521.

Thomson, B. J., and N. Bridges (2008), Gale Crater: Context and layer diversity from HiRISE Images, paper presented at Third Mars Science Laboratory Landing Site Workshop, Monrovia, CA.

Thomson, B. J., N. T. Bridges, R. Milliken, A. Baldridge, S. J. Hook, J. K. Crowley, G. M. Marion, C. R. de Souza, A. J. Brown, and C. M. Weitz (2011), Constraints on the origin and evolution of the layered mound in Gale Crater, Mars using Mars Reconnaissance Orbiter data, *Icarus*, *214*(2), 413-432, doi: 10.1016/j.icarus.2011.05.002.

Tosca, N. J. (2004), Acid-sulfate weathering of synthetic Martian basalt: The acid fog model revisited, *J Geophys Res*, *109*(E5), doi: 10.1029/2003je002218.

Tosca, N. J., A. H. Knoll, and S. M. McLennan (2008), Water activity and the challenge for life on early Mars, *Science*, *320*(5880), 1204-1207, doi: 10.1126/science.1155432.

Tosca, N. J., F. A. Macdonald, J. V. Strauss, D. T. Johnston, and A. H. Knoll (2011), Sedimentary talc in Neoproterozoic carbonate successions, *Earth Planet Sc Lett*, *306*(1-2), 11-22, doi: 10.1016/j.epsl.2011.03.041.

Treiman, A. H., et al. (2015), Mineralogy, Provenance, and Diagenesis of a Potassic Basaltic Sandstone on Mars: CheMin X-ray Diffraction of the Windjana Sample (Kimberley Area, Gale Crater), *Journal of Geophysical Research: Planets*, doi: 10.1002/2015je004932.

Tucker, E. (2009), *Sedimentary Petrology: An Introduction to the Origin of Sedimentary Rocks*, Wiley.

VanBommel, S. J., R. Gellert, J. A. Berger, J. L. Campbell, L. M. Thompson, K. S. Edgett, M. J. McBride, M. E. Minitti, I. Pradler, and N. I. Boyd (2016), Deconvolution of distinct lithology chemistry through oversampling with the Mars Science Laboratory Alpha Particle X-Ray Spectrometer, *X-Ray Spectrometry*, *45*(3), 155-161, doi: 10.1002/xrs.2681.

Vaniman, D., et al. (2014), Mineralogy of a Mudstone at Yellowknife Bay, Gale Crater, Mars, *Science*, *343*(6169), doi: 10.1126/science.1243480.

Vaniman, D. T., D. L. Bish, S. J. Chipera, C. I. Fialips, J. W. Carey, and W. C. Feldman (2004), Magnesium sulphate salts and the history of water on Mars, *Nature*, *431*(7009), 663-665, doi: 10.1038/nature02973.

Vervott, J. D., P. J. Patchett, J. Blichert-Toft, and F. Albarede (1999), Relationships between Lu-Hf and Sm-Nd isotopic systems in the global sedimentary system, *Earth Planet Sc Lett*, *168*, 79-99.

Vezzoli, G., E. Garzanti, and S. Monguzzi (2004), Erosion in the Western Alps (Dora Baltea basin) 1. Quantifying Sediment Provenance, *Sedimentary Geology*, *171*(1-4), 227-246, doi: 10.1016/j.sedgeo.2004.05.017.

von Eynatten, H. (2004), Statistical modelling of compositional trends in sediments, *Sedimentary Geology*, *171*(1-4), 79-89, doi: 10.1016/j.sedgeo.2004.05.011.

von Eynatten, H., R. Tolosana-Delgado, and V. Karius (2012), Sediment generation in modern glacial settings: Grain-size and source-rock control on sediment composition, *Sedimentary Geology*, *280*, 80-92, doi: 10.1016/j.sedgeo.2012.03.008.

Walter, M. J., T. W. Sisson, and D. C. Presnall (1995), A Mass Proportion Method for Calculating Melting Reactions and Application to Melting of Model Upper-Mantle Lherzolite, *Earth Planet Sc Lett*, *135*(1-4), 77-90, doi: 10.1016/0012-821x(95)00148-6.

Watkins, J., J. Grotzinger, N. Stein, S. Banham, S. Gupta, D. Rubin, K. Stack, and K. Edgett (2016), Paleotopography of Erosional Unconformity, Base of Stimson Formation, Gale Crater, Mars, paper presented at 47th Lunar and Planetary Science Conference, LPI, Houston, TX, Abs. #2939.

Weinberger, R. (1999), Initiation and growth of cracks during desiccation of stratified muddy sediments, *Journal of Structural Geology*, *21*(4), 379-386, doi: 10.1016/S0191-8141(99)00029-2.

Weltje, G. J. (2004), A quantitative approach to capturing the compositional variability of modern sands, *Sedimentary Geology*, *171*(1-4), 59-77, doi: 10.1016/j.sedgeo.2004.05.010.

Weltje, G. J., and H. von Eynatten (2004), Quantitative provenance analysis of sediments: review and outlook, *Sedimentary Geology*, *171*(1-4), 1-11, doi: 10.1016/j.sedgeo.2004.05.007.

White, W. A. (1961), Colloid Phenomena in Sedimentation of Argillaceous Rocks, *Journal of Sedimentary Petrology*, *31*(4), 560-570.

Whitmore, G. P., K. A. W. Crook, and D. P. Johnson (2004), Grain size control of mineralogy and geochemistry in modern river sediment, New Guinea collision, Papua New Guinea, *Sedimentary Geology*, *171*(1-4), 129-157, doi: 10.1016/j.sedgeo.2004.03.011.

Williams, R. M., et al. (2013), Martian fluvial conglomerates at Gale crater, *Science, 340*(6136), 1068-1072, doi: 10.1126/science.1237317.

Wittmann, A., R. L. Korotev, B. L. Jolliff, A. J. Irving, D. E. Moser, I. Barker, and D. Rumble (2015), Petrography and composition of Martian regolith breccia meteorite Northwest Africa 7475, *Meteoritics & Planetary Science*, *50*(2), 326-352, doi: 10.1111/maps.12425.

Worden, R., and S. Burley (2003), Sandstone diagenesis: the evolution of sand to stone, *Sandstone Diagenesis: Recent and Ancient*, 1-44.

Wray, J. J., S. T. Hansen, J. Dufek, G. A. Swayze, S. L. Murchie, F. P. Seelos, J. R. Skok, R. P. Irwin, and M. S. Ghiorso (2013), Prolonged magmatic activity on Mars inferred from the detection of felsic rocks, *Nat Geosci*, *6*(12), 1013-1017, doi: 10.1038/ngeo1994.

Yen, A. S., et al. (2005), An integrated view of the chemistry and mineralogy of martian soils, *Nature*, *436*(7047), 49-54, doi: 10.1038/nature03637.

Young, G. M., and H. W. Nesbitt (1999), Paleoclimatology and provenance of the glaciogenic Gowganda Formation (Paleoproterozoic), Ontario, Canada: A chemostratigraphic approach, *Geological Society of America Bulletin*, *111*(2), 264-274, doi: 10.1130/0016-7606(1999)111<0264:Papotg>2.3.Co;2.